OBSERVATIONS OF THE SPACE-TIME STRUCTURE OF FLOW, VORTICITY AND STRESS OVER ORBITAL-SCALE RIPPLES

by

Jenna Hare

Submitted in partial fulfillment of the requirements
for the degree of Master of Science

at

Dalhousie University
Halifax, Nova Scotia
May 2013

DALHOUSIE UNIVERSITY

DEPARTMENT OF OCEANOGRAPHY

The undersigned hereby certify that they have read and recommend to the Faculty of Graduate Studies for acceptance a thesis entitled “OBSERVATIONS OF THE SPACE-TIME STRUCTURE OF FLOW, VORTICITY AND STRESS OVER ORBITAL-SCALE RIPPLES” by Jenna Hare in partial fulfillment of the requirements for the degree of Master of Science.

Dated: May 28, 2013

Supervisor: ______________________________

Readers: ______________________________

____

____

____

____

DALHOUSIE UNIVERSITY

DATE: May 28, 2013

AUTHOR: Jenna Hare

TITLE: OBSERVATIONS OF THE SPACE-TIME STRUCTURE OF FLOW, VORTICITY AND STRESS OVER ORBITAL-SCALE RIPPLES

DEPARTMENT OR SCHOOL: Department of Oceanography

DEGREE: M.Sc. CONVOCATION: October YEAR: 2013

Signature of Author

TABLE OF CONTENTS

LIST OF TABLES

LIST OF FIGURES

ABSTRACT

The spatial and temporal structure of the flow, vorticity and stress over equilibrium orbital-scale sand ripples are investigated at turbulence-resolving scales with a wide-band coherent Doppler profiler (MFDop) in an oscillating tray apparatus. The oscillation period and horizontal excursion were 10 s and 0.5 m. Velocity profiles were acquired with 3 mm vertical resolution and at a 42 Hz sampling rate. Ripple wavelength and amplitude were 25 cm and 2.2 cm. The MFDop measurements are used to investigate the development of the lee vortex as a function of phase, and the co-evolution of turbulent kinetic energy, Reynolds stress and turbulence production. Shear stress is determined from the vertically-integrated vorticity equation and using the double-averaging approach. Friction factors obtained from the two methods are comparable and range from 0.1 to 0.2.

The spatial distribution of flow, Reynolds stress and turbulence as a function of oscillation phase were determined by combining the phase-averaged velocity measurements from trials with the MFDop at different positions relative to a particular ripple crest. Estimates of bottom shear stress were determined using different methods. It was found that the acceleration defect integral cannot be implemented since the boundary layer approximation does not hold over orbital-scale ripples. The law-of-the-wall yields friction factor values of about 2.5 and hydraulic roughness values of the order of 100 cm, which are physically unrealistic. The vorticity method assumes that the horizontal length scales are much greater than the vertical length scales, but provides bed shear stress estimates at all points along the ripple profile. Double-averaging necessarily produces only the net shear stress, but yields the relative contributions from the Reynolds stress and bedform-induced stress. For these two spatially-averaged methods, the hydraulic roughness to ripple height ratio lies between 1 and 3, which is much more sensible than the values of 14 to 40 obtained via the law-of-the-wall.

LIST OF ABBREVIATIONS AND SYMBOLS USED

Roman symbol	Description	Units
A	semi-excursion	m
a	ripple amplitude	m
d_0	orbital excursion	m
D_{50}	median grain diameter	m
$f_{2.5}$	grain roughness friction factor	
f_w	wave friction factor	
g	gravitational acceleration	m/s^2
k	ripple wave number	m^{-1}
p	fluid pressure	kg m^{-1} s^{-2}
p'	dynamic pressure at the bed	kg m^{-1} s^{-2}
prod	turbulence production	m^2/s^3
$\bar{R}$	ensemble-averaged complex correlation between consecutive pulses	
r_b	range within the bed	m
R_B	range to the sediment-water interface	m
Re	Reynolds stress	m^2/s^2
r_h	hydraulic roughness	m
s	sediment specific gravity	
t	time	s
T_K	RippleKart period	s
TKE	turbulent kinetic energy	m^2/s^2
u	horizontal velocity	m/s

Roman symbol	Description	Units
U_0	amplitude of free-stream velocity	m/s
U_∞	free-stream velocity	m/s
u_*	friction velocity	m/s
u_{*m}	maximum friction velocity	m/s
u_d	defect velocity	m/s
u_K	RippleKart velocity	m/s
u_{K0}	RippleKart velocity amplitude	m/s
u_{KF}	horizontal velocity in the frame of reference moving with the Kart	m/s
u_{LF}	horizontal velocity in the laboratory frame of reference	m/s
u_R	relative flow	m/s
u_{R0}	relative flow amplitude	m/s
u_V	reaction flow	m/s
u_{V0}	reaction flow amplitude	m/s
v	cross-tank velocity	m/s
V_{xx}	projections of the flow along the bisectors between two transducers	m/s
V_a	ambiguity velocity	m/s
w	vertical velocity	m/s
x	horizontal coordinate	m
z	vertical coordinate	m
z_0	roughness height	m
Δz	displacement height	m

Greek symbol	Description	Units
δ	boundary layer thickness, section 2.1	m
δ	time delay, section 3.3.1	s
ζ	horizontal component of vorticity	s^{-1}
ζ	bed profile used in the potential flow solution given by *Davies* (1983), section 2.2.1	m
ζ	complex plane used in the potential flow solution given by *Longuet-Higgins* (1981), section 2.2.2	
η_0	ripple height	m
θ	bisector angle	$^\circ$
$\theta_{2.5}$	grain roughness Shields parameter	
κ	von Karman's constant	
λ	ripple wavelength	m
ν	kinematic viscosity	m^2/s
ρ	water density	kg/m^3
τ	pulse repetition interval	s
τ^x	shear stress in the x-direction	kg m^{-1} s^{-2}
τ^z	shear stress in the z-direction	kg m^{-1} s^{-2}
τ_0	bed shear stress	kg m^{-1} s^{-2}
φ_j	phase of the jth pulse	
$\Phi(x, z, t)$	velocity potential	m^2/s
$\phi(x, z)$	velocity potential	m^2/s
ϕ_R	relative flow phase	$^\circ$
ϕ_V	reaction flow phase	$^\circ$
Ψ	roughness geometry function	
ψ	stream function	m^2/s
ω	angular frequency	s^{-1}

Greek symbol	Description	Units
ω_K	RippleKart oscillation frequency	s^{-1}

ACKNOWLEDGEMENTS

It is with immense gratitude that I acknowledge the tremendous support and help of my supervisor, Dr Alex E Hay. He has inspired me to bring his dedication to excellence to my own work, and without his guidance this research would not have been possible. I am likewise indebted to my committee members (Dr Anthony Bowen, Dr Stephanie Kienast and Dr Barry Ruddick) for their support and the insightful comments that have strengthened and bettered this thesis. In addition, I would like to thank Richard Cheel, whose assistance during the experiments as well as help outside the laboratory was greatly appreciated. I also wish to thank my friends and family for their comfort and loving support generously given whenever needed. Last but not least, I cannot find words to fully express my gratitude towards my father who has provided unwavering support and encouragement throughout this entire journey. I thank him for instilling in me at a young age the curiosity to explore this beautiful world and attempt to unravel its many mysteries.

CHAPTER 1

INTRODUCTION

1.1 Wave-generated ripples in sandy sediments

A variety of sedimentary structures ranging from small-scale O(10 cm) wavelength ripples to large-scale O(10 m) to O(100 m) dunes are usually present on the sea bed in sandy coastal and continental shelf environments, and also in the deep ocean. Small-scale structures such as ripples have an influence on the bottom boundary layer vertical structure, sediment transport rates as well as turbulence near the bed. My research will focus on ripples, more specifically orbital-scale vortex ripples. These ripples are usually formed under purely oscillatory flows. *Bagnold* (1946) first studied in detail the formation and physical properties such as the amplitude and wavelength of vortex ripples. Since then, a great many studies have focused on laboratory experiments involving ripples, *van der Werf et al.* (2007) being a recent example. In addition, numerical models, both Reynolds-averaged and turbulence-resolving, are currently being used to simulate ripple formation and evolution under oscillatory flow (*Marieu et al.*, 2008; *Chou and Fringer*, 2010).

Allen (1979) assembled data from various sources to create the existence field for wave-formed ripples, reproduced in Figure 1.1. *Allen* (1979) concluded that the occurrence of these ripples is a function of near-bed orbital velocity and sediment grain size. In Figure 1.1, the existence field of wave ripples is bounded below by the field of no bed-material movement on a plane bed, and above by that for intense sediment transport over a stable plane bed. Contours of limiting values of ripple steepness (ripple height η_0 to ripple wavelength λ ratio) are indicated. Flatter ripples occur at velocities near the field boundaries, whereas steeper ripples occur in medium-grained sand at velocities between

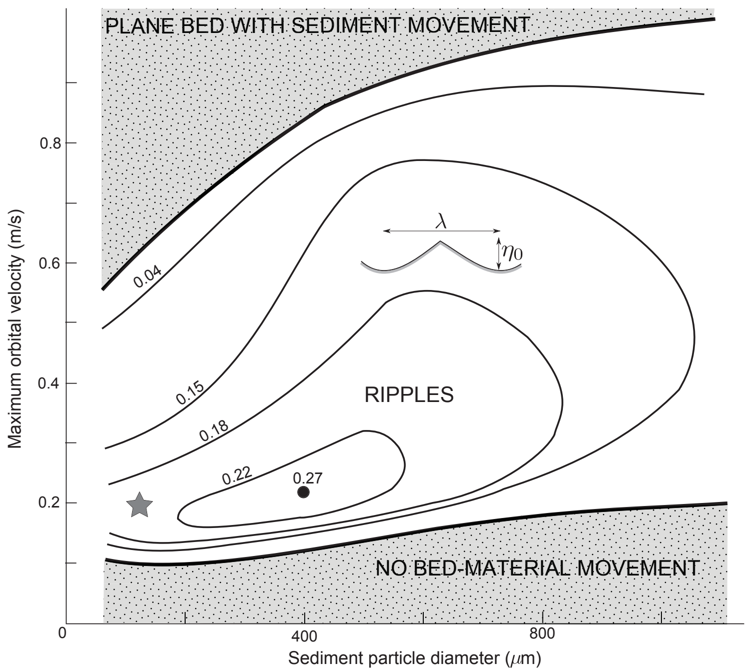

Figure 1.1: Existence field for wave-formed ripples: ripple steepness (η_0/λ) as a function of maximum near-bed orbital velocity and sediment particle diameter. The curves are limiting values of ripple steepness (modified from *Allen* (1979)). The star indicates the location of the ripples that were created experimentally in the present work.

0.16 m/s and 0.32 m/s (*Allen*, 1979).

Under the action of surface gravity waves, rolling-grain ripples with low steepness will be first to appear on an initially smooth bed. Sediment in motion near the bed is then carried away from the troughs towards the crests. As time increases, the ripples grow and tend to organize themselves in parallel transverse zones. When ripple steepness exceeds 0.1 (*Sleath*, 1984), vortex formation starts to occur in the lee of each ripple crest. The vortex scoops up grains of sediment from the troughs and places them on the ripple crests. In the case of finer sediment, a proportion of grains will overshoot the crest and be carried in a suspended sand cloud (*Bagnold*, 1946). As a result, near-bed sediment transport is greatly influenced by these vortices. In fact, *van der Werf et al.* (2007) conclude that the concentration field of suspended sediment above ripples is dominated by the formation and diffusion of these vortices.

Clifton and Dingler (1984), re-examined later by *Wiberg and Harris* (1994), classify equilibrium ripples into three categories based on wavelength λ and near-bed wave orbital diameter d_0. In order of increasing d_0, three categories of 2-dimensional ripples are observed: orbital, suborbital and anorbital-scale ripples. Orbital-scale ripples, as defined by *Wiberg and Harris* (1994), have wavelengths proportional to the near-bed wave orbital diameter d_0.

$$\lambda = 0.62 d_0 \tag{1.1}$$

It should be noted that orbital-scale ripples and vortex ripples are often considered to be equivalent. *Wiberg and Harris* (1994) also find an average steepness for orbital-scale ripples of

$$\frac{\eta_0}{\lambda} = 0.17 \tag{1.2}$$

1.2 Importance and timeliness

Before we can begin to understand the complexities of the physical processes occurring in the nearshore region, we must first have a better understanding of the fundamental processes involved under idealised conditions. For instance, it is essential to understand the flow over regular bedforms under oscillatory waves before we can adequately study the flow over irregular bedforms under unsteady forcing. Furthermore, the study of fundamental processes involved (such as flow) is important in order to describe related mechanisms (such as sediment transport and bed shear stress). Increased knowledge of all these physical processes can then be applied to improve modelling of large-scale processes such as coastal morphology and erosion.

The importance of bottom stress in wind-driven coastal circulation and its effects on wave dissipation in shallow waters has been discussed by many, notably *Grant and Madsen* (1986). In fact, *Ardhuin et al.* (2003) conclude that bottom friction, due to the presence of bedforms, plays a dominant role in wave energy dissipation over broad shallow shelves. Over symmetrical sand ripples, *Tunstall and Inman* (1975) determined that 7% of the total wave energy loss resulting from bottom effects is due to the generation and motion of vortices.

Direct measurements of stress over a fixed roughness bed using a shear plate have been made by *Riedel et al.* (1972). Furthermore, indirect stress measurements over these kinds of beds have also been obtained by *Sleath* (1987) and *Jensen et al.* (1989). Over mobile beds, direct measurements of stress are difficult to make, and, as a result, reliable flow measurements are needed to infer bottom stress. *Hay et al.* (2012c) obtained bed stress estimates over mobile beds in a laboratory setting. In addition, friction factors have been estimated from the vertical turbulent velocity over mobile beds using field measurements (*Smyth and Hay*, 2002; *Newgard and Hay*, 2007).

Three different methods are available for near-bed shear stress measurement: the momentum integral, Reynolds stress and the law-of-the-wall. Previously, there have been important differences in the stress estimates obtained using these methods. In fact, prior studies have concluded that one or more of the methods may yield unreliable results for stress estimates in oscillatory boundary layers. For example, *Sleath* (1987) obtained stress estimates over a fixed roughness bed via the Reynolds method that were significantly lower than those calculated using the momentum integral approach. Over a smooth bed, *Jensen et al.* (1989) conclude that their Reynolds stress estimates are also underpredicted. Over a fixed roughness bed, *Jensen* (1988) estimated bed friction factors using the law-of-the-wall that were consistent with earlier measurements, but obtained unreliable stress measurements using the vertical integral method. Furthermore, *Hay et al.* (2012c) obtained defect stress estimates over evolving sand ripples that were larger than the law-of-the-wall stress calculations, but smaller than Reynolds stress estimates. As a result, redundant and reliable stress measurements are still much needed.

Recently, new technologies have fuelled a renewed interest among researchers in investigating the wave bottom boundary layer over ripples. For example, particle image velocimetry (PIV) has been used for near-bed velocity measurement (*Nichols and Foster*, 2007; *van der Werf et al.*, 2007). In this technique, the flow is determined by using a camera to photograph small tracer particles (illuminated by a laser lightsheet) moving with the fluid. Furthermore, Laser Doppler Anemometry (LDA) has been used to measure fluid velocities near the bed (*Du Toit and Sleath*, 1981; *Sleath*, 1987). In addition, a number of studies have had success in using pulse-coherent Doppler for measuring flow and turbulence within the wave bottom boundary layer (*Hurther et al.*, 2011; *Hurther and Thorne*, 2011; *Hay et al.*, 2012a,b,c). Hence, the availability of better technology has been the driving force behind some of the more recent experimental work.

At the same time, advances in computational power and computational fluid dynamics techniques have allowed researchers to develop more accurate numerical models to simulate the flow over vortex ripples. For example, promising advances have been made using the

Reynolds Averaged Navier-Stokes (RANS) equations (*Marieu et al.*, 2008) and turbulence-resolving, i.e. large-eddy simulation (LES), techniques (*Chou and Fringer*, 2010). In addition, *Barr et al.* (2004) have used numerical simulations to investigate near-bed turbulence levels over different shapes of fixed ripples.

Given the current growing interest in investigating the wave bottom boundary layer, the present research is of immediate relevance to obtaining independent flow and stress measurements over equilibrium orbital-scale ripples. High-resolution flow measurements will be obtained using a state-of-the-art wide-band coherent Doppler profiler (MFDop). In doing so, the limits of the instrument will be tested in a laboratory setting as precursor to making field measurements under similar conditions. MFDop measurements will be used to investigate the development of the lee vortex at different phases of the forcing cycle and the co-evolution of Reynolds stress, turbulent kinetic energy and turbulence production. Shear stress will be calculated using several methods, so as to determine the approach which yields the most reliable results for orbital-scale ripples. The present work will thus provide accurate flow and stress measurements that can then be used to validate and improve current numerical models.

1.3 Objectives

The objectives of my thesis are:

- to measure the spatial structure of the near-bed flow and vorticity field over equilibrium orbital-scale ripples.
- to estimate stress within the turbulent oscillatory boundary layer over orbital-scale ripples using different methods.
- to investigate stress at a higher orbital excursion when the ripples are out of equilibrium.
- to test the MFDop's limits in a laboratory setting in order to evaluate whether the instrument is suitable for similar field conditions.

1.4 Thesis organisation

In order to address the outlined objectives, the thesis is organised as follows. Chapter 2 summarizes the theory of flow and stress in oscillatory boundary layers. Two solutions to the potential flow over a rippled bed are also presented. The experimental set-up and the MFDop instrument are described in chapter 3. The data analysis methods are also discussed in this chapter. The results and their discussion are presented in chapter 4. A summary of the results and the conclusions are given in chapter 5.

CHAPTER 2

THEORY

2.1 Oscillatory boundary layers over a flat bed

Determining the flow in the wave bottom boundary layer is essential to understanding the mechanics of sediment transport, which is of great importance in coastal engineering (*Nielsen*, 1992). The bottom boundary layer can be defined as the thin layer of fluid that is influenced by the bed (*Nielsen*, 1992). Let us define x and z as the horizontal and vertical coordinates, with u and w as the corresponding velocity components. The fluid density is given by ρ, p is pressure, τ^x is the shear stress in the x-direction and τ^z is the shear stress in the z-direction. The momentum equations are given by (*Kundu*, 1990)

$$\rho\left(\frac{\partial u}{\partial t}+u\frac{\partial u}{\partial x}+w\frac{\partial u}{\partial z}\right) = -\frac{\partial p}{\partial x}+\frac{\partial \tau^x}{\partial z} \tag{2.1}$$

$$\rho\left(\frac{\partial w}{\partial t}+u\frac{\partial w}{\partial x}+w\frac{\partial w}{\partial z}\right) = -\frac{\partial p}{\partial z}+\rho g+\frac{\partial \tau^z}{\partial x} \tag{2.2}$$

where the first term is the local acceleration and the second and third terms are referred to as the non-linear terms. For uniform oscillatory flow over a horizontal flat bed, the momentum equations in the boundary layer is (*Fredsoe and Deigaard*, 1992)

$$\rho\frac{\partial u}{\partial t} = -\frac{\partial p}{\partial x}+\frac{\partial \tau^x}{\partial z} \tag{2.3}$$

in the flow direction and

$$\frac{\partial p}{\partial z} = 0 \tag{2.4}$$

perpendicular to the flow direction. These equations arise by applying the boundary layer approximation to the momentum equations. The boundary layer approximation assumes that, within the boundary layer, the magnitude of the variations of the flow in the streamwise direction is much smaller than the magnitude of the variations across the boundary (*Kundu*, 1990). Since shear stresses are absent outside the boundary layer, the horizontal momentum equation within the interior is

$$\frac{\partial U_\infty}{\partial t} = -\frac{1}{\rho}\frac{\partial p}{\partial x} \tag{2.5}$$

where U_∞ is the free-stream velocity. Given that the horizontal pressure gradient $\partial p/\partial x$ is constant throughout the boundary layer (independent of z (equation 2.4)), the horizontal momentum equation for the boundary layer is

$$\frac{\partial u_d}{\partial t} = \frac{1}{\rho}\frac{\partial \tau^x}{\partial z} \tag{2.6}$$

where the defect velocity u_d is

$$u_d = u - U_\infty \tag{2.7}$$

and $\partial u_d/\partial t$ is the acceleration defect. It can be shown that equation 2.6 also holds for the boundary layer above an oscillating plate with no imposed flow in the interior (see appendix A).

Let the defect velocity within the bottom boundary layer be given by

$$u_d(t) = u_0(z)\sin[\omega t + \phi_0(z)] \tag{2.8}$$

where $u_0(z)$ and $\phi_0(z)$ are the amplitude and phase of the flow and ω is the angular frequency of the oscillation. A characteristic feature of oscillatory boundary layers is the fact that the velocity amplitude within the boundary layer overshoots the amplitude of the oscillatory flow in the interior (*Nielsen*, 1992). Since there is less inertia in the boundary layer than in the interior, the flow within the boundary layer responds faster to the varying pressure gradient (*van der Werf et al.*, 2007). Thus, the flow within the boundary layer reverses before that of the free-stream velocity.

Performing dimensional analysis on equation 2.6, using the friction velocity u_* as the velocity scale, with $\tau^x/\rho = u_*^2$ and $\partial/\partial t = \omega$, the scale height of the oscillatory boundary layer is $\delta \sim u_*/\omega$. In their analytical constant eddy viscosity model, *Christoffersen and Jonsson* (1985) define δ as

$$\delta = \kappa u_*/\omega \tag{2.9}$$

where $\kappa = 0.4$ is von Karman's constant. Using $\omega \sim 1$ radian/s for typical surface gravity waves having 5 to 20 s periods and $u_* \sim 10$ cm/s, the boundary layer thickness over a flat bed is expected to be of the order of a few centimetres.

Grant and Madsen (1986) emphasize the importance of bottom stress in wind-driven coastal circulation and its effects on wave dissipation in shallow waters. The bed friction factor f_w is defined as

$$f_w = 2\frac{{u_{*m}}^2}{{U_0}^2} \tag{2.10}$$

where u_{*m} is the maximum friction velocity and U_0 is the amplitude of the free-stream velocity. For turbulent oscillatory boundary layers,

$$f_w = f_w\left(\frac{r_h}{A}\right) \tag{2.11}$$

where A is the semi-excursion and r_h is the hydraulic roughness which, for fixed roughness flat beds, is proportional to grain size (*Nielsen*, 1992). Even though bottom friction has been the subject of numerous studies, reliable measurements of the bottom-friction coefficient for flow over mobile beds are scarce because measurements are difficult to make.

2.2 Irrotational Flow over a Rippled Bed

Determining the theoretical flow over ripples can be quite complex. In order to simplify the problem, the flow can be decoupled into two parts: an irrotational part and a rotational part. This section presents a solution to the potential flow over smooth-crested ripples according to *Davies* (1983) and over steep-crested ripples according to *Longuet-Higgins* (1981). Both solutions assume that the sediment-water interface is fixed and also neglect the effects of suspended sediment. In chapter 4, the flow field calculated from our laboratory results will be compared to both potential flow solutions.

2.2.1 Potential flow over smooth-crested ripples: *Davies* (1983)

Davies (1983) considered a two-dimensional, irrotational, deep flow over a small-amplitude sinusoidal bed extending to infinity in both positive and negative x directions (see Figure 2.1). Let the bed be given by

$$\zeta(x) = a \cos kx \tag{2.12}$$

where a is the ripple amplitude, $k = 2\pi/\lambda$ is the ripple wavenumber and λ is the ripple wavelength. *Davies* (1983) assumed that the unperturbed flow away from the bed is uniform and of strength U_0 in the positive x direction. Since the flow is irrotational, we can define a velocity potential Φ such that

$$u = \frac{\partial \Phi}{\partial x}; w = \frac{\partial \Phi}{\partial z} \tag{2.13}$$

where u and w are the horizontal and vertical components of the fluid's velocity. The velocity potential can be written as

$$\Phi(x, z, t) = \phi(x, z) \sin \omega t \tag{2.14}$$

where ω is the angular frequency.

Laplace's equation

$$\frac{\partial^2 \phi}{\partial x^2} + \frac{\partial^2 \phi}{\partial z^2} = 0 \tag{2.15}$$

must be satisfied in the flow domain. On the surface of the rippled bed, the kinematical condition (a fluid particle on the surface of the bed never leaves the surface) must also be satisfied: that is, at the bed $z = \zeta$,

$$\frac{D\zeta(x)}{Dt} = \cancelto{0}{\frac{\partial \zeta(x)}{\partial t}} + u \frac{\partial \zeta(x)}{\partial x} = w \tag{2.16}$$

Using equation 2.13, the kinematic boundary condition reduces to

$$-\frac{\partial \phi}{\partial x} \frac{\partial \zeta}{\partial x} + \frac{\partial \phi}{\partial z} = 0 \tag{2.17}$$

Davies (1983) expanded the velocity potential ϕ, as well as the ripple profile ζ, in a

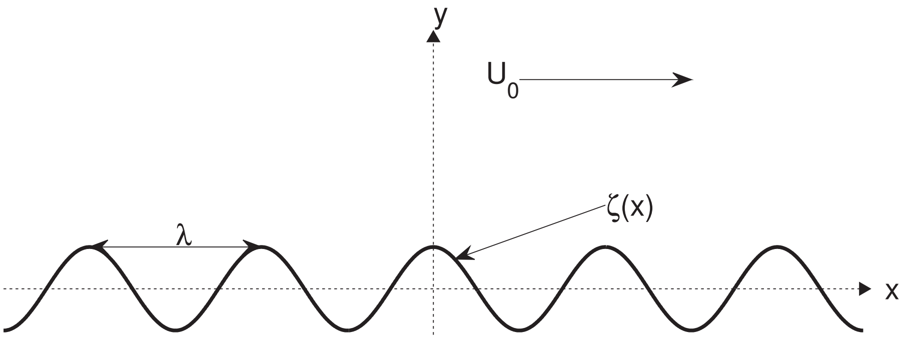

Figure 2.1: Ripple profile used in *Davies* (1983)

power series

$$\begin{aligned} \phi &= \alpha\phi_1 + \alpha^2\phi_2 + ... \\ \zeta &= \alpha\zeta_1 + \alpha^2\zeta_2 + ... \end{aligned} \tag{2.18}$$

where α is a small parameter. In doing so, the problem has now been simplified to a first-order solution representing the velocity potential existing in the absence of ripples and a second-order solution representing a perturbation. Using a Taylor series expansion, the boundary condition (equation 2.17) can be linearised and applied at the mean bed level ($z = 0$).

$$\left[-\frac{\partial\phi}{\partial x}\frac{\partial\zeta}{\partial x} + \frac{\partial\phi}{\partial z}\right]_{z=\zeta} = \left[-\frac{\partial\phi}{\partial x}\frac{\partial\zeta}{\partial x} + \frac{\partial\phi}{\partial z}\right]_{z=0} + ... \tag{2.19}$$

Combining equations 2.17 and 2.18, we get the following

$$-\frac{\partial}{\partial x}\left(\alpha\phi_1 + \alpha^2\phi_2 + ...\right)\frac{\partial}{\partial x}\left(\alpha\zeta_1 + \alpha^2\zeta_2 + ...\right) + \alpha\frac{\partial\phi_1}{\partial z} + \alpha^2\frac{\partial\phi_2}{\partial z} + ... = 0 \tag{2.20}$$

Thus, from 2.20, the problem to order α is

$$\frac{\partial\phi_1}{\partial z} = 0 \tag{2.21}$$

and Laplace's equation (2.15) becomes

$$\frac{\partial^2\phi_1}{\partial x^2} + \frac{\partial^2\phi_1}{\partial z^2} = 0 \tag{2.22}$$

Using both these equations, the solution to order α is

$$\phi_1 = U_0 x \tag{2.23}$$

where U_0 is the amplitude of the free-stream velocity far from the bed.

From 2.20, the problem to order α^2 is

$$-\frac{\partial \phi_1}{\partial x}\frac{\partial \zeta_1}{\partial x} + \frac{\partial \phi_2}{\partial z} = 0 \tag{2.24}$$

and Laplace's equation (2.15) is

$$\frac{\partial^2 \phi_2}{\partial x^2} + \frac{\partial^2 \phi_2}{\partial z^2} = 0 \tag{2.25}$$

The solution to Laplace's equation takes the form

$$\phi_2 = (Ae^{kz} + Be^{-kz}) \sin kx \tag{2.26}$$

where A and B are constants. Since ϕ_2 must exist away from the bed at $z = \infty$, $A = 0$. Equation 2.26 thus becomes

$$\phi_2 = Be^{-kz} \sin kx \tag{2.27}$$

Substituting ϕ_2 into equation 2.24,

$$U_0 ka \sin kx - Bke^{-kz} \sin kx = 0 \tag{2.28}$$

and at $z = 0$, we find that $B = U_0 a$. The solution to order α^2 is

$$\phi_2 = U_0 ae^{-kz} \sin kx \tag{2.29}$$

Thus, the overall solution correct to the second order is

$$\Phi = [\phi_1 + \phi_2] \sin \omega t = [U_0 x + U_0 ae^{-kz} \sin kx] \sin \omega t \tag{2.30}$$

Using equations 2.13, the velocity components are found to be

$$u = [1 + ake^{-kz}\cos kx]U_0 \sin\omega t \tag{2.31}$$

$$w = -U_0 ake^{-kz}\sin kx \sin\omega t \tag{2.32}$$

2.2.2 Potential flow over steep sand ripples: *Longuet-Higgins* (1981)

The bed profile used in *Longuet-Higgins* (1981) has sharper crests. *Longuet-Higgins* (1981) used a conformal transformation to map the ripple profile onto the sides of a regular polygon. The flow field (corresponding to the exterior of the polygon) is then mapped onto the interior of a unit circle.

Consider a series of ripples of wavelength λ in the complex z-plane given by

$$z = x + iy \tag{2.33}$$

where x and y are rectangular coordinates and the origin is located at a ripple crest. Using a conformal transformation (angles are preserved locally), the ripple sequence can be mapped onto the sides of a regular polygon. The vertices of the polygon represent the ripple crests and the interior angle at each crest is the same as the interior angle of the corners of the polygon. This transformation on the ζ-plane can be written as

$$\zeta = e^{-ikz} \tag{2.34}$$

where $k = 2\pi/P\lambda$ and P is an integer. Therefore, the origin ($z = 0$) in the z-plane corresponds to $\zeta = 1$ and the centre of the polygon ($\zeta = 0$) corresponds to $y \to -\infty$ in the z-plane. The interior of the polygon represents the sand and the exterior is the fluid. Similar to *Longuet-Higgins* (1981), a series of five ripples was mapped onto the sides of a pentagon ($P = 5$). The value 5 was chosen so that the ripple steepness of these theoretical ripples would be similar to those created in the laboratory experiments.

Using the following transformation, the exterior of the polygon can be mapped onto the interior of a unit circle.

$$\zeta = \zeta_0 - K \int_{W_0}^{W} \frac{(1 - W^P)^{2/P}}{W^2} dW \tag{2.35}$$

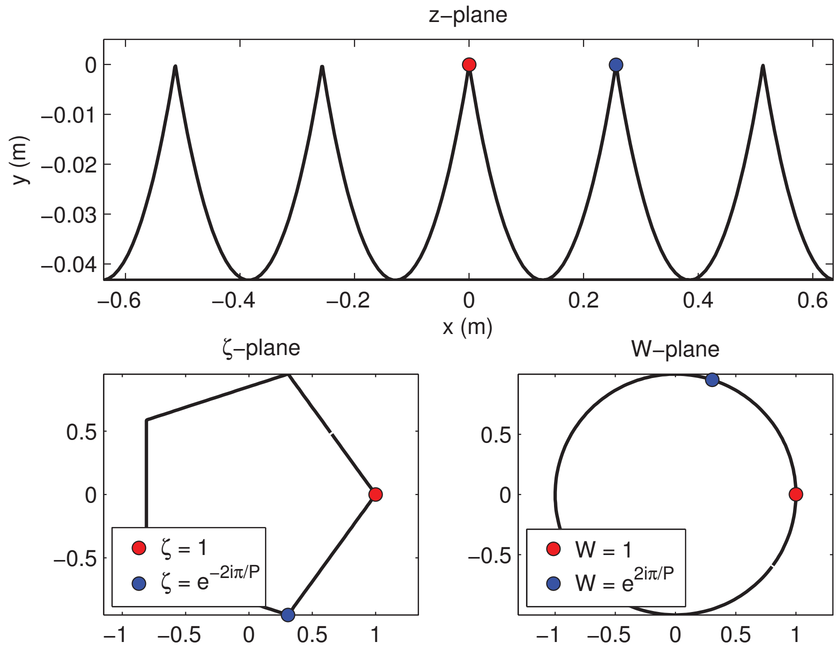

Figure 2.2: Ripple profile in the z-plane and transformed into a polygon in the ζ-plane and a circle in the W-plane. Two ripple crests are identified.

where ζ_0, W_0 and K are constants. In this plane, the exterior of the circle corresponds to the sand and the interior represents the water. W can be expressed as

$$W = \rho e^{i\alpha} \tag{2.36}$$

where $\rho = 1$ defines the unit circle. Lines of constant ρ are represented by concentric circles in the W-plane and by streamlines in the z-plane. Distance along a streamline is given by α. Using equation 2.35, K can be calculated by using $W_0 = 1$ and $W = e^{2i\pi/P}$, as well as their corresponding points in the ζ-plane: $\zeta_0 = 1$ and $\zeta = e^{-2i\pi/P}$. To avoid a singularity at $W = 1$, *Longuet-Higgins* (1981) suggested using $W_0 = e^{-i\pi/P}$ for numerical computations. The constant ζ_0 for this choice of W_0 was then determined using the point $\zeta = e^{-2i\pi/P}$ and its corresponding point in the W-plane mentioned earlier, as well as equation 2.35. Figure 2.2 shows the ripple sequence in all three planes. Two ripple crests are identified in the z-plane, as well as their corresponding points in the ζ and W-planes.

Longuet-Higgins (1981) assumed that the flow far from the bed is of uniform strength U_0 in the horizontal direction and has been started from rest impulsively. Since the flow is initially irrotational, a complex potential χ can be defined

$$\chi = \phi + i\psi \tag{2.37}$$

in such a way that far from the bed ($y \to \infty$),

$$\chi \sim U_0 z \tag{2.38}$$

In equation 2.37, ϕ is the velocity potential and ψ is the stream function. Combining equation 2.38 with equation 2.34, we get

$$\chi \sim (iU_0/k) \ln \zeta \tag{2.39}$$

Furthermore, for $W \ll 1$, equation 2.35 can be reduced to

$$\zeta \sim K/W \tag{2.40}$$

and, for $W \to 0$, equation 2.39 then becomes

$$\chi \sim (U_0/ik) \ln W \tag{2.41}$$

Longuet-Higgins (1981) thus suggested that the required initial flow is given by

$$\chi = (U_0/ik) \ln W \tag{2.42}$$

By substituting W from equation 2.36 in equation 2.42 and taking the imaginary part, the stream function is given by

$$\psi = -(U_0/k) \ln \rho \tag{2.43}$$

The streamlines in the z-plane, represented by curves of constant ρ, are plotted in Figure 2.3. The velocity potential given by the real part of χ is

$$\phi = \frac{\alpha U_0}{k} \tag{2.44}$$

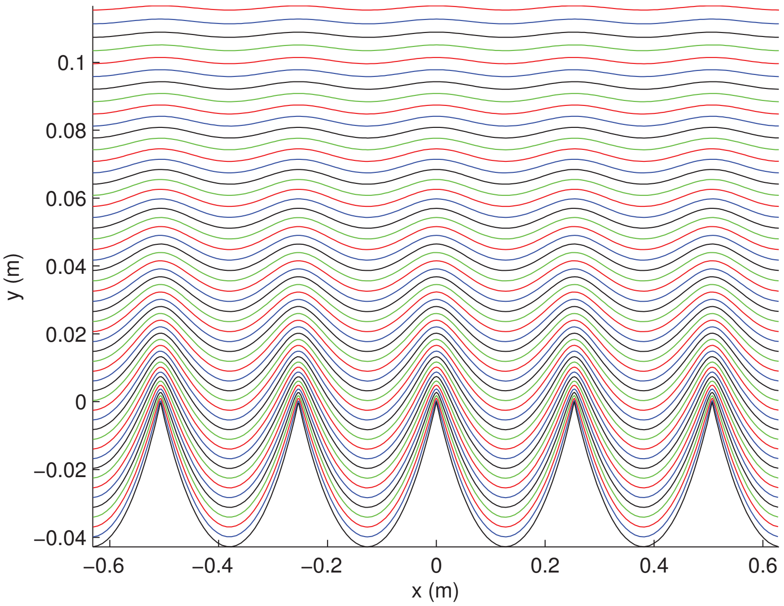

Figure 2.3: Streamlines in the z-plane calculated from the solution given by *Longuet-Higgins* (1981).

The flow field can then be calculated numerically by using the velocity potential

$$u = \frac{\partial \phi}{\partial x}; w = \frac{\partial \phi}{\partial y} \tag{2.45}$$

where u and w are the horizontal and vertical components of the flow.

2.2.3 Pressure gradient in potential flow

The boundary layer approximation is used in the defect stress estimate which will be discussed in section 2.4.1. However, this approximation may not be applicable over orbital-scale equilibrium ripples. Using the potential flow models, let us investigate the boundary layer approximation, and, consequently, the dependence of the pressure gradient field on height above the bed.

The pressure gradient ($\partial p/\partial x$) can be calculated using the momentum equation for horizontal flow over a frictionless bed.

$$\frac{\partial u}{\partial t} + u\frac{\partial u}{\partial x} + w\frac{\partial u}{\partial z} = -\frac{1}{\rho}\frac{\partial p}{\partial x} \tag{2.46}$$

For the potential flow solution suggested by *Davies* (1983), the pressure gradient can be calculated analytically using equations 2.31 and 2.32, whereas for the solution suggested by *Longuet-Higgins* (1981), the pressure gradient must be estimated numerically. For the model given by *Davies* (1983), the local acceleration is

$$\frac{\partial u}{\partial t} = \omega U_0[1 + ake^{-kz}\cos kx]\cos\omega t \tag{2.47}$$

and the non-linear terms are given by

$$u\frac{\partial u}{\partial x} = -ak^2e^{-kz}U_0^2[1 + ake^{-kz}\cos kx]\sin kx\sin^2\omega t \tag{2.48}$$

$$w\frac{\partial u}{\partial z} = a^2k^3e^{-2kz}U_0^2\cos kx\sin kx\sin^2\omega t \tag{2.49}$$

The pressure at the bed can also be determined using the time-dependent form of the irrotational Bernouilli equation (*Kundu*, 1990).

$$\frac{\partial\Phi}{\partial t} + \frac{1}{2}(u^2 + w^2) + \frac{p}{\rho} + gz = 0 \tag{2.50}$$

Considering that the velocity potential Φ can be written as

$$\Phi(x, z, t) = \phi(x, z)\sin\omega t \tag{2.51}$$

Bernouilli's equation (2.50) can be rewritten as

$$-\omega\phi'(x, z)\cos\omega t - \frac{1}{2}(u^2 + w^2) = \frac{p}{\rho} + gz - \omega U_0 x\cos\omega t \tag{2.52}$$

where $\phi'(x, z) = \phi(x, z) - U_0x$. Let the right-hand-side of the equation be referred to as p'/ρ and represent the dynamic pressure at the bed. The hydrostatic pressure is given by the gz term and $\omega U_0 x\cos\omega t$ term represents the part of the pressure field driving the mean flow.

The top panel in Figure 2.4 shows the pressure gradient field at $\omega t = 90°$ over ripples of wavelength and height similar to those in the experiments to be presented later. It can clearly be seen that the pressure gradient is not independent of height. Areas of alternating positive and negative pressure gradient that decay away from the bed are evident. The bottom panel shows the dynamic pressure at the bed. As expected, the dynamic pressure is negative over the crests and close to zero at the troughs. This result represents the typical behaviour of flow through a constriction where the static pressure of the fluid in question is reduced (*Kundu*, 1990). It was found that the pressure gradient field, as well as the dynamic pressure at the bed were similar when calculated numerically from the solution described by *Longuet-Higgins* (1981).

The pressure gradient field at 45° and the dynamic pressure at the bed are shown in Figure 2.5. Similar features of alternating negative and positive pressure gradient areas that decay away from the bed can be observed. The acceleration term has a $\cos\omega t$ dependence, whereas the non-linear terms have a $\sin\omega t$ dependence. As a consequence, the magnitude of these features is smaller at 45° than at 90°. Furthermore, far from the bed ($z \to \infty$), the only contribution to the pressure gradient field comes from the acceleration term. Since this term has a $\cos\omega t$ dependence, the pressure gradient field is non-zero far from the bed at 45° and close to zero at 90°. In addition, due to weaker velocities over the ripple crests, the dynamic pressure is also expected to be weaker over the crests at 45° than at 90°.

The acceleration term $\partial u/\partial t$ and the non-linear terms ($u\partial u/\partial x$ and $w\partial u/\partial z$) that were used in calculating the pressure gradient field (equation 2.50) at 45° are shown in Figure 2.6. Since the bed profile has a $\cos kx$ dependence (equation 2.12), crests are given by $kx = \pm 2\pi$, troughs are given by $kx = \pm(2n-1)\pi$ and zero-crossings are found at $kx = \pm(n+1/2)\pi$, where n is an integer. Thus, the $w\partial u/\partial z$ (equation 2.49) is zero over the zero-crossings due to its $\cos kx$ dependence. In addition, both non-linear terms (equations 2.48 and 2.49) are found to be zero over the crests and troughs due to their dependence on $\sin kx$. As a result, the main contribution to the pressure gradient term over the troughs and crests comes from the acceleration term. However, it is clear that the overall main contribution to the pressure gradient field along other parts of the ripple profile comes from the non-linear terms. This result has serious implications concerning the boundary layer approximation. The boundary layer approximation assumes that the magnitude of the variations of flow in the stream-wise direction is smaller than the magnitude of the variations across the boundary (*Batchelor*, 1967):

$$\left|\frac{\partial}{\partial x}\right| \ll \left|\frac{\partial}{\partial z}\right| \qquad (2.53)$$

This approximation also implies that the horizontal pressure gradient is independent of height. These assumptions are thus valid for a flat bed or a small-amplitude rippled bed where the boundary layer thickness is much smaller than the horizontal length scale of the variations in bed elevation. However, it is clear from Figure 2.5 (where the pressure

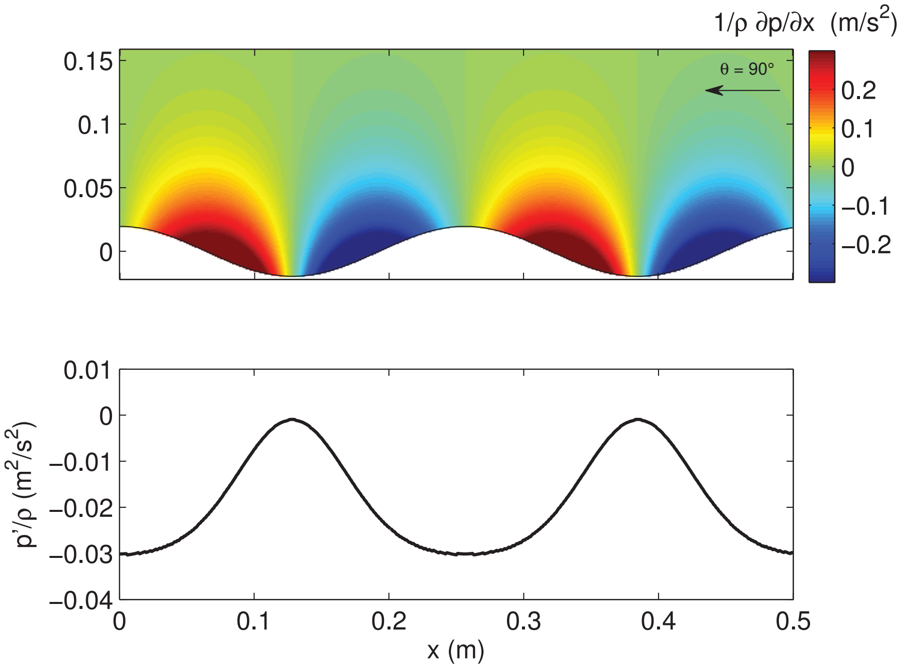

Figure 2.4: Top panel: pressure gradient field calculated analytically from *Davies* (1983) potential flow solution at 90°. Bottom panel: dynamic pressure $p' = p+\rho g z-\rho\omega U_0 x\cos\omega t$ at the bed.

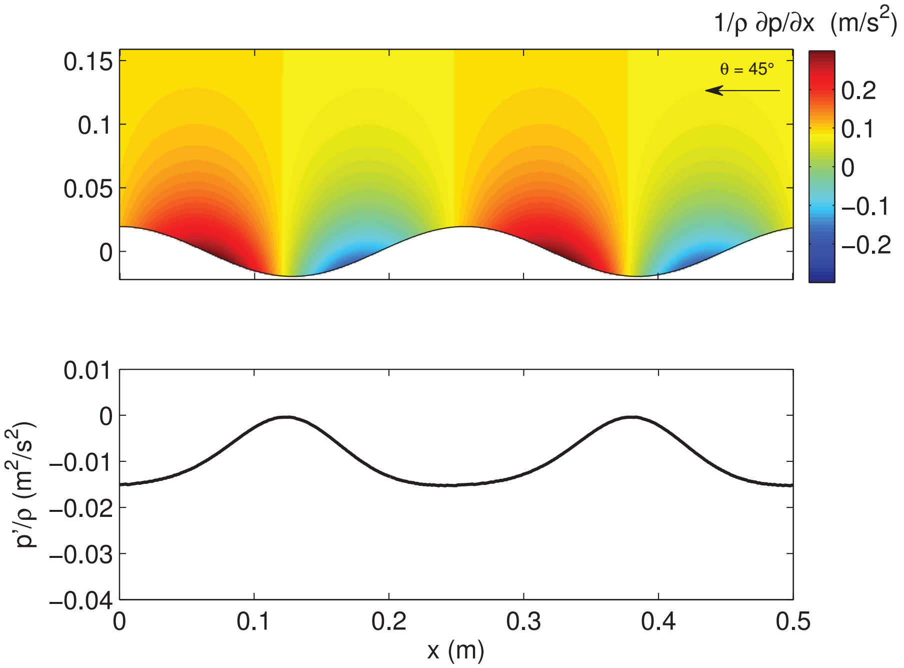

Figure 2.5: Top panel: pressure gradient field calculated analytically from *Davies* (1983) potential flow solution at 45°. Bottom panel: dynamic pressure $p' = p+\rho g z-\rho\omega U_0 x\cos\omega t$ at the bed.

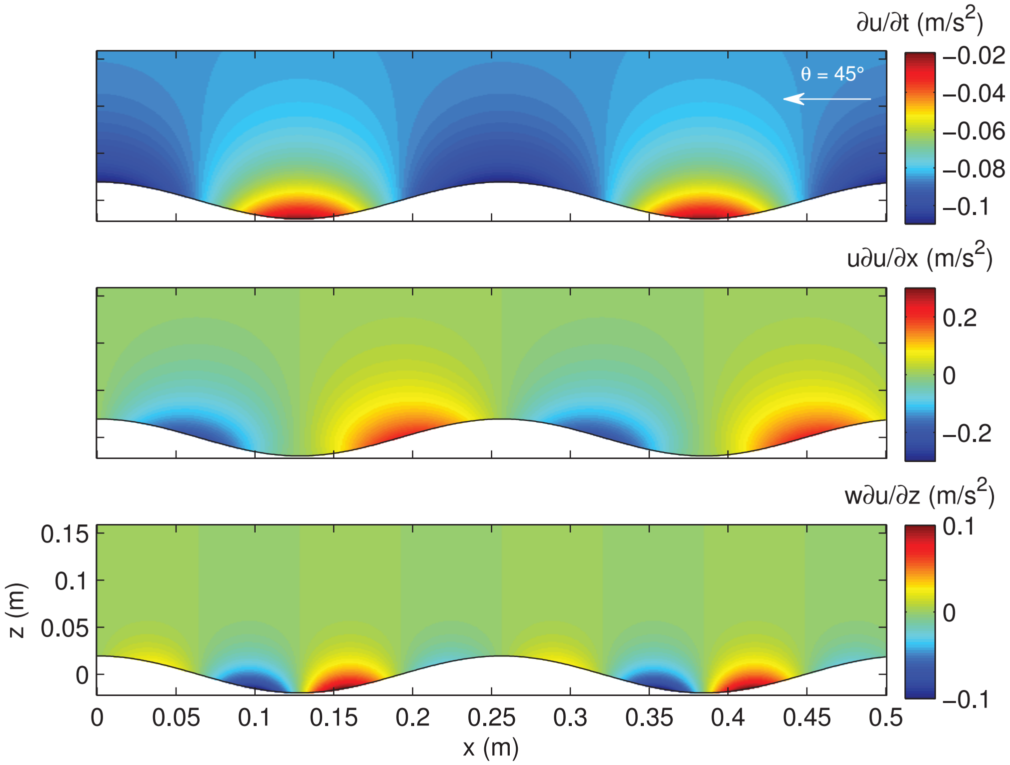

Figure 2.6: Contributions to the pressure gradient field at 45° calculated analytically from the solution given by *Davies* (1983). The acceleration term $\partial u/\partial t$ is shown in the top panel and the non-linear terms ($u\partial u/\partial x$ and $w\partial u/\partial z$) are shown in the middle and bottom panel.

distribution is dependent on the height above the bed) and Figure 2.6 (where the relative contribution of the non-linear terms are non-negligible) that this approximation may not hold over equilibrium orbital-scale ripples.

2.3 Rotational flow in oscillatory boundary layers over a rippled bed

The dynamics of the flow within the bottom boundary layer are strongly influenced by the shape of the sea bed. In fact, the presence of bed forms increases near-bed turbulence levels compared to flows over smooth beds (*Nielsen*, 1992; *Barr et al.*, 2004). In a numerical simulation of turbulent flow over fixed ripples, *Barr et al.* (2004) conclude that the distribution of turbulence becomes more focused over the troughs as ripple steepness increases. Based on the time-averaged turbulent kinetic energy, it was also found that the turbulent boundary layer thickness is dependent on ripple shape. Over sinusoidal ripples, the boundary layer is found to be thinner over the crests, with a "secondary thinning" over the troughs, whereas over steeper ripples, the boundary layer thickness becomes larger over the crests. As will be discussed in section 4.7, the variable thickness of the boundary layer over vortex ripples has important consequences for determining the bed shear stress using the law-of-the-wall.

A typical feature of the flow in oscillatory boundary layers over a rippled bed is the separation of the flow at or near the ripple crest, in which the flow next to the bed reverses direction. The flow accelerates up the ripple slope and decelerates as it descends on the other side. Due to the decrease of pressure in the direction of the flow, the flow adheres to the boundary upstream of the ripple crest. Downstream of the crest, the pressure increases, the flow next to the boundary reverses direction and flow separation occurs (*Kundu*, 1990). As a consequence, a region of reverse flow, sometimes referred to as a separation bubble, between the ripple crest and a point farther downstream in the trough is created (Figure 2.7). A vortex is thus defined in the lee of the ripple crest. As the free-stream velocity decelerates, the vortex is swept backwards over the crest and is ejected around the time of the free-stream flow reversal (*van der Werf et al.*, 2007).

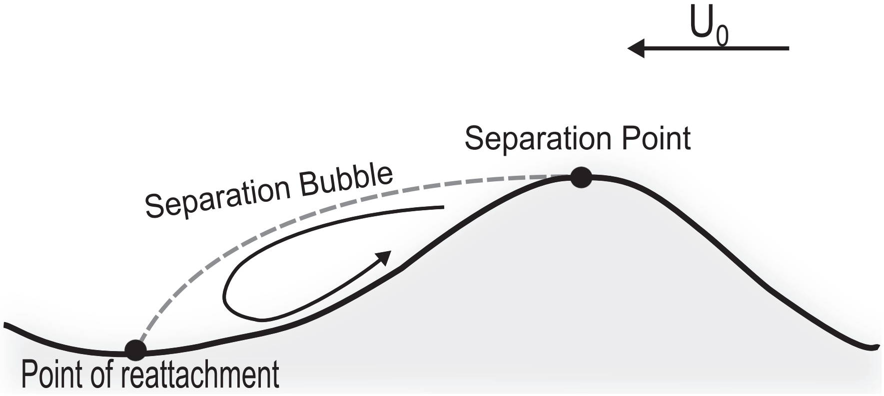

Figure 2.7: Sketch of the flow separation over a ripple. The separation point, the point of reattachment and the separation bubble are shown. The free-stream velocity (U_0) is indicated by an arrow.

2.3.1 Vorticity

Detailed observations of vortex dynamics over a rippled bed have been obtained numerically (*Blondeaux and Vittori*, 1991; *Barr et al.*, 2004) and experimentally (*Nichols and Foster*, 2007). However, redundant measurements are still needed in order to fully understand the generation and ejection of vortical structures over a rippled bed. The obtained results will lead to a better understanding of the mechanisms involved in the re-suspension of sediment grains and their transport (*Blondeaux and Vittori*, 1991).

Vorticity is defined as the curl of the flow field. The horizontal component of vorticity perpendicular to the xz plane and thus parallel to the ripple crests is given by

$$\zeta = \frac{\partial u}{\partial z} - \frac{\partial w}{\partial x} \tag{2.54}$$

2.4 Stress and turbulence in oscillatory boundary layers

In principal, different methods can be implemented to estimate the bed shear stress: the acceleration defect, the Reynolds stress, the law-of-the-wall, the bedform-induced stress and from the vertically-integrated vorticity equation.

2.4.1 Defect stress

Over a flat bed, shear stress can be obtained by vertically integrating the acceleration defect (equation 2.6) and assuming that the stress vanishes far from the bed, i.e. $\tau(\infty) = 0$.

$$\frac{\tau(z)}{\rho} = -\int_z^\infty \frac{\partial u_d}{\partial t} dz \tag{2.55}$$

The superscript on τ^x has been dropped. The stress estimates determined from this approach are referred to as the defect stress. However, in section 2.2.3, it was shown that over orbital-scale ripples, the boundary layer approximation likely does not hold. In fact, it was assumed that the horizontal pressure gradient is constant with depth throughout the boundary layer when obtaining the acceleration defect (equation 2.6). Thus, while equation 2.55 has been found to hold over flat beds (*Sleath*, 1987) and over smaller evolving ripples (*Hay et al.*, 2012c), it probably cannot be used over orbital-scale equilibrium ripples.

2.4.2 Reynolds stress

The Reynolds stress (the stress associated with the turbulent fluctuations) appears in the Reynolds-averaged Navier-Stokes equations (*Monin and Yaglom*, 1971). These equations are based on the Reynolds decomposition where a quantity θ is decomposed into its time-averaged part $\bar{\theta}$ and its fluctuating part θ'. Using primes to indicate turbulent fluctuations and an overbar to designate a time average, the vertical turbulent flux of horizontal momentum, or in other words, the turbulent shear stress, is

$$\frac{\tau(z)}{\rho} = -\overline{u'w'} \tag{2.56}$$

where $-\overline{u'w'}$ represents the Reynolds stress.

2.4.3 Law-of-the-wall

The law-of-the-wall, which can be obtained by dimensional analysis (*Monin and Yaglom*, 1971), is used in the third method of determining stress. Neglecting viscous effects, it assumes that the mean velocity gradient is only dependent on the bed shear stress τ_0, fluid density ρ and the vertical coordinate z. A unique combination of these parameters having the dimension of a velocity gradient can be formed

$$\sqrt{\frac{\tau_0}{\rho}}\frac{1}{z} = \frac{u_*}{z} \tag{2.57}$$

where the friction velocity $u_* = \sqrt{\tau_0/\rho}$. Thus,

$$\frac{\partial u(z)}{\partial z} \propto \frac{u_*}{z} \tag{2.58}$$

Therefore, the velocity distribution of the fluid near a boundary (but far enough away from the boundary for viscous effects to be neglected) exhibits a logarithmic dependence on z. From equation 2.58, the law-of-the-wall can be deduced and for our purposes takes the following form:

$$u(x, z, t) = \frac{u_*(x, t)}{\kappa} \ln(z'/z_0) \tag{2.59}$$

where z_0 is the roughness height, and $z' = z + \Delta z$, Δz being the displacement height (*Monin and Yaglom*, 1971) or zero-plane displacement (*Raupach*, 1992). The height above the bed at which the logarithmic velocity profile goes to zero is given by z_0. The presence of this logarithmic layer in turbulent oscillatory boundary layers over flat and fixed roughness beds has been verified experimentally by many, notably *Jensen et al.* (1989).

2.4.4 Bed shear stress from vorticity

The bed shear stress can be determined from the equation governing the rate of change of vorticity (*Kundu*, 1990). This equation is obtained by cross-differentiating the two-dimensional momentum equations for an incompressible fluid ($\nabla \cdot \vec{u} = 0$). The rate of change of the horizontal component of vorticity ζ is thus given by

$$\frac{\partial \zeta}{\partial t} + u\frac{\partial \zeta}{\partial x} + w\frac{\partial \zeta}{\partial z} = \frac{1}{\rho}\left[\frac{\partial^2 \tau^x}{\partial z^2} - \frac{\partial^2 \tau^z}{\partial x^2}\right] \tag{2.60}$$

and modifying,

$$\frac{\partial \zeta}{\partial t} + \frac{\partial}{\partial x}(u\zeta) + \frac{\partial}{\partial z}(w\zeta) = \frac{1}{\rho}\left[\frac{\partial^2 \tau^x}{\partial z^2} - \frac{\partial^2 \tau^z}{\partial x^2}\right] \tag{2.61}$$

where the τ^x and τ^z are the horizontal and vertical components of stress. If we assume that the stress is mainly in the horizontal direction ($\tau^x \gg \tau^z$) and that the horizontal length scales are much greater than the vertical length scales ($\partial(u\zeta)/\partial x \ll \partial(w\zeta)/\partial z$), equation 2.61 becomes

$$\int_z^\infty \left[\int_z^\infty \frac{\partial \zeta}{\partial t} dz + w\zeta\right] dz \simeq \frac{1}{\rho}\tau^x(z) \tag{2.62}$$

This approximation of horizontal length scales being greater than the vertical length scales is a valid assumption to make for orbital-scale ripples, which have a steepness of $\sim$0.2 (equation 1.2).

2.4.5 Bedform-induced shear stress

The bedform-induced shear stress appears in the double-averaged (time-space averaged) momentum equations (*Nikora et al.*, 2007a,b; *Mignot et al.*, 2009). The time-average of a flow variable is given by the average over time of an Eulerian measurement of flow at a specific Cartesian coordinate. In oscillatory flow, time-averaging refers to the average over time of a Eulerian measurement at a specific Cartesian coordinate and at a specific phase of the oscillation cycle.

The double-averaging procedure uses two kinds of spatial average: an intrinsic spatial average and a superficial spatial average. The intrinsic spatial average of a flow variable θ is given by

$$\langle\theta(x, y, z, t)\rangle = \frac{1}{A_f}\int\limits_{A_f} \theta(x, y, z, t)dA \tag{2.63}$$

and the superficial spatial average is given by

$$\langle\theta(x, y, z, t)\rangle_s = \frac{1}{A_0}\int\limits_{A_f} \theta(x, y, z, t)dA \tag{2.64}$$

where A_f is the area occupied by the fluid, which excludes the space occupied by the roughness elements, within the total area A_0 (*Nikora et al.*, 2007a,b). These two averages are related by the roughness geometry function $\Psi(z) = \langle\theta\rangle_s/\langle\theta\rangle = A_f/A_0$. Above the roughness elements, $\Psi(z) = 1$ and, at the bed, $\Psi(z) = 0$. The averaging area is chosen to be a slab of fluid close to the bed that is larger than the length scale of the roughness elements, but smaller than the overall bed geometry such as bed slope (*Mignot et al.*, 2009).

The double-averaged momentum equations use the Reynolds decomposition $\theta = \bar{\theta} + \theta'$ for instantaneous variables and the decomposition $\bar{\theta} = \langle\bar{\theta}\rangle + \tilde{\theta}$ for time-averaged variables. The spatial fluctuation in the time-averaged variable, denoted by the tilde overbar, is given by $\tilde{\theta} = \bar{\theta} - \langle\bar{\theta}\rangle$.

The double-averaging can be executed in two steps: time-average the momentum equations using the Reynolds decomposition and then spatially-average the result. The double-averaging procedure can also be performed in a single operation (*Nikora et al.*, 2007a). Compared to the conventional Reynolds-averaged momentum equations, a new term representing the bedform-induced shear stress appears in the double-averaged equations:

$$\frac{\tau(z)}{\rho} = -\langle \tilde{u}\tilde{w} \rangle_s \tag{2.65}$$

This stress is due to the spatial variations in the time-averaged flow, whereas the Reynolds stress is associated with temporal fluctuations in the flow field (*Nikora et al.*, 2007a).

2.4.6 Turbulence

Another measurement in bottom boundary layers is the turbulent kinetic energy (TKE), which represents the kinetic energy associated with the fluctuating motion (*Monin and Yaglom*, 1971). Turbulent kinetic energy is given by

$$TKE = \frac{1}{2}(\overline{u'^2} + \overline{v'^2} + \overline{w'^2}) \tag{2.66}$$

where the primes denote velocity fluctuations. Over orbital-scale ripples, the TKE will be a measure of the turbulence generated by the lee vortex. From the Reynolds-averaged Navier-Stokes equations, a term representing the production of turbulent kinetic energy arises and is given by the product of Reynolds stress and vertical shear (*Monin and Yaglom*, 1971).

$$prod = -\rho\overline{u'w'}\frac{\partial u}{\partial z} \tag{2.67}$$

2.5 Hydraulic roughness of rippled beds

The hydraulic roughness is a measure of the roughness scale relative to the orbital excursion, and is related to the friction factor. For a flat bed of densely packed particles under oscillatory flow, the hydraulic roughness is proportional to the grain diameter (*Nielsen*, 1992). For a rippled mobile bed, *Nielsen* (1992) suggests that the hydraulic roughness be given by the sum of the roughness of a rigid ripple profile and the roughness contribution due to moving sand grains over the ripples. The former must be dependent on ripple height and ripple steepness. From *Nielsen* (1992), the hydraulic roughness over rippled beds under oscillatory flow is

$$r_h = \frac{8\eta_0^2}{\lambda} + 170\sqrt{\theta_{2.5} - 0.05}D_{50} \tag{2.68}$$

where $\eta_0 = 2a$ is the ripple height and the grain roughness Shields parameter is given by

$$\theta_{2.5} = \frac{f_{2.5}(A\omega)^2/2}{(s-1)gD_{50}} \tag{2.69}$$

and the grain roughness friction factor is

$$f_{2.5} = \exp[5.213(2.5D_{50}/A)^{0.194} - 5.977] \tag{2.70}$$

and where $A = d_0/2$ is the semi-excursion.

CHAPTER 3

APPARATUS AND METHODS

3.1 Experimental set-up

Figure 3.1 shows the details of the RippleKart setup used in *Hay et al.* (2012a,b,c). A Scotch yoke assembly drives the Kart. Rotary motion of the drive arm is converted to rectilinear 10-s period sinusoidal oscillations parallel to the tank's long axis. In order to avoid any sideslip, the RippleKart is equipped with guide wheels that travel along the centre guide rail. A 2.4 m long by 0.8 m wide tray with faired end pieces is suspended from the Kart. These end pieces retain the sand, and the faired surfaces minimize end effects on ripple evolution. Quartz sand (industrial blasting sand) was placed on the tray to a thickness of approximately 10 cm. The sand size distribution (see Figure 3.2) was determined by mechanical sieving. The median grain size D_{50} was 153 μm. The 16% and 84% coarser than sizes (D_{16} and D_{84}) were 215 μm and 106 μm respectively. A depression to help initiate the formation of two-dimensional ripples was created on the initially flat bed before the RippleKart was started. The RippleKart was then run for a little under 12 hours, allowing the ripples to develop until a stable (equilibrium) ripple profile was obtained. Figure 3.3 shows the evolution of the bed during one of the RippleKart test runs.

A wide-band coherent Doppler profiler (MFDop) was mounted underneath the centre guide rail with the centre transducer facing the bed, and remained stationary as the Kart passed beneath it. Once a stable ripple profile was obtained, the data were collected at as many as six different MFDop positions (see Table 3.1). For the first run, the instrument head was positioned directly over a ripple crest at maximum Kart speed. The MFDop was then repositioned for the subsequent runs over an adjacent ripple trough and half-way

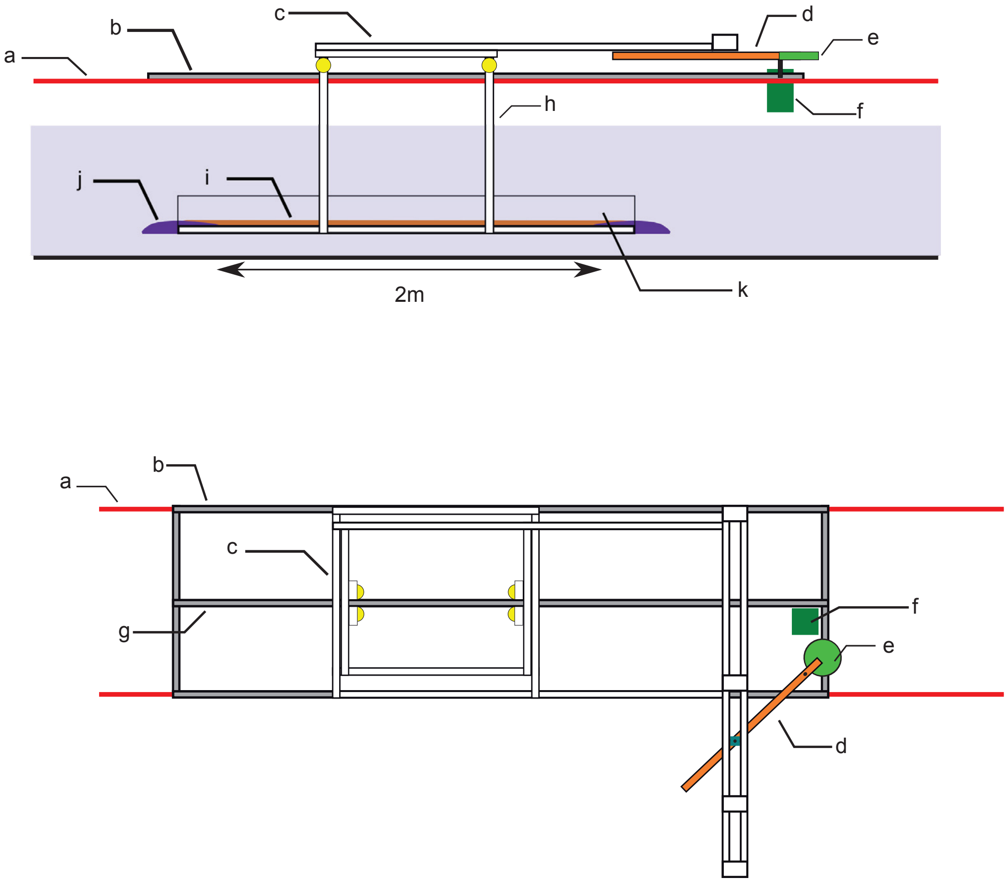

Figure 3.1: Sketch of the RippleKart apparatus. Top panel (side view) and bottom panel (top view) showing a. top of tank sidewalls; b. side rails; c. Kart; d. drive arm; e. counterweight; f. drive motor; g. centre guide rail (bottom panel only); h. downriggers (top panel only); i. bed (top panel only); j. fared end-pieces (top panel only); k. tray sidewalls (top panel only). From *Hay et al.* (2012a).

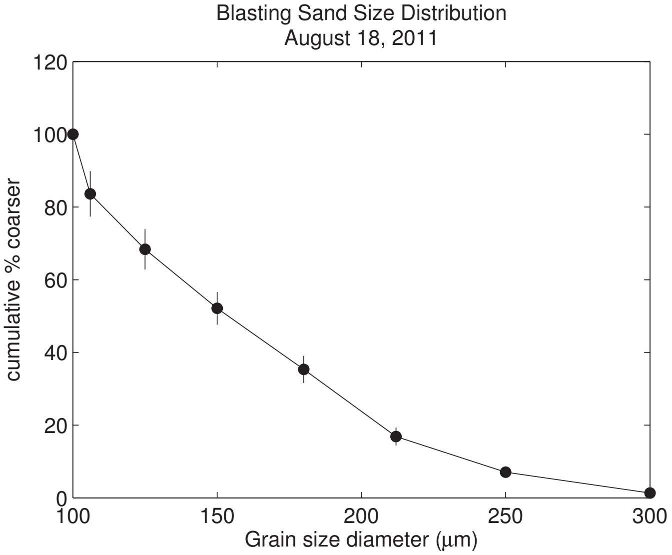

Figure 3.2: Sand size distribution: mean and standard deviation from 3 replicates. The points indicate the cumulative percentage of mass coarser than the indicated grain size diameter.

between the ripple crest and trough. These data were then combined in order to determine the flow field over one full ripple profile. These measurements were also made over a new bed of ripples at a similar RippleKart excursion ($d_0 = 49.6$ cm) and at a higher excursion ($d_0 = 60.5$ cm).

Using a gravity-fed system, a mixture of agricultural lime and water from a mechanically-stirred reservoir was continuously injected into the water close to the MFDop's centre transducer to increase the number of scatterers in the water, and thereby the pulse-pair correlations. In order to remove larger particles with high settling velocities, the lime was

Table 3.1: MFDop head positions for different RippleKart excursions

	d_0 = 49.8 cm	d_0 = 49.6 cm	d_0 = 60.5 cm
zero-crossing	-	-15.65 cm	-
trough	-	-11.34 cm	-
zero-crossing	-6.5 cm	-5.81 cm	-5.81 cm
crest	0 cm	0 cm	0 cm
zero-crossing	6.8 cm	4.40 cm	4.40 cm
trough	13.6 cm	8.80 cm	-

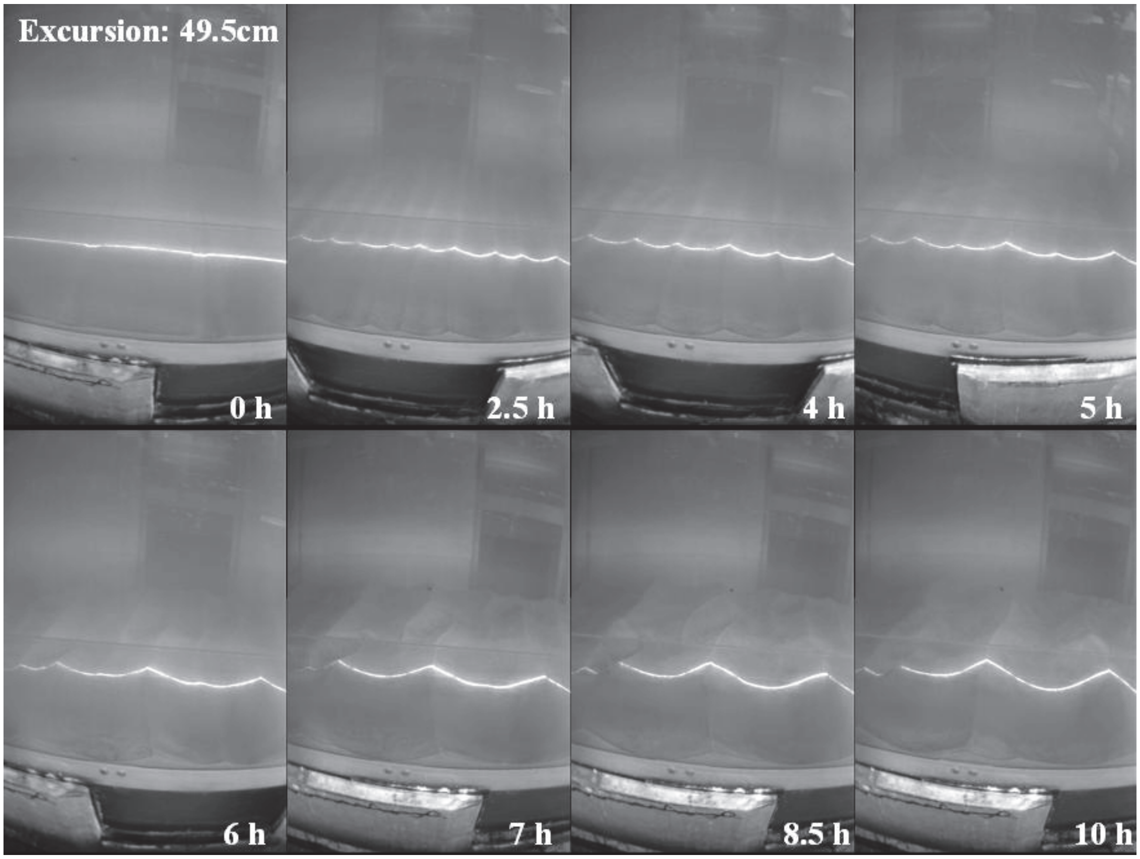

Figure 3.3: Ripple evolution for one of the RippleKart test runs at an excursion of 49.5 cm. The camera was mounted to the RippleKart, but outside the tank. A laser light sheet helps define the ripple profile.

dry-sieved using a sieve with 0.177 mm openings. A Nortek Vectrino (acoustic Doppler velocimeter) was used to measure the flow in the interior far from the bed. The use of this instrument was necessary to account for the flow induced by the displacement of water by the sediment-laden tray. The Vectrino was mounted to the centre guide rail and was positioned next to the MFDop head. The Kart motion was measured using an in-air acoustic travel time sensor (PASCO Motion Sensor II) and an aluminium flat plate reflector mounted to the Kart.

3.2 The MFDop

Near-bed flow measurements over the orbital-scale ripples created with the RippleKart apparatus were obtained using the wide-band coherent Doppler profiler (MFDop) described in *Hay et al.* (2012a,b,c).

3.2.1 Pulse-coherent acoustic Doppler sonar

Reliable measurements of velocity profiles and sediment transport within the oscillatory bottom boundary layer are scarce, as stated by *Grant and Madsen* (1986) in their review of continental-shelf bottom boundary layers. Hence, the need for robust instrumentation capable of making these measurements without disturbing the flow near the bed or the bed itself have led to the development of pulse-coherent acoustic Doppler sonar for making high-resolution measurements of the flow and turbulence within the bottom boundary layer (*Hay et al.*, 2012a; *Hurther et al.*, 2011; *Hurther and Thorne*, 2011). This technology works well in high suspended sediment conditions since scatterers are abundant.

In pulse-to-pulse coherent Doppler, the instantaneous velocity of a moving particle is based on the rate of change of the phase of sound scattered from a detected volume at a fixed range. The velocity accuracy depends on the degree of coherence between successive pulses (*Zedel and Hay*, 1999). The ensemble-averaged complex correlation between consecutive pulses $\bar{R}$ is thus a fundamental measurement of pulse-to-pulse Doppler and takes the following form as implemented in the MFDop (*Hay et al.*, 2012c),

$$\bar{R} = \frac{1}{\sigma^2} \sum_{j=1}^{N-1} z_j^* z_{j+1} \tag{3.1}$$

where $z_j = a_j \exp(i\varphi_j)$ is the complex amplitude of the return signal from the jth

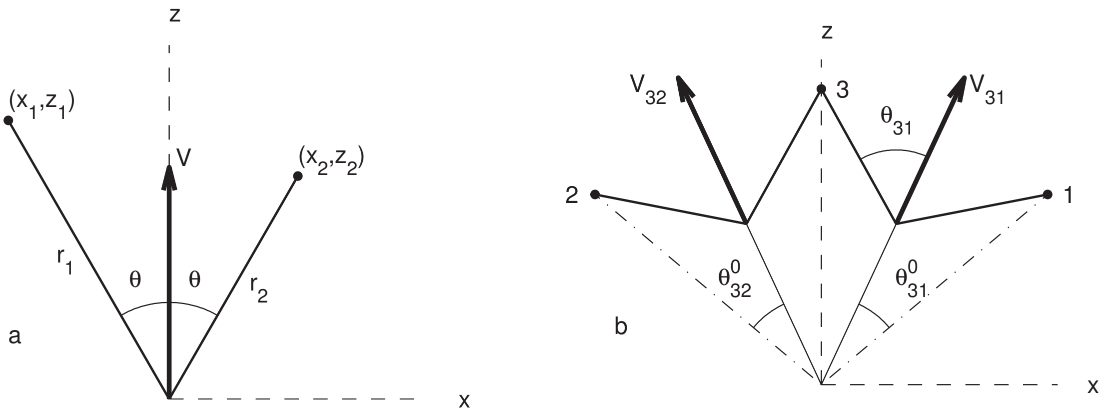

Figure 3.4: (a) Schematic bistatic geometry and (b) Symmetric isosceles geometry used in the MFDop from *Hay et al.* (2012a).

pulse, φ_j is its phase and * represents a complex conjugate. The normalization factor $\sigma^2 = \sum |a_j||a_{j+1}|$, and is related to the amplitude variance. Thus, $\bar{R}$ can be expressed as

$$\bar{R} = \frac{1}{\sigma^2} \sum_{j=1}^{N-1} a_j^* a_{j+1} e^{i(\varphi_{j+1} - \varphi_j)} \tag{3.2}$$

The phase of the return signal from a scatterer located at r_j is $\varphi_j = 2kr_j$, where k is the acoustic wavenumber. The difference in phase for two pulses is $\Delta\varphi = 2k\Delta r$ and the variation of the change of phase over time is $\Delta\varphi/\Delta t = 2kV$. The velocity V can thus be expressed as a function of the mean phase difference $\Delta\varphi$ among a suitable number of consecutive pulse pairs

$$V = \frac{\Delta\varphi}{2k\tau} \tag{3.3}$$

where τ is the pulse repetition interval.

Since the mean phase difference is calculated using the arctangent of the ratio of imaginary and real parts of the complex signal autocovariance R (*Lhermitte and Serafin*, 1984), $\Delta\varphi$ is bounded by $\pm\pi$. As a consequence, phase wraps occur at $\pm\pi$ and an ambiguity velocity $V_a = \pm\pi/2k\tau$ can be defined.

In a bistatic geometry (Figure 3.4a), a transmitter and a receiver are located at a distance r_1 and r_2 from the origin. For a particle situated at the origin, the phase of the scattered pulse is $\varphi = kr_1 + kr_2$. Using θ as the bisector angle, the velocity component along the bisector for small displacements of the scatterer is given by

$$V = \frac{\Delta\varphi}{2k\tau\cos\theta} \tag{3.4}$$

and hence the velocity ambiguity is

$$V_a = \frac{\pi}{2k\tau\cos\theta} \tag{3.5}$$

As a result, the observed velocity can be expressed as a function of the ambiguity velocity

$$V = \frac{\Delta\varphi}{\pi}V_a \tag{3.6}$$

The bistatic geometry used in the MFDop is sketched in Figure 3.4b. The two receive-only transducers (1 and 2) and the transmit transducer (3) are indicated. The detected velocities V_{31} and V_{32} are the projections of the flow along the bisectors between each of the outboard transducers and the centre transducer (*Hay et al.*, 2012a) and are given by

$$V_{31} = u\sin\theta^0_{31} + w\cos\theta^0_{31} + \epsilon_1 \tag{3.7}$$

$$V_{32} = -u\sin\theta^0_{32} + w\cos\theta^0_{32} + \epsilon_2 \tag{3.8}$$

where ϵ represents noise and u and w are the Cartesian velocity components. These velocities can be solved to obtain u and w:

$$u = \left[\frac{V_{31}}{\cos\theta^0_{31}} - \frac{V_{32}}{\cos\theta^0_{32}} - \frac{\epsilon_1}{\cos\theta^0_{31}} + \frac{\epsilon_2}{\cos\theta^0_{32}}\right][\tan\theta^0_{31} + \tan\theta^0_{32}]^{-1} \tag{3.9}$$

$$w = \left[\frac{V_{31}}{\sin\theta^0_{31}} + \frac{V_{32}}{\sin\theta^0_{32}} - \frac{\epsilon_1}{\sin\theta^0_{31}} - \frac{\epsilon_2}{\sin\theta^0_{32}}\right][\cot\theta^0_{31} + \cot\theta^0_{32}]^{-1} \tag{3.10}$$

Similarly, the detected velocities V_{35} and V_{36} in the transverse direction between the orthogonal pair of outboard transducers can be determined. The cross-tank velocity v (perpendicular to the RippleKart motion and parallel to the ripple crests) can then be calculated from these observed velocities.

Following *Hay et al.* (2012b) and defining primes to denote fluctuations relative to a mean, the Reynolds stress can be estimated from the detected velocity fluctuations:

$$-\overline{u'w'} = \frac{\overline{V_{32}'^2} - \overline{V_{31}'^2}}{\sin\theta_{31}^0 + \sin\theta_{32}^0} + ... \tag{3.11}$$

where the second-order statistics $\overline{u'^2}$ and $\overline{w'^2}$ are considered to be the same at the two measurement points. This requires that the time-averaged turbulent energy be uniform on horizontal scales comparable to the beam bisector separation. For the MFDop, the separation between the beam bisectors is of the order of a few centimetres (see Appendix B).

3.2.2 The MFDop

The MFDop consists of a centre transducer, which can transmit and receive, and four outboard transducers that only have receive capabilities. As stated by *Hay et al.* (2012a), all the transducers in the MFDop have similar beam patterns and beamwidths. Other bistatic geometries have a centre transmit beam that has a different width than the outboard receive beams. However, since both the transmit and outboard receive beamwidths are narrow, the isosceles geometry implemented in the MFDop allows a higher signal-to-noise ratio in the beam overlap region. The MFDop beam axes intersect at a range of 40 cm and have an overlapping region that extends 10 to 15 cm above and below this point. Due to the MFDop geometry, there is a difference in range along the vertical beam and the beam bisectors. Thus, the measurements registered by each transducer must be interpolated onto the centre transducer's vertical range (see Appendix C for details).

The MFDop operates in the $\sim$1.2 to $\sim$2.3 MHz frequency band and has the capacity to operate in single-frequency and multi-frequency modes. Since different frequencies have distinct velocity ambiguities, multiple frequencies are used to resolve the velocity ambiguities (*Hay et al.*, 2008; *Zedel and Hay*, 2010). A sketch of the MFDop transmit pulse in dual-frequency mode is shown in Figure 3.5. The vertical size of the detected volume (i.e. range bins) is given by half the transmit pulse length. Hence, high spatial resolution is achieved by using short pulses.

A typical feature of oscillatory boundary layers is the fact that the velocity amplitude near the top of the bottom boundary layer overshoots (is larger than) the amplitude of the oscillatory flow in the interior. For measurements over a fixed gravel bed, an observed velocity overshoot of 4 to 8$\%$ and a maximum phase lead of 18° to 19° were obtained by

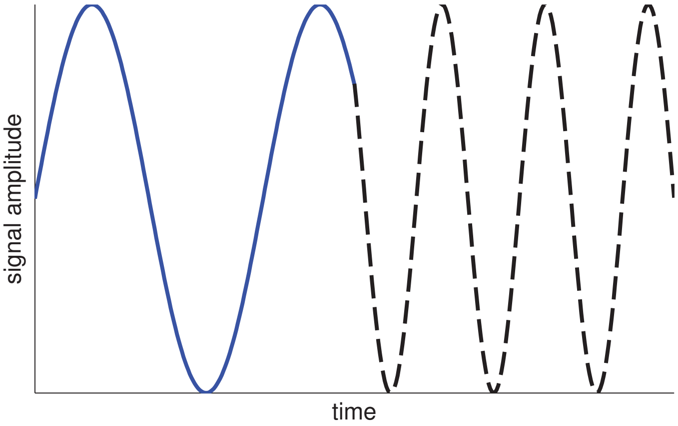

Figure 3.5: MFDop transmit pulse sketch in dual frequency mode. The transmit pulse is composed of two frequencies indicated by the blue and black lines.

Hay et al. (2012a). These values are comparable to measurements made by *Sleath* (1987) using Laser Doppler Anemometry. Furthermore, *Hay et al.* (2008) showed that MFDop measurements of flow within a turbulent wall jet agreed favourably with independent velocity measurements acquired using a Nortek Vectrino.

MFDop amplitude calibration experiments were carried out as part of testing improvements to the analog electronics in the instrument. The experiments used the jet tank setup described in *Hay* (1991). The backscatter amplitude from the jet was measured as increasing quantities of blasting sand were added. One-litre suction samples were filtered and the dried sand was then weighed in order to obtain concentration measurements. At frequencies for which attenuation is negligible (lower frequencies), the squared mean backscatter amplitude was found to be linearly proportional to particle concentration, which is similar to results obtained by *Hay* (1991). As sensitivity improvements were made to the system, curves of the maximum mean squared amplitude of the signal as a function of concentration were used to quantify the improvement.

The MFDop operating parameters used during the RippleKart experiments are listed in Table 3.2. Data from runs using a pulse length of 4 μs and 2 μs were compared, where the MFDop was operated in dual-frequency mode. It was found that the data using a 4 μs pulse length have higher signal correlations away from the bed. It is important to note that the bandwidth of the digital filters of the receivers in the system matches the bandwidth of the transmit pulse. Noise levels increase for shorter pulse lengths due to the increased

Table 3.2: MFDop operating parameters

Parameter	Value
ensemble acquisition rate	42.4 Hz
frequency 1	1.35 MHz
frequency 2	1.8 MHz
pulse duration	4 μs
pulse pairs per ensemble	20
range resolution	3 mm
transmit amplitude	100 $\%$

bandwidth. Furthermore, a longer pulse length increases the vertical extent of the detected volume, which in turn can also lead to higher signal correlations, especially at low scatterer concentrations. As a result, for these experiments, a pulse length of 4 μs was used. Also, it was found that using 20 pulse pairs per ensemble average instead of 10 is preferable. In this case, less noise is present in the data set since it is averaged over more points.

3.3 Synchronisation

The output signals acquired from the different instruments should ideally be synchronous; i.e. on a common time base. However, there is a potential latency between the collected data and their transfer to the computer. The following section examines the synchronisation between the MFDop and the Vectrino.

3.3.1 Time delay

In order to determine the time delay between the Vectrino and the MFDop, an experiment was conducted over a flat bed using the RippleKart apparatus. A steel rod (1/16 inch diameter) was attached to the RippleKart in such a way that it passed through both the Vectrino detected volume and the MFDop vertical beam. The RippleKart was then run for $\sim$10 cycles at an excursion of 17.2 cm.

In order to determine the Kart velocity, a sine wave was fit to the low-pass filtered Pasco data (cut-off frequency of 1 Hz). From this fit, the first zero-upcrossing of each cycle of the Kart motion was determined. The Vectrino amplitude data were low-pass filtered using a cut-off frequency of 1.2 Hz. Both the Vectrino data and the MFDop amplitude

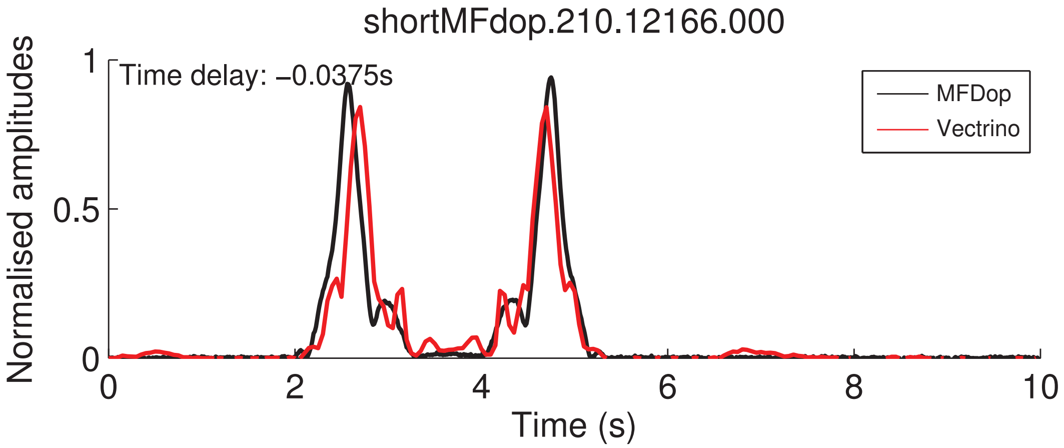

Figure 3.6: Example data for the time delay experiment. Normalised amplitude measurements averaged over several cycles from the MFDop (black) and Vectrino (red) are compared.

measurements from the centre transducer were averaged over several cycles. The averaged normalised amplitude measurements registered by the MFDop and the Vectrino are shown in Figure 3.6. The two amplitude spikes represent the signal reflected from the bar as it passed beneath the instruments during each half-cycle. The peaks occur at different times for each instrument.

In calculating the time delay, the fact that the MFDop and the Vectrino might not be perfectly aligned along the axis of the steel rod was taken into account as follows. The time delay for each half cycle (Δt_1, Δt_2) is given by

$$\Delta t_1 = \delta + \frac{\Delta x}{u_{K0}} \tag{3.12}$$

$$\Delta t_2 = \delta - \frac{\Delta x}{u_{K0}} \tag{3.13}$$

where δ is the time delay that must be added to correct the Vectrino time base, Δx is the difference in position between the two instruments and u_{K0} is the amplitude of the Kart velocity. Δt for each half-cycle was determined by finding the time difference between the maximum of the averaged backscatter amplitude measured using the MFDop and Vectrino. The time delay is given by

$$\delta = \frac{\Delta t_1 + \Delta t_2}{2} \tag{3.14}$$

The overall time delay was calculated by averaging over the time delays for seven repeat runs. It was found to be -0.05 ± 0.01s. The negative sign indicates that the MFDop led the Vectrino.

3.4 Analysis

3.4.1 Phase-averaging

The phase average $\overline{\xi_j}$ of a quantity ξ at time t_j over N_c cycles is given by

$$\overline{\xi_j} = \frac{1}{N_c} \sum_{i=1}^{N_c} \xi \left(t_j + (i-1)T \right) \tag{3.15}$$

where T is the oscillation period. Following *Hay et al.* (2012a), only the MFDop data from cycles having a cycle-mean correlation away from the bed (38 cm to 41 cm from the centre transducer) exceeding 85% were included in the phase-averaging. The phase-averaged velocities u, v and w were computed from the range-corrected phase-averaged V's using equations 3.9 and 3.10.

The time delay discussed in section 3.3.1 was based on equations 3.12 and 3.13. These equations assume that the amplitude of the Kart velocity u_{K0} is the same for both half-cycles, or in other words, that the Kart motion u_K is symmetric. This assumption was verified by calculating the residual between the low-pass filtered Kart motion and the best-fit sinusoid. As Figure 3.7 illustrates, this residual was found to be very small (O(1) mm/s) and lacking a distinct pattern, verifying that u_K was nearly sinusoidal.

3.4.2 Kart velocity

Using the backscatter amplitude A_j from the centre transducer, the amplitude-weighted mean range r_b to the bottom was calculated over the range interval of the bottom return.

$$r_b = \frac{\sum A_j r_j}{\sum A_j} \tag{3.16}$$

The velocity of the bottom, and as a consequence the Kart motion, was determined by calculating the velocity at r_b. The best-fit sinusoid to the MFDop time series (~40 cycles) was obtained using

$$u(r_b, t_j) = a \sin \omega_K t_j + b \cos \omega_K t_j \tag{3.17}$$

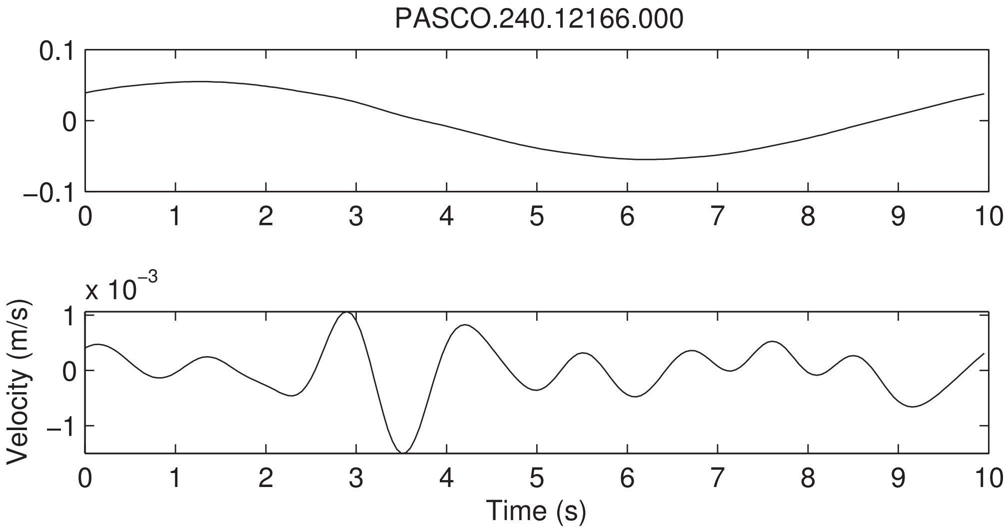

Figure 3.7: Example of velocity data collected using the Pasco. Top panel: phase-averaged low-pass filtered Kart velocity. Bottom panel: residual velocity between the Kart velocity and the best fit sinusoid.

where $\omega_K = 2\pi/T_K$ is the RippleKart oscillation frequency. The amplitude $U_{K0} = \sqrt{a^2 + b^2}$ and period T_K of the Kart oscillation were then computed. These parameters were used in determining the times of zero up-crossings of the Kart motion, which enabled the identification of individual cycles within the time series. For each range bin, the time series data were interpolated onto a common time base eliminating the relative time drift between the motor driving the Kart and the data acquisition computer clock. The phase-averaged range to the bottom was determined from the phase-averaged backscatter amplitude using equation 3.16.

The phase-averaged Kart motion determined from the MFDop data and the Pasco data are compared in Figure 3.8. It can be seen that both curves are sinusoidal with similar amplitudes. This result is consistent with *Hay et al.* (2012a), who also confirmed that the Kart motion is very nearly sinusoidal. However, the phase-averaged Pasco velocity, u_P, lags $\overline{u(r_b)}$ by 3° to 6°. This phase difference is most likely due to the lag between the data collection with the different instruments and the data transfer to the computer. Furthermore, both curves have similar periods of ~10 s. The first ~5 s represents the first half-cycle and the last ~5 s represents the second half-cycle when the Kart is moving in the opposite direction.

The theoretical Kart velocity was defined as a sine wave using:

$$u_K = \frac{d_0}{2}\omega_K \sin \omega_K t \tag{3.18}$$

where the amplitude of the sinusoid is a function of the orbital excursion d_0 and the Kart oscillation frequency ω_K. The phase-averaged velocity measured at r_b is compared to u_K in Figure 3.9. Since both curves are nearly identical (similar amplitude, period and shape), it can be concluded that the theoretical Kart velocity u_K is an appropriate definition of the Kart motion.

The phase-averaged horizontal velocities can now be obtained in the frame of reference moving with the RippleKart:

$$u_{KF}(z,t) = u_{LF}(z,t) - u_K(t) \tag{3.19}$$

where u_{LF} is the phase-averaged horizontal velocity in the laboratory (i.e. fixed) frame of reference and u_K is given by equation 3.18.

3.4.3 Ripple profile

A second estimate of the range to the bed, designated by R_B, was obtained by defining the range at which the gradient of the phase-averaged backscatter amplitude (registered by the centre transducer) exceeded a specified threshold. This bottom profile represents the sediment-water interface, whereas r_b is located within the bed. A low-pass filter (10 Hz cutoff frequency) was then implemented to remove the quantized variations associated with the discrete range bins. Using the phase-averaged bed velocity, the bottom profile was transformed from the time domain to the space domain. For each half-cycle, a best fit to the bottom profile was obtained using:

$$\eta(x) = a\sin(kx) + b\cos(kx) + \sum_{n=2}^{5}\left[a_n \sin(nkx) + b_n \cos(nkx)\right] \tag{3.20}$$

where a and b are constants, $k = 2\pi/\lambda$ and n indicates the nth harmonic. The accuracy of the fit was increased by adding a sum of harmonics to the fundamental signal. The fitted bed profile defining the sediment-water interface was then transformed back to the time domain.

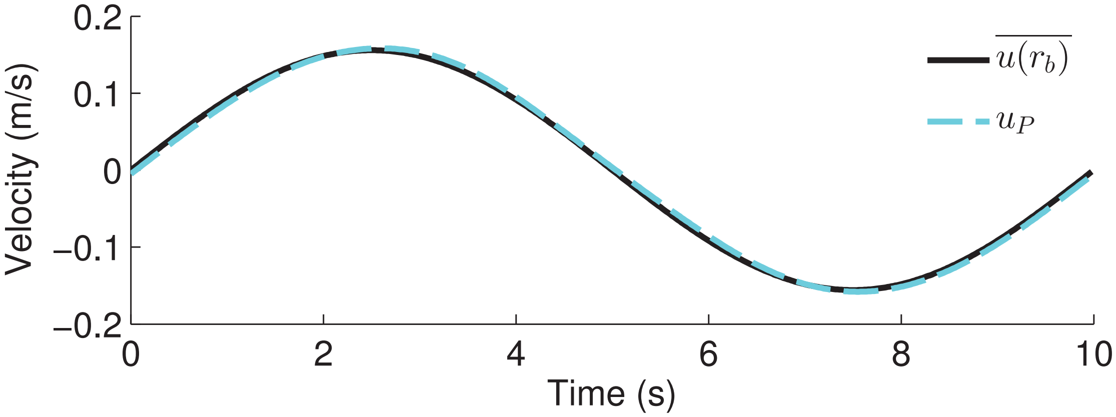

Figure 3.8: Phase-averaged bed velocity registered by the MFDop $\overline{u(r_b)}$, in black, and the Pasco u_P, in cyan.

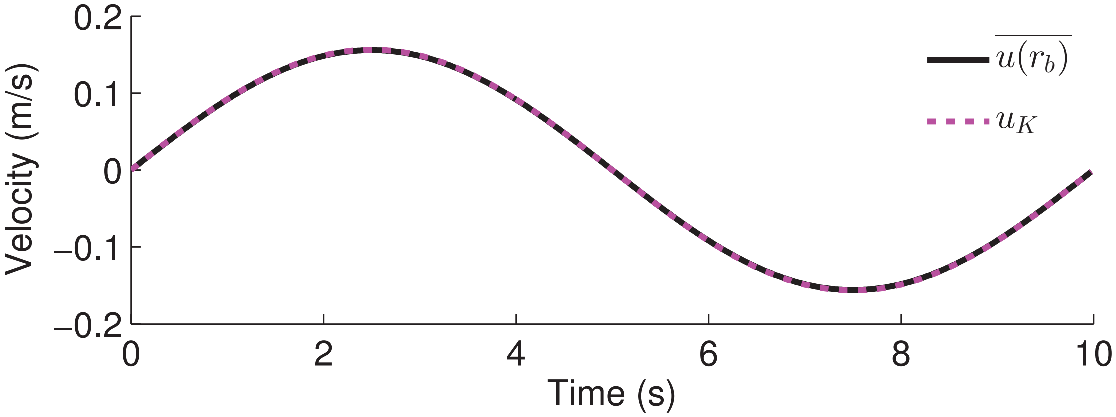

Figure 3.9: Phase-averaged bed velocity registered by the MFDop $\overline{u(r_b)}$, in black, and the theoretical Kart velocity u_K computed using equation 3.18, in magenta.

An example of the base 10 logarithm of the phase-averaged backscatter amplitude measured by outboard transducer 1 is presented in Figure 3.10. Both estimates of range to the bed are indicated: r_b in white and R_B in black. The middle panel shows the Kart velocity u_K. The bed profile during the second half-cycle is roughly the mirror image of the first. During this run, the MFDop head was positioned directly over a ripple crest at maximum Kart translation speed, as can be seen in Figure 3.10: the time at which the ripple crest passes beneath the MFDop head is 2.5 s which is the time of maximum Kart velocity. The bottom panel shows the magnitude of the ensemble-averaged complex correlation between consecutive pulses. Overall, the signal correlations are quite high. As discussed in *Hay et al.* (2012a), patches of lower correlation (and higher error in the amplitude and velocity estimates) are most likely due to turbulence near the bed, and to low scatterer concentrations far from the bed.

3.4.4 Bottom contamination

Over a flat bed, the bottom return from an outboard transducer arrives earlier by 6 mm than from the centre transducer (see Appendix D). In other words, the path of least time from the centre transducer to an outboard transducer is shorter by 6 mm than the path from the centre transducer and back. This result is consistent with measurements made in *Hay et al.* (2012a), where they estimated that the bottom return arrived earlier by 5 mm ± 1 mm. As a result, horizontal velocity measurements can only be accurately resolved beyond 6 mm from the bed due to the MFDop geometry.

Using the bed profiles R_B obtained from different transducers, the bottom contamination zone for a rippled bed can be estimated. In Figure 3.11, the bed profiles obtained using the backscatter amplitude registered by outboard transducers 1 and 2 are compared to the bed profile determined using the data from the centre transducer. The absolute difference between both outboard transducers and the centre transducer are given in the bottom panel. Averaging the mean difference of various runs together, the bottom contamination layer is estimated to start at 4 mm ± 2 mm above bed level.

3.4.5 Reaction flow

The Vectrino velocity measurements were first despiked by identifying data points that had correlations lower than 70% and replacing these points by the average of its nearest neighbours. Next, the data were low-pass filtered (0.2 Hz cut-off frequency) and then

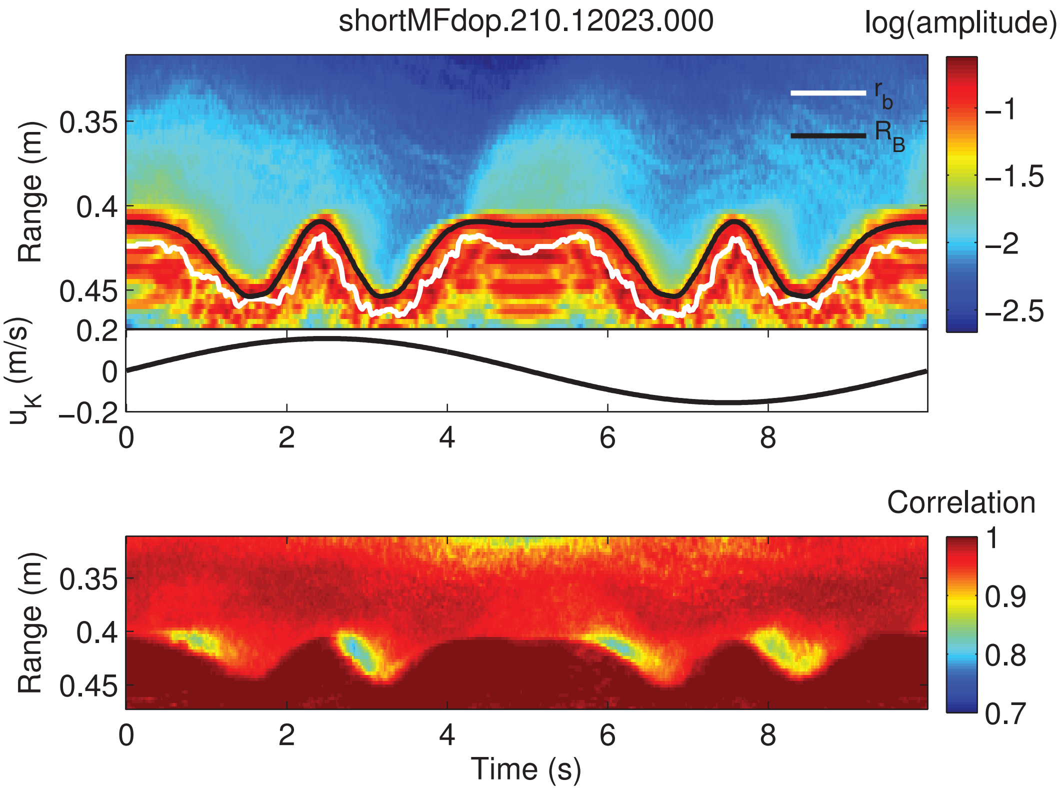

Figure 3.10: Top panel: Base 10 logarithm of the phase-averaged backscatter amplitude measured by outboard transducer 1 in Volts as a function of time for a RippleKart run. Two estimates of range to the bed are indicated: r_b in white and R_B in black. Middle panel: Kart velocity u_K. Bottom panel: phase-averaged correlation obtained using outboard transducer 1.

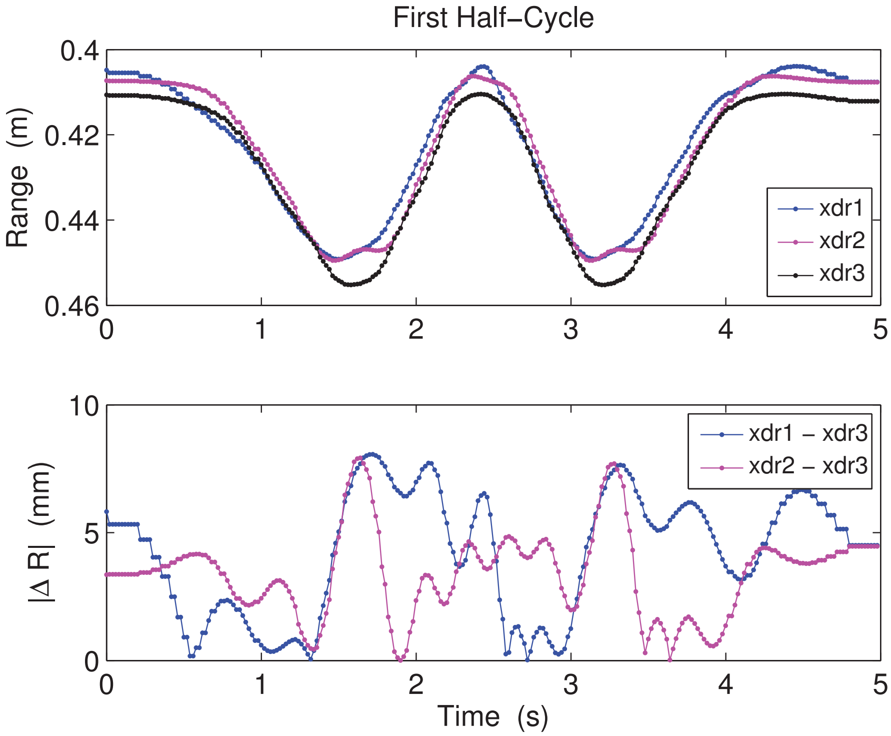

Figure 3.11: Top panel: R_B determined from outboard transducers 1 and 2, as well as from the centre transducer (transducer 3) for an example RippleKart run. Bottom panel: absolute range difference between the outboard and centre transducer bed profiles.

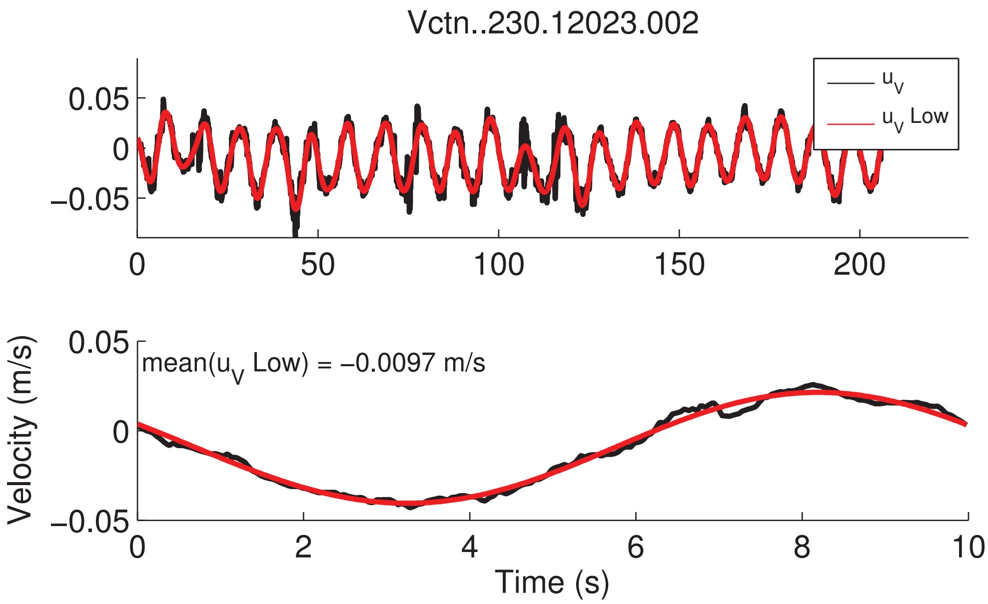

Figure 3.12: Top panel: velocity time series measured with the Vectrino. The raw data are in black and the low-pass filtered data are in red. Bottom panel: phase-averages of the data in the top panel.

interpolated onto the MFDop timebase. The time delay calculated in section 3.3.1 was taken into account. An example Vectrino time series is shown in the top panel of Figure 3.12. The phase-averaged reaction flow induced by the displacement of water by the sediment-laden tray was calculated from the Vectrino data (bottom panel of Figure 3.12). All cycles were included in the Vectrino phase-averaging. It can be seen that the reaction flow is nearly sinusoidal with a 10 s period. However, the phase-averaged velocity data have a small (1 cm/s) non-zero mean, which could indicate asymmetry in the tank response at the Vectrino location.

3.4.6 Relative flow

The reaction flow contributes to the forcing at the bed. The relative velocity u_R is given by

$$u_R = u_K - u_V \tag{3.21}$$

where $u_K = u_{K0} \sin \omega_K t$ is the Kart velocity, $\omega_K = 2\pi/T$ and u_V is the phase-averaged reaction flow registered by the Vectrino. The latter can be expressed as a sine wave

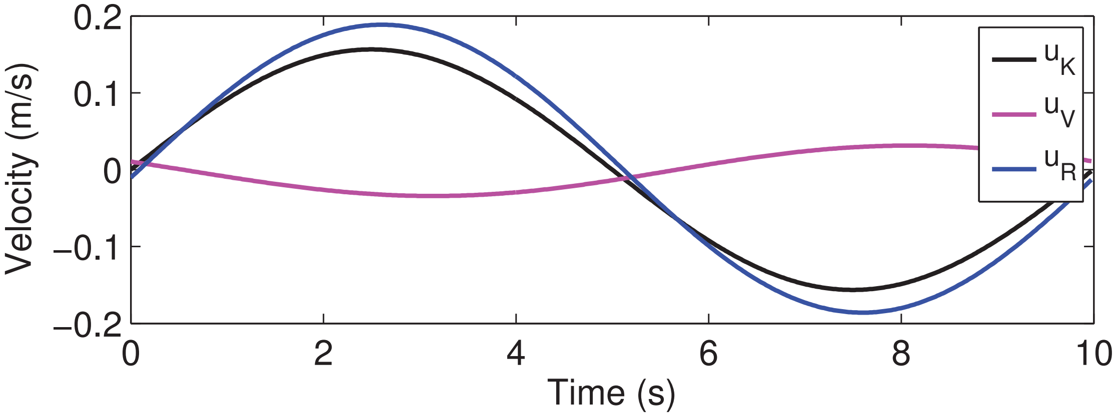

Figure 3.13: Kart velocity u_K, phase-averaged reaction flow registered by the Vectrino u_V and phase-averaged relative velocity u_R as a function of time for a RippleKart run.

$u_{V0}\sin(\omega_K t + \phi_V)$ with phase ϕ_V. Using trigonometric identities,

$$u_R = [u_{K0} - u_{V0}\phi_V]\sin\omega_K t - [u_{V0}\sin\phi_V]\cos\omega_K t \tag{3.22}$$

Simplifying,

$$u_R = u_{R0}\sin(\omega_K t + \phi_R) \tag{3.23}$$

where the relative velocity amplitude u_{R0} and ϕ_R are given by

$$u_{R0} = \sqrt{{u_{K0}}^2 - 2u_{K0}u_{V0}\cos\phi_V + {u_{V0}}^2} \tag{3.24}$$

$$\tan\phi_R = \frac{u_{V0}\sin\phi_V}{u_{K0} - u_{V0}\cos\phi_V} \tag{3.25}$$

The maximum of u_R will occur when $\omega_K t + \phi_R = \pi/2$. Therefore,

$$\phi_R = \pi/2 - \omega_K t_{max} \tag{3.26}$$

From equation 3.26, the maximum relative velocity u_R was estimated to occur 3.6° to 5.0° after the maximum Kart velocity u_K. The phase-averaged time series of relative velocity u_R, the Kart velocity u_K and the reaction flow u_V are compared in Figure 3.13. All three signals are nearly sinusoidal with 10 s periods. The amplitude of the reaction flow is much smaller than the Kart velocity amplitude. Furthermore, the reaction flow is nearly out of phase with the Kart velocity: $\phi_V = 201°$ for this run.

3.4.7 Transformation to the space domain

Let

$$\Delta x = u_K \Delta t \tag{3.27}$$

where x is the horizontal distance in the direction of the RippleKart oscillation. For each run, the data were transformed from the time domain to the space domain using the Kart velocity u_K and then interpolated onto fixed x coordinates:

$$u_{KF}(z,t) \Rightarrow u_{KF}(z,x) \tag{3.28}$$

This transformation to the space domain has two purposes. First, it allows the direct calculation of the second term of vorticity $\partial w/\partial x$ (equation 2.54). Second, this transformation is used to construct an instantaneous picture of the flow using the MFDop measurements, as discussed in the following section.

3.4.8 Flow field at different phases

The velocity profiles from different RippleKart runs were combined to determine the flow field over one full ripple profile at different phases of the forcing cycle. For each run, data segments of equal length in the space domain are pieced together using a linearly weighted mean in the overlap areas. A sketch of this linear weighting in the overlap area for two cases is presented in Figure 3.14. Data segments in the space domain are represented by rectangular boxes and the overlap area is indicated by dotted vertical lines. For two overlap zones (Figure 3.14a), the edge of each data segment is given less weight than the interior. A similar procedure is used for three overlap zones (Figure 3.14b), except for more importance given to the middle segment.

The length of each segment was determined by selecting data contained within 2% of the maximum of u_R. At 90° phase, this data segment represents a window spanning $\pm 12°$ from the phase of interest with a 7° overlap. At this phase, the unblended region represents $\pm 5°$. The lengths of the data segments in phase space at different phases of interest are listed in Table 3.3. An example of the piecing procedure is shown in Figure 3.15. Portions of the velocity distribution that are pieced together at 90°± 12° are shown in colour. The length in x of each portion can differ a little due to differences between runs of the maximum relative flow. The resulting velocity field thus represents an instantaneous picture of the phase-averaged flow over a ripple at a particular phase of the forcing cycle.

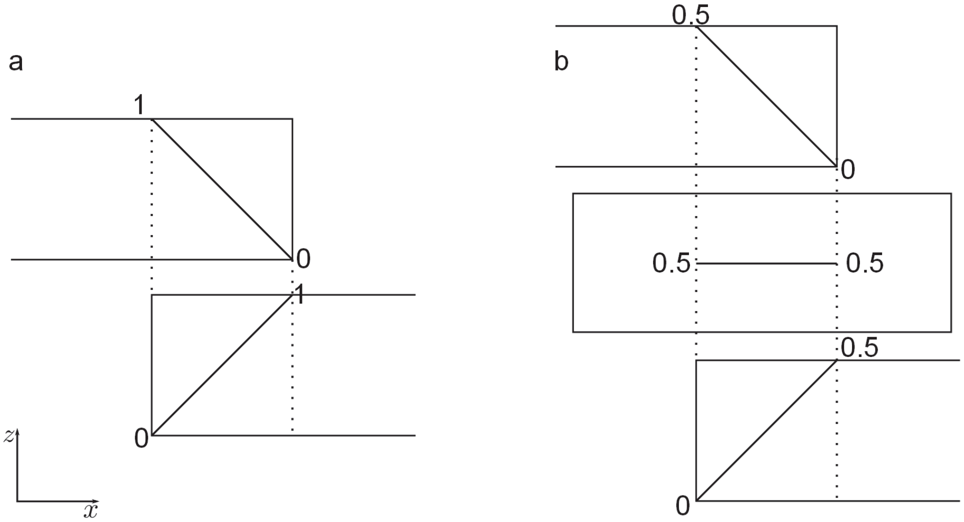

Figure 3.14: A sketch indicating the linear weighting used in the overlap for 2 cases: 2 overlap zones (a) and 3 overlap zones (b). The rectangular boxes represent data segments in the space domain and the dotted vertical lines indicate the overlap area.

Table 3.3: Length of data segments in phase space for d_0 = 49.8 cm

Phase (°)	± (°)	average overlap (°)
90	12	7
105	12	7
120	14	8
135	20	9

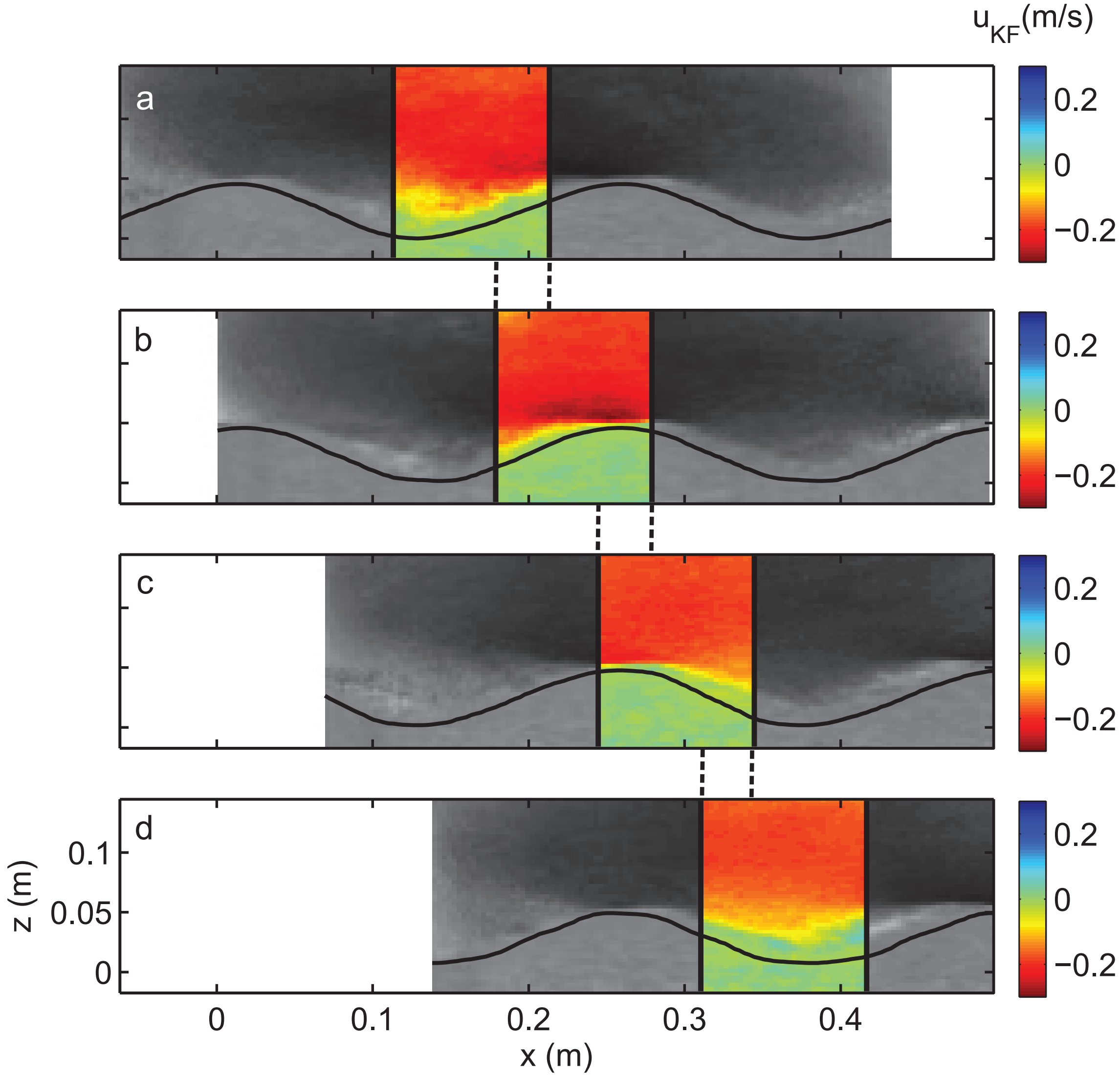

Figure 3.15: Phase-averaged horizontal flow in the Kart frame for different RippleKart runs. The segments to be pieced together at 90°± 12° phase of the forcing cycle are shown in colour. In a), the MFDop was positioned over the zero up-crossing of the ripple profile; in b) over the crest; in c) over the down zero-crossing, and in d) over the trough. Dashed lines indicate the overlap areas.

The piecing procedure is compromised if the mean values of the overlap pieces are widely different, indicating that the chosen length of the data segment in phase space is too large. Thus, to check this piecing procedure, vertical profiles of the linearly-weighted mean for each overlap section at 90° are compared in Figure 3.16. In this case, only two data segments overlapped and the linearly-weighted mean was implemented as sketched in Figure 3.14a. The solid lines indicate the linearly-weighted mean within the overlapping section for each data segment and the dashed lines represent one standard deviation from each mean. The location of the centre of the overlapping pieces is indicated in grey in the inset of the horizontal flow field at 90°. For each location, both vertical profiles are similar indicating that the piecing procedure is doing well. However, over the crest, there is a larger difference between the two profiles. Due to higher flow speeds, the velocity field is changing more rapidly. As a result, the mean vertical profile of both overlapping portions will differ since there is (at most) a 24° difference.

3.4.9 Vorticity, acceleration and the non-linear terms

Vorticity was calculated in the space domain using equation 2.54, where each term was estimated by using a 3-point linear fit with the shear given by the slope. The local acceleration ($\partial u/\partial t$) as well as the non-linear terms ($u\partial u/\partial x$ and $w\partial u/\partial z$) were estimated in a similar way. The local acceleration was calculated before the piecing procedure in the time domain. The non-linear terms were determined after the piecing procedure in the space domain. All three terms were smoothed by averaging together every point and its nearest neighbours. The bottom was not included in the averaging.

3.4.10 Spatial-averaging

Presented in section 2.4.5, the roughness geometry function $\Psi(z)$ was determined to be

$$\Psi(z) = \frac{\lambda - b(z)}{\lambda} \tag{3.29}$$

where $b(z)$ is the ripple width at elevation z. The ripple profile and the roughness geometry function determined from the MFDop data are presented in Figure 3.17. The $\Psi(z)$ function determined from the experimental data can be compared to a theoretical ripple profile given by

$$\eta(x) = \eta_0 \left[\cos\left(\frac{2\pi}{\lambda}x\right) + 1\right] \tag{3.30}$$

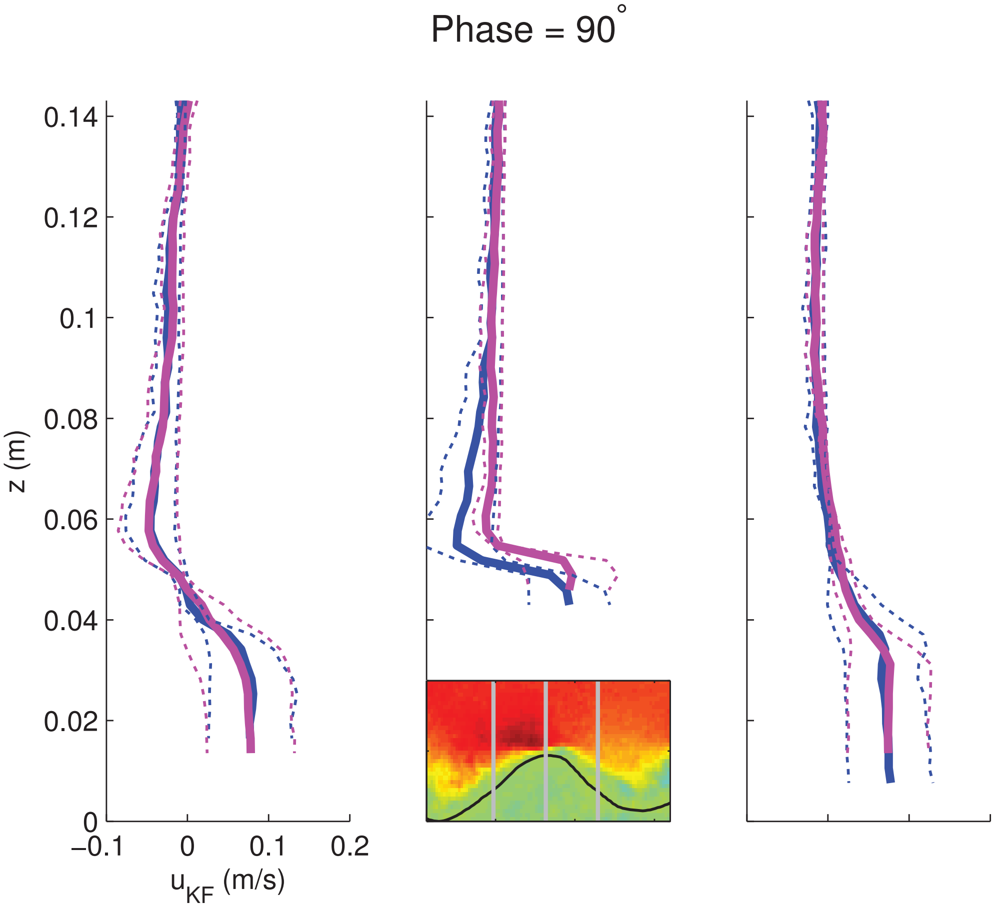

Figure 3.16: Linearly-weighted mean vertical profiles of u_{KF} within the overlapping area at 90°± 12° for both data segments (solid blue and magenta lines). The dashed lines represent one standard deviation away from the mean. The location of the centre of the overlapping pieces is indicated by vertical grey lines in the inset of the horizontal flow u_{KF} at 90°.

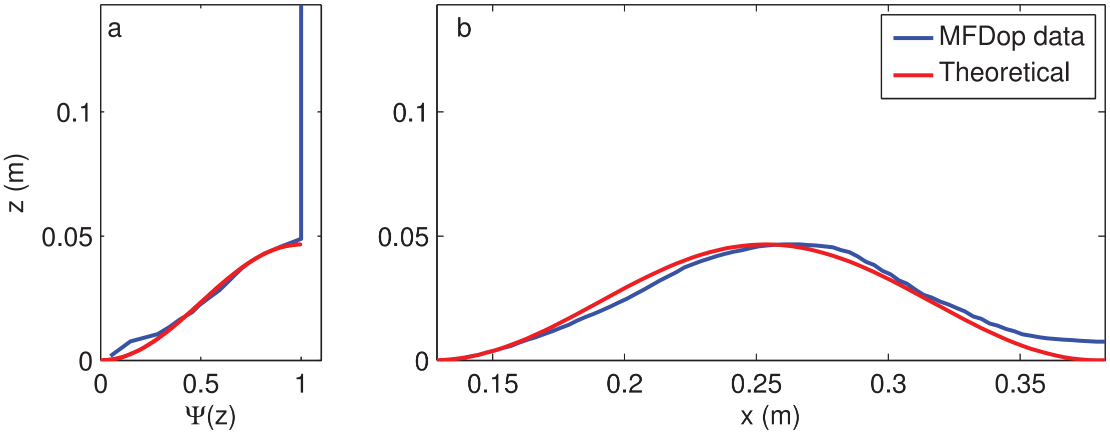

Figure 3.17: Roughness geometry function $\Psi(z)$ (panel a) and ripple profile (panel b). The profiles from the MFDop data (blue) and from a theoretical ripple (red) are compared.

where η_0 is the ripple amplitude. The corresponding roughness geometry function can be determined from equation 3.29 using a ripple width of $2x$ and by isolating x in equation 3.30. The roughness geometry function determined analytically is shown in red in Figure 3.17a and is compared to the parameter determined from the experimental bed profile in blue. In both cases, $\Psi(z) = 0$ in the troughs, and $\Psi(z) = 1$ over the crest. However, since the troughs of the experimental bed profile are at slightly different heights, the analytical and experimental roughness geometry functions differ close to the bed.

The intrinsic spatial average $\langle\theta\rangle$ of a flow variable θ was determined by taking the average of the flow at each range bin over a full ripple profile. The area occupied by the ripple was excluded in this average. The spatial fluctuations $\tilde{u}$ and $\tilde{w}$ of the phase-averaged flow variables were determined by calculating the difference between the phase-averaged flow and the double-averaged flow. The superficial spatial average $\langle\theta\rangle_s$ of a flow variable was obtained by calculating the product between its intrinsic spatial average and the roughness geometry function, i.e. $\langle\theta\rangle_s = \Psi(z)\langle\theta\rangle$.

3.4.11 Stress and turbulence

The Reynolds stress was determined using equation 3.11. The fluctuations of the observed velocities (V's) were obtained by removing the phase-averaged flow from the unfiltered time series for each cycle. The square of the resulting time series was then phase-averaged in order to obtain the second moments of the turbulent velocity fluctuations ($\overline{V'^2}$). Turbulent kinetic energy (TKE) was estimated using equation 2.66 and turbulence production was determined using equation 2.67. Similarly to the flow, the Reynolds stress, TKE and turbulence production were pieced together in order to obtain an instantaneous picture of stress and energy at different phases of the forcing cycle.

From equation 2.59, the law-of-the-wall takes the following form:

$$u(z,t) = \frac{u_*(t)}{\kappa} \ln(z'/z_0) + u_K(t) \tag{3.31}$$

where u_K is the velocity of the boundary, u_* is the friction velocity, z_0 is the roughness height, and $z' = z + \Delta z$, Δz being the displacement height. The no-slip condition is satisfied for a moving boundary since $u = u_K$ at $z' = z_0$ (*Monin and Yaglom*, 1971). The law-of-the-wall stress estimates were based on fits of vertical profiles of the time-averaged (0.1 s interval) horizontal velocity at different points along the ripple profile. Using the mean bed level as Δz, the free parameters in the fit were the friction velocity u_* and the roughness height z_0. The fit was only executed on the part of the vertical profile that seemed to exhibit the characteristic logarithmic behaviour near the bed, which corresponded to 10 data points over the zero-crossings and 12 data points over the troughs. Furthermore, due to the bottom contamination of the return signal, the closest range bins to the bed (∼3 bins) were discarded.

CHAPTER 4

RESULTS

4.1 Flow field

4.1.1 Horizontal flow

The phase-averaged horizontal velocity in the frame of reference moving with the Kart at 90° phase of the forcing cycle is compared to the solutions for potential flow given by *Davies* (1983) and *Longuet-Higgins* (1981) in Figure 4.1. The z axis indicates the height above the first trough. Ripple amplitude and wavelength, as well as the free-stream velocity were determined from the phase-averaged results and used in calculating the potential flow solutions (equations 2.31 and 2.45). It is important to note that the colour map has been reversed in all three plots in order to indicate certain features of the flow more clearly. Negative u velocities indicate fluid moving in the negative x direction. The black line in all three panels represents the sediment-water interface (R_B). Due to the constriction of the flow from the trough to the crest, the flow accelerates as it rises towards the crest (right side of ripple) and then decelerates as it descends into the trough (left side of ripple), resulting in an intensification of the horizontal flow over the ripple crest and lower near-bed velocities in the troughs. All three panels show these two features: higher velocity over the ripple crest and lower velocity in the troughs. Compared to both potential flow solutions, a spatial shift of the intensification of the flow measured by the MFDop is evident. This shift is most likely due to the lack of bottom friction in the models and due to the experimental ripples being not quite symmetrical.

Vertical profiles of horizontal velocity above the crest and troughs are presented in Figure 4.2. The solid lines are based on the phase-averaged horizontal velocity in the

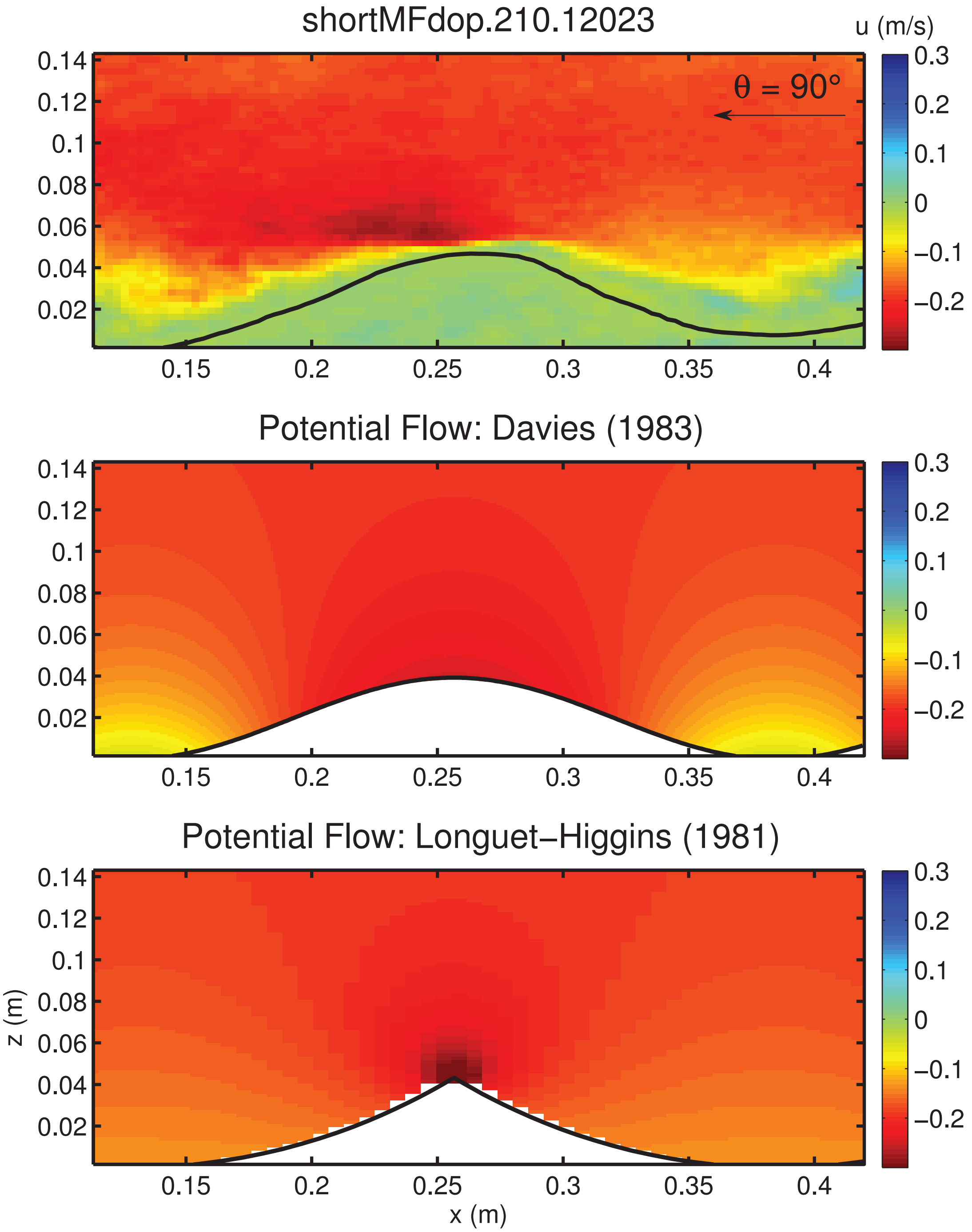

Figure 4.1: Horizontal flow during the first half cycle. Top panel: phase-averaged horizontal velocity at 90°. Middle panel: horizontal potential flow over a ripple based on *Davies* (1983) solution. Bottom panel: horizontal potential flow over a steep ripple based on *Longuet-Higgins* (1981) solution.

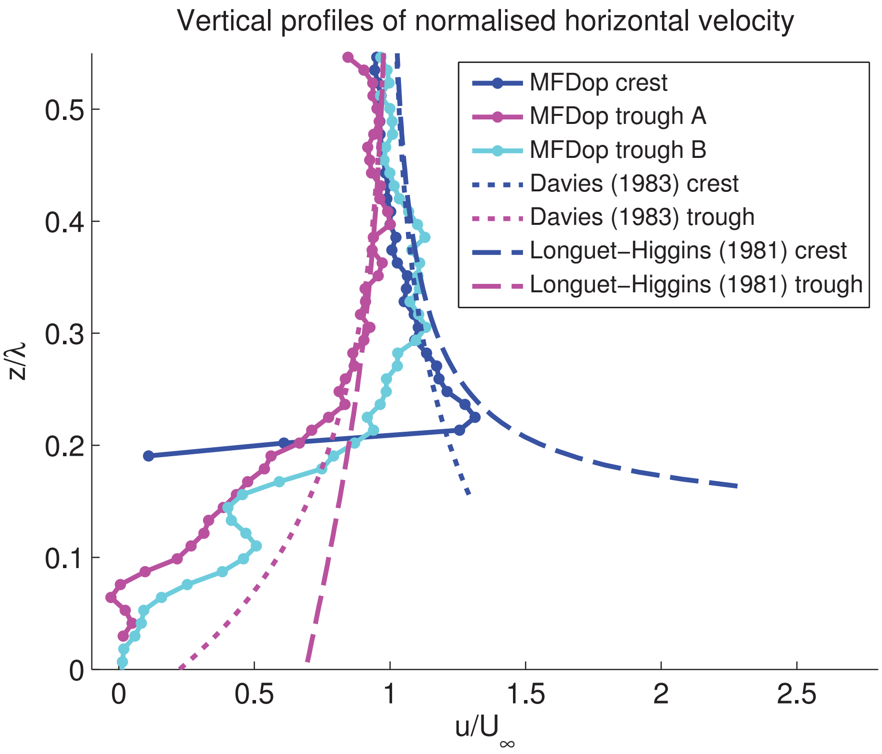

Figure 4.2: Vertical profiles of normalised horizontal velocity above the crest and trough during the first half-cycle at 90° of the forcing cycle.

Kart frame at 90°. The dotted and dashed lines are based on the solutions obtained by *Davies* (1983) and *Longuet-Higgins* (1981), respectively. Very close to the bed, the MFDop profiles decrease toward zero, unlike the theoretical profiles. This difference is due to the absence of bottom friction in the models. Over the crest, the theoretical and observed vertical profiles of horizontal velocity increase towards the bed. This feature in the profile corresponds to the intensification of the flow over the ripple crest discussed earlier. Due to the sharper peaks in the model presented by *Longuet-Higgins* (1981), the intensification of the potential flow over a ripple crest is more pronounced. The ripples that were created experimentally have sharper peaks than a sine wave, yet more rounded peaks than the bottom profile given by the model presented by *Longuet-Higgins* (1981). As a result, the observed intensification of the flow over the crest is stronger than that given by *Davies* (1983) and weaker than the flow in the model presented by *Longuet-Higgins* (1981).

Vertical profiles of horizontal flow in the frame of reference moving with the Kart at different phases of the forcing cycle are presented in Figure 4.3. These profiles are

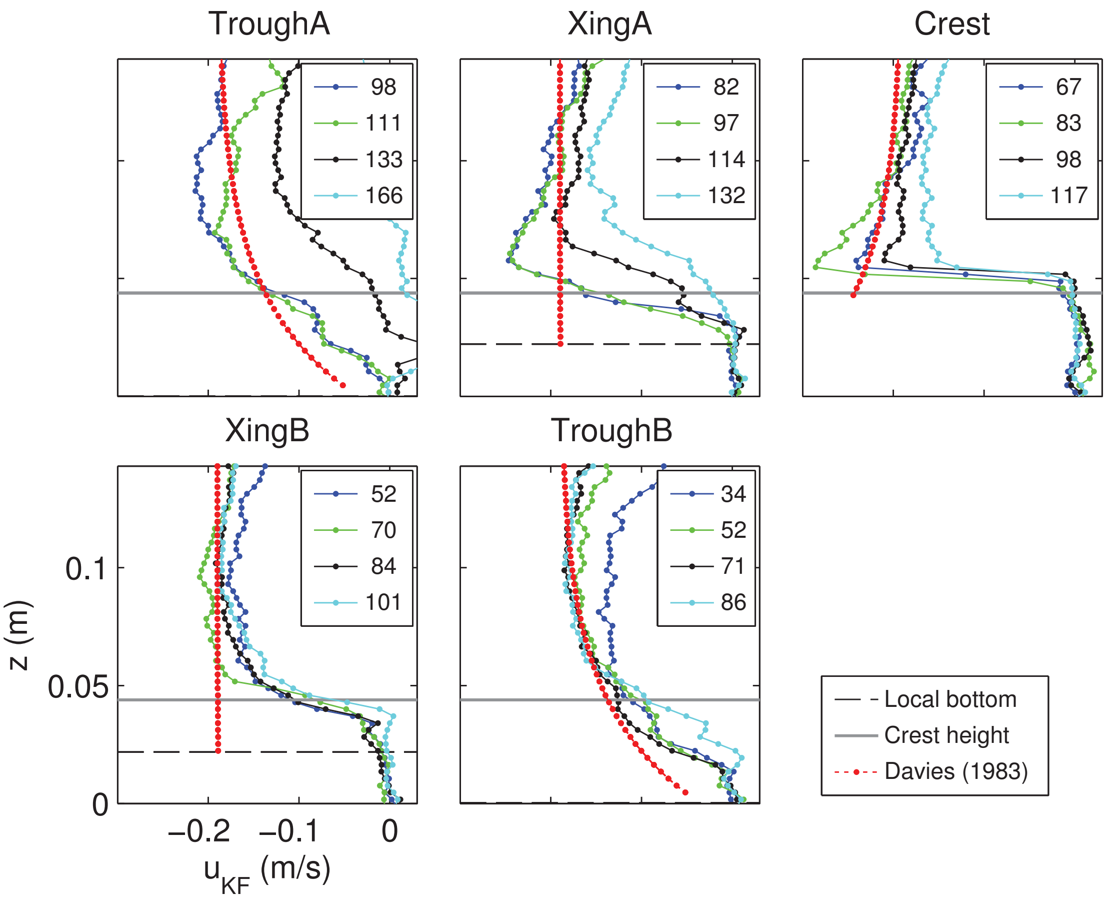

Figure 4.3: Vertical profiles of horizontal flow in the frame of the reference moving with the Kart at different phases of the forcing cycle measured by the MFDop. The red dots indicate the flow at the same positions calculated from *Davies* (1983) at 90° phase.

compared to potential flow profiles at 90° calculated from *Davies* (1983) at the same locations along the ripple profile. It can be seen that the intensification of the flow over the crest varies as a function of phase, peaking around 90°. Over the crest and troughs, the shape of the vertical profiles of the flow above the zone influenced by bottom friction is comparable to the model prediction. However, over the zero-crossings, the model indicates that the flow is constant with depth. This behaviour is quite different from the MFDop data which indicate a fluid layer with high vertical shear extending upward from the bed.

Vertical profiles of horizontal flow at different phases of the forcing cycle as measured with the MFDop (black) and the Vectrino (red) are presented in Figure 4.4. The MFDop measurements were obtained by averaging over five repeat runs and the grey lines indicate the error based on one standard deviation from the mean. The relatively small error of

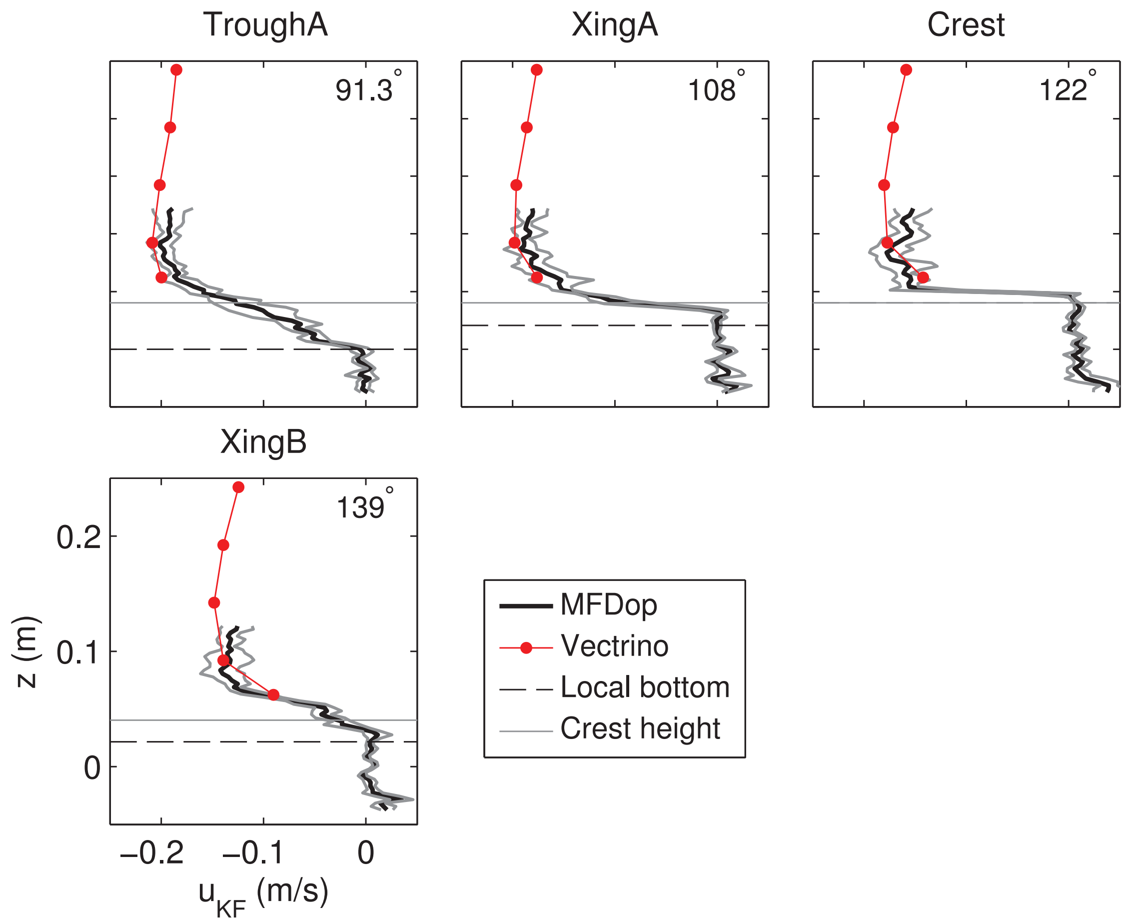

Figure 4.4: Vertical profiles of horizontal flow in the Kart frame at different phases of the forcing cycle measured by the MFDop (black and grey) and the Vectrino (red). The horizontal dashed line and the horizontal grey line represent the height above TroughA of the local bottom and the crest height, respectively.

the MFDop profiles confirms the repeatability of the RippleKart runs. Furthermore, these Vectrino measurements also support the validity of the MFDop results.

4.1.2 Vertical flow

In Figure 4.5, the phase-averaged vertical velocity at 90° phase is compared to the vertical flow obtained from *Davies* (1983) and *Longuet-Higgins* (1981) solutions. Consistent with Figure 4.1, the colour map has been reversed. Upward flow is indicated by blue (positive velocity) and downward flow is represented by red (negative velocity). As the horizontal flow meets the ripple face, it must flow upwards and over the ripple crest coming back down on the other side. This flow pattern is clearly shown in all three panels by patches of upward velocity to the right of the ripple crest and downward velocity to the left. Upward flow in both models is stronger than the measured upward flow. Differences between the observed and predicted flow patterns are due to bottom friction and to different ripple shapes.

4.1.3 Cross-tank flow

The phase-averaged cross-tank horizontal velocity (parallel to the ripple crests) at 90° phase is shown in Figure 4.6. Positive velocities are into the page. The cross-tank flow has little structure and is small compared to the along-tank and vertical flows. The cross-tank flow is non-zero, likely because the ripples were not quite two-dimensional, and the crests not perfectly aligned with the y-axis.

4.1.4 Flow field evolution

The evolution of the flow field over different phases is presented in Figure 4.7. Streamlines are indicated in blue. At 90° phase, or at the time of maximum forcing, the flow is clearly separating immediately downstream of the crest. A separation bubble is thus beginning to form on the lee side of the ripple crest. As the free-stream velocity decelerates (phases greater than 90°), the separation bubble increases in size and begins to detach from the ripple face.

4.1.5 The influence of the non-linear terms

As discussed in section 2.2.3, the horizontal pressure gradient in potential flow is dependent on height above the bed and the relative contribution of the non-linear terms are non-negligible. It was concluded that the boundary layer approximation is unlikely to hold over orbital-scale ripples. This question can now be investigated further using the MFDop data.

The local acceleration $\partial u/\partial t$ and the non-linear terms determined from experimental results at 90° phase are given in Figure 4.8. As stated in section 3.4.9, the local acceleration was calculated in the time domain for each run before the piecing procedure. The non-linear terms are obtained by multiplying the horizontal and vertical gradients by the horizontal or vertical flow. Since u and w are nearly zero within the bed, the non-linear terms are expected to contain less bottom noise than the acceleration term (see Figure 4.8). Within the bottom boundary layer, the acceleration term is comparable in magnitude to the non-linear terms. Interesting features can be seen in the $w\partial u/\partial z$ component due to the

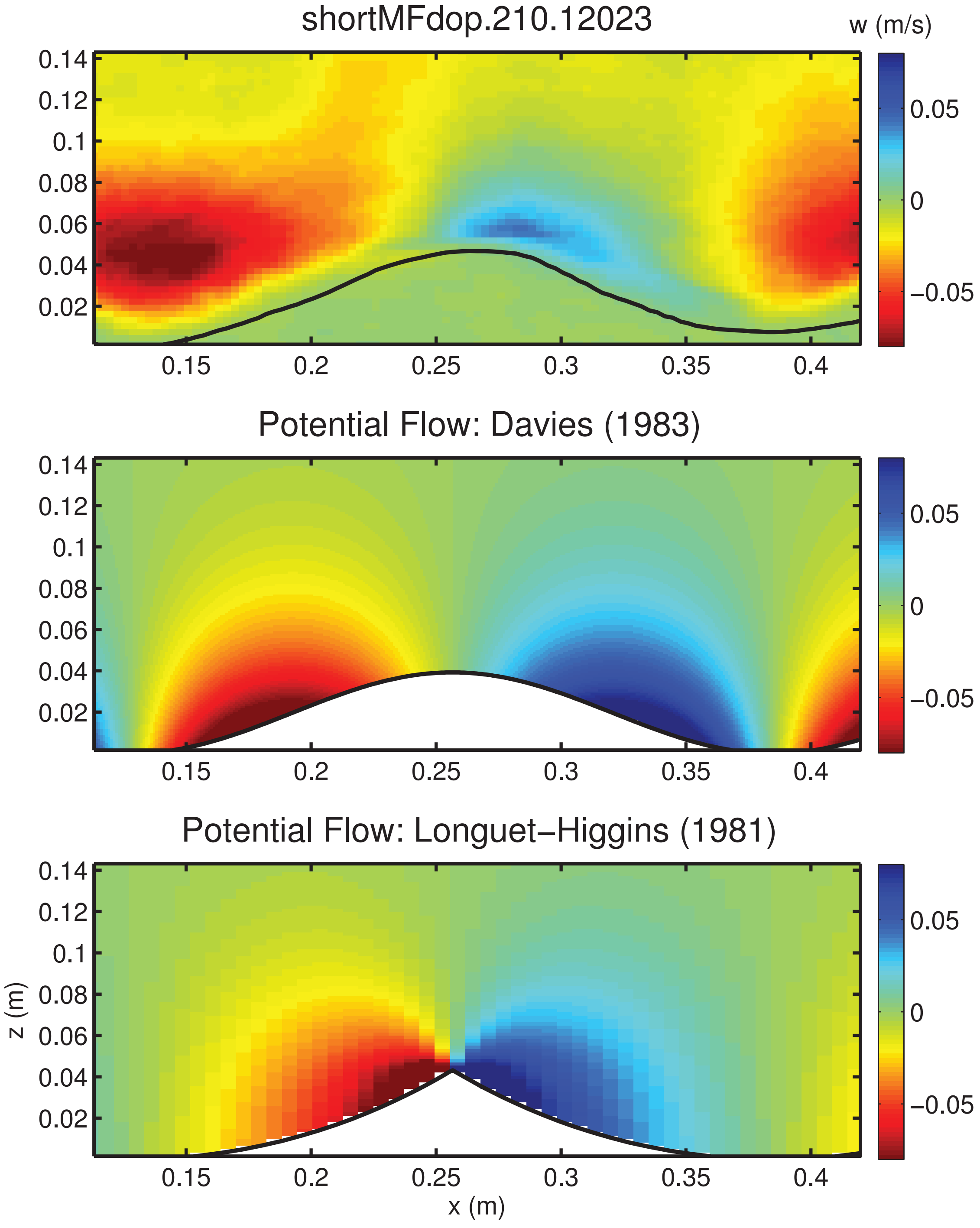
shortMFdop.210.12023

Potential Flow: Davies (1983)

Potential Flow: Longuet–Higgins (1981)

Figure 4.5: Vertical flow during the first half cycle. Top panel: phase-averaged vertical velocity at 90°. Middle panel: vertical potential flow over smooth-crested ripples based on the solution presented by *Davies* (1983). Bottom panel: vertical potential flow over steep-crested ripples based on the solution given by *Longuet-Higgins* (1981). The sediment-water interface is indicated in black.

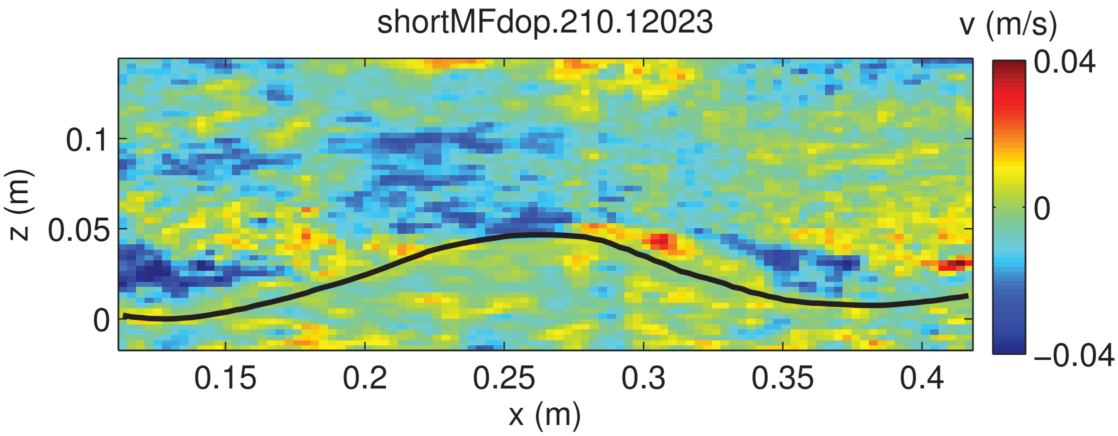

Figure 4.6: Phase-averaged cross-tank horizontal velocity at 90° phase. The sediment-water interface is indicated by the black line.

presence of large vertical shear. The intensification of flow over the crest and the existence of the lee vortex both contribute to areas of large vertical shear. The acceleration term at 60° as well as the non-linear components are presented in Figure 4.9. As in Figure 4.8, all terms are comparable in magnitude.

The boundary layer approximation assumes that the magnitudes of the variations in the stream-wise direction are much smaller than the magnitudes of the variations normal to the boundary. The non-linear terms determined from the MFDop data have been shown to be non-negligible, which confirms that the boundary layer approximation does not hold. As a result, the stress over these ripples cannot be accurately resolved using the vertically integrated defect acceleration.

4.1.6 Rotational flow

The rotational part of the flow can be estimated by subtracting the potential flow solution (*Davies*, 1983) from the flow measurements obtained using the MFDop. A layer of positive horizontal rotational flow u_{rot} is clearly visible in the top panel of Figure 4.10. Diffusion of negative u_{rot} away from the ripple crest is also evident. In the bottom panel, patches of negative and positive vertical rotational flow w_{rot} are well defined on the ripple flanks. These features of large rotational flow represent areas in the flow field that are affected by shear stresses within the flow and at the bed.

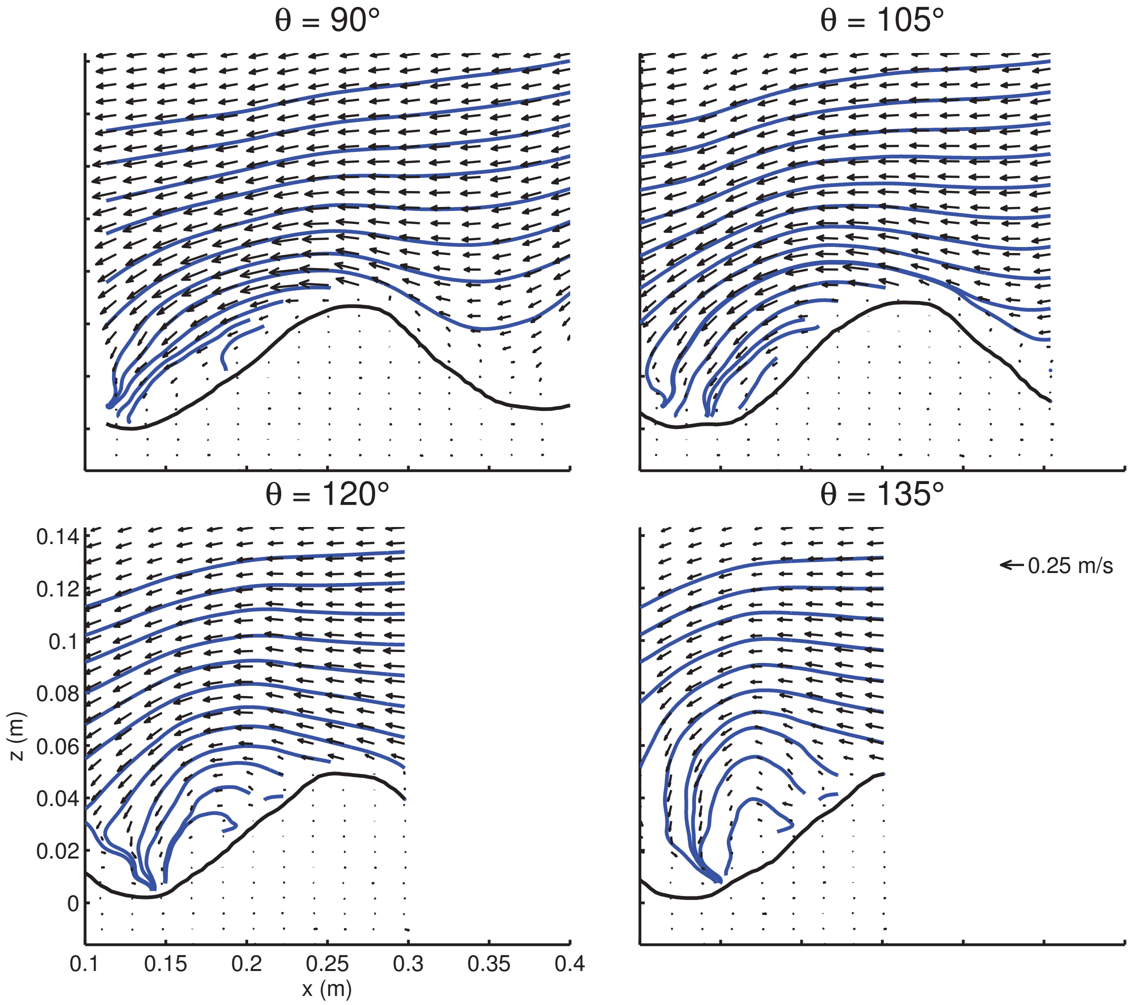

Figure 4.7: Evolution of the flow field (arrows) and streamlines (blue). The sediment-water interface is indicated in black.

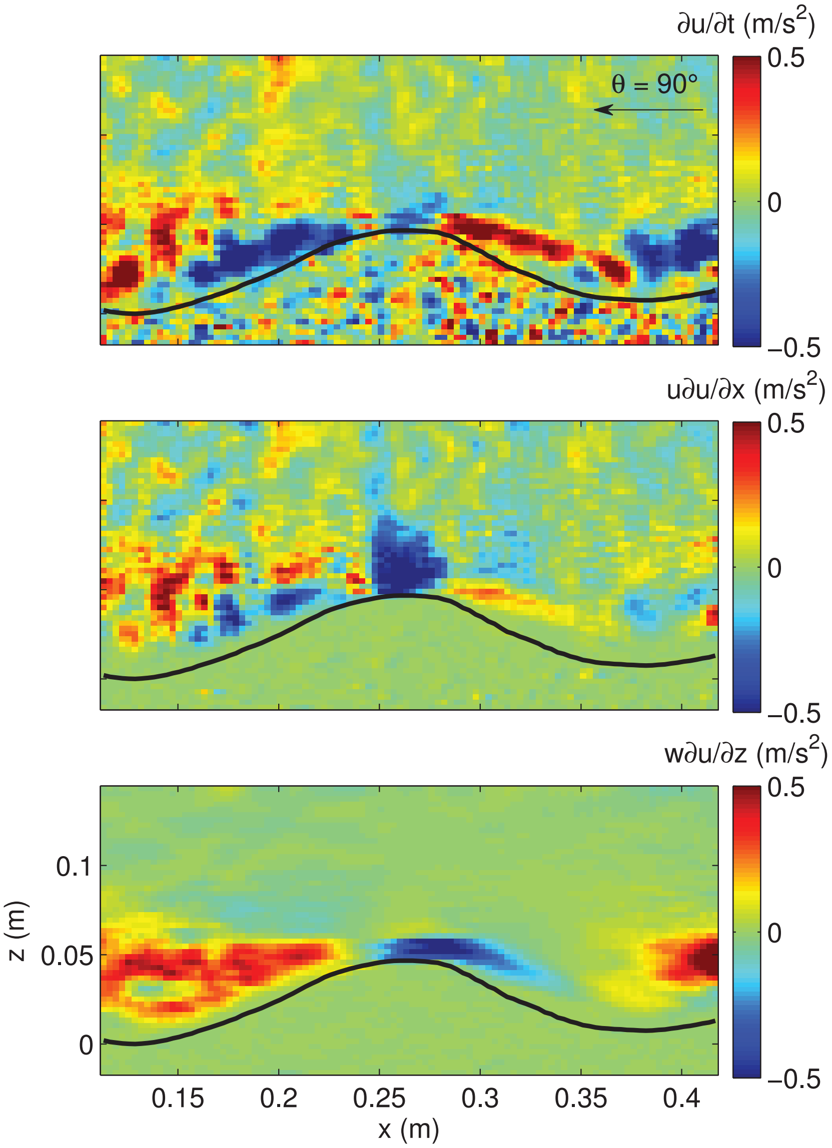

Figure 4.8: The acceleration term $\partial u/\partial t$ and the non-linear terms ($u\partial u/\partial x$ and $w\partial u/\partial z$) at 90° phase of the forcing cycle.

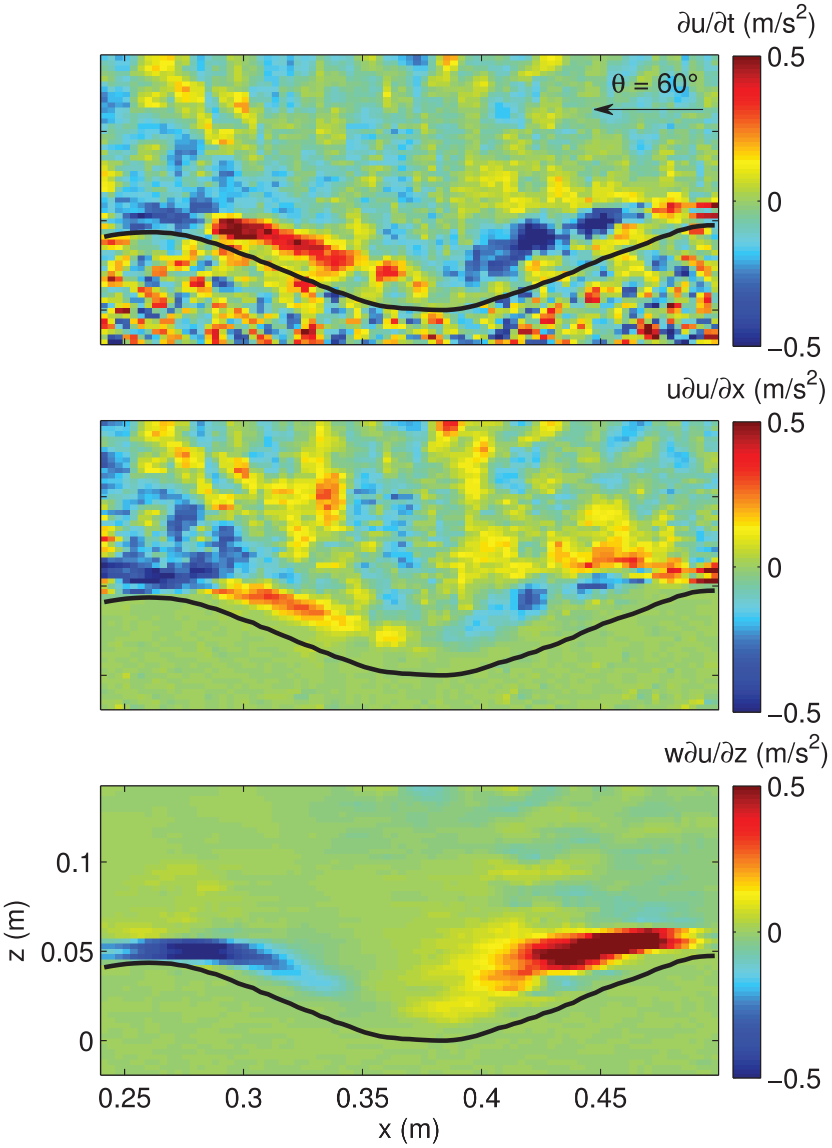

Figure 4.9: The acceleration term $\partial u/\partial t$ and the non-linear terms ($u\partial u/\partial x$ and $w\partial u/\partial z$) at 60° phase of the forcing cycle.

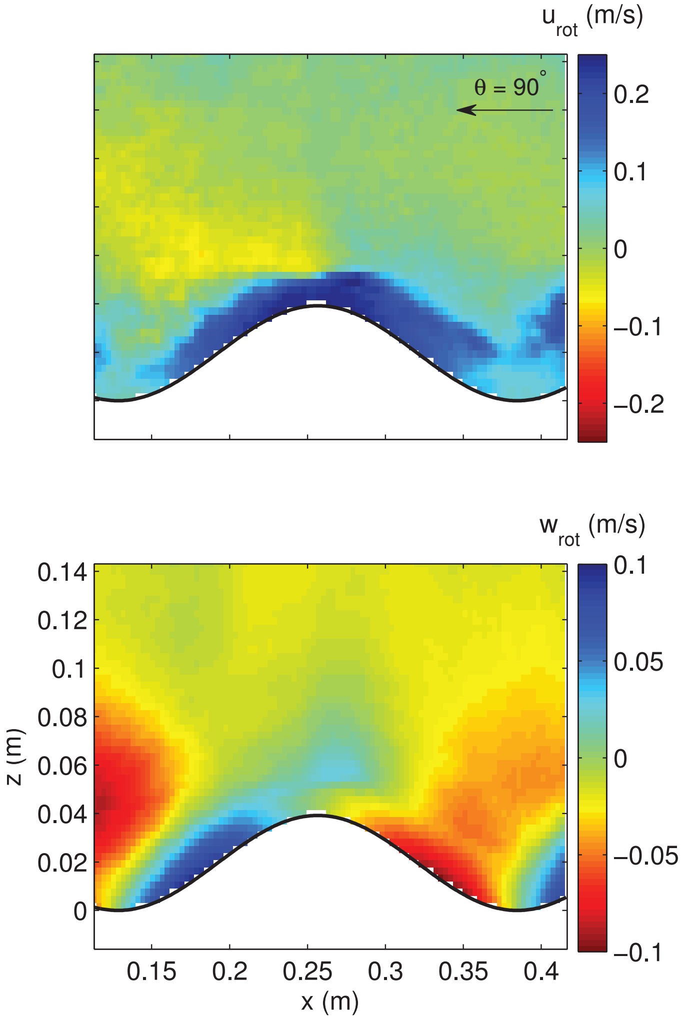

Figure 4.10: Rotational part of the horizontal flow (top panel) and vertical flow (bottom panel) at 90°. The sediment-water interface is indicated in black.

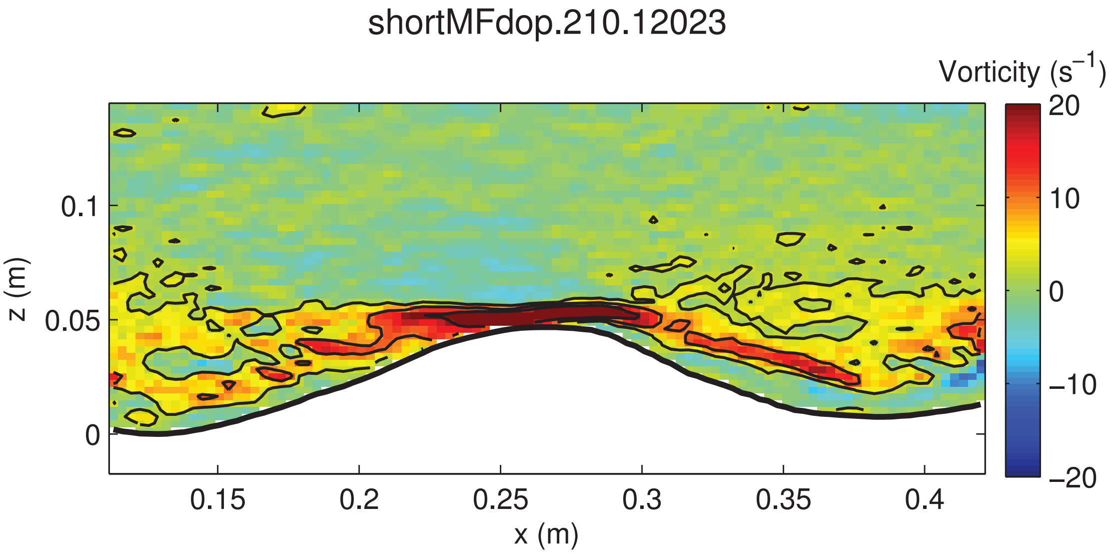

Figure 4.11: Vorticity field over a ripple at 90° phase where certain contour lines are given in black. The sediment-water interface is indicated by a thick black line.

4.2 Vorticity field

The vorticity field over a ripple at 90° phase is presented in Figure 4.11. The main contribution to vorticity is due to the vertical shear term $\partial u/\partial z$ (not shown). Consequently, there is a high vorticity layer close to the bed. Since there is an expected increase of vertical shear at the edges of the lee vortex, higher vorticity surrounds a patch of near zero or weakly negative vorticity downstream from the ripple crest (at lower x values). Furthermore, due to the intensification of the flow over the crest, vertical shear and, as a consequence, vorticity is high and positive over the crest.

4.3 Turbulent kinetic energy

The distribution of turbulent kinetic energy (TKE) at different phases of the forcing cycle is depicted in Figure 4.12. A region of higher TKE confined between the crest and the trough is clearly depicted downstream of the ripple crest. High TKE is confined to a central core, and decays outwards. At 90° phase, the magnitude of the TKE is larger and decays as the free-stream velocity decelerates. As the separation bubble increases in size and begins to detach from the ripple flank (Figure 4.7), turbulent kinetic energy diffuses from the high

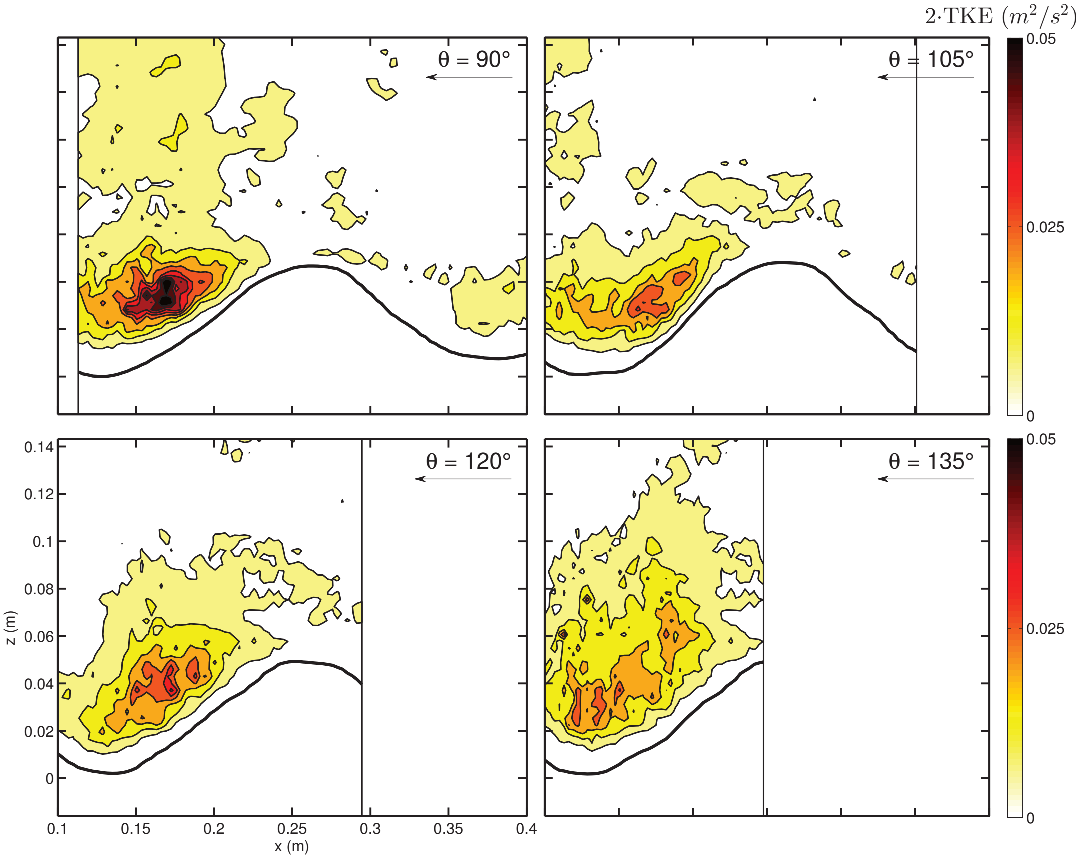

Figure 4.12: Turbulent kinetic energy at four phases of the forcing cycle. The sediment-water interface is indicated in black and the direction of the free-stream velocity is indicated by an arrow.

TKE core into the water column. This high TKE core is associated with the lee vortex.

The phase-averaged TKE components $\overline{u'^2}$, $\overline{v'^2}$ and $\overline{w'^2}$ at 90° phase are shown in Figure 4.13. The high TKE core is present to varying degrees in all three components. The main contribution to the TKE comes from the second moment of the horizontal component of turbulent velocity fluctuations, namely $\overline{u'^2}$. The turbulent kinetic energy is clearly anisotropic, meaning that it is dependant on direction.

4.4 Reynolds stress

The phase-averaged Reynolds stress at four different phases of the forcing cycle is presented in Figure 4.14. Similar to the TKE, patches of higher Reynolds stress associated with the

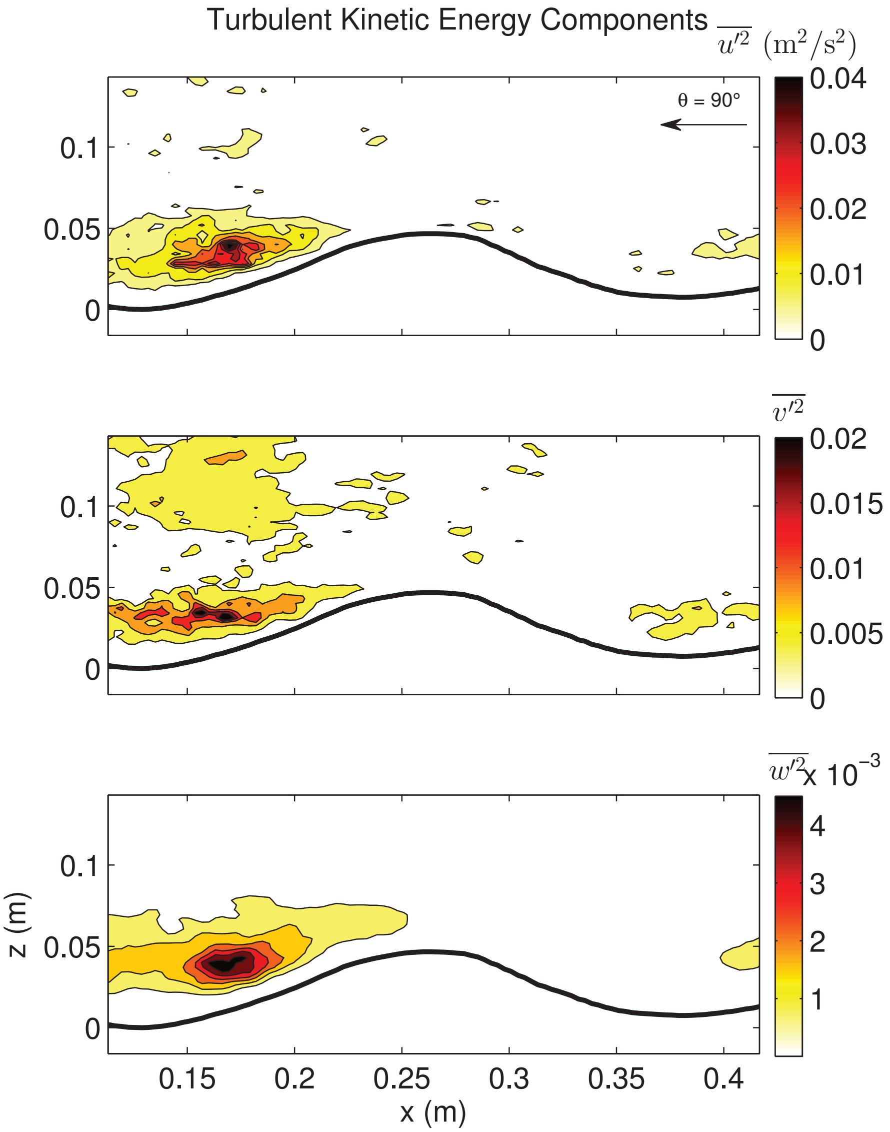

Figure 4.13: Turbulent kinetic energy components $\overline{u'^2}$, $\overline{v'^2}$ and $\overline{w'^2}$ at 90° phase. The sediment-water interface is indicated in black and the direction of the free-stream velocity is indicated by an arrow.

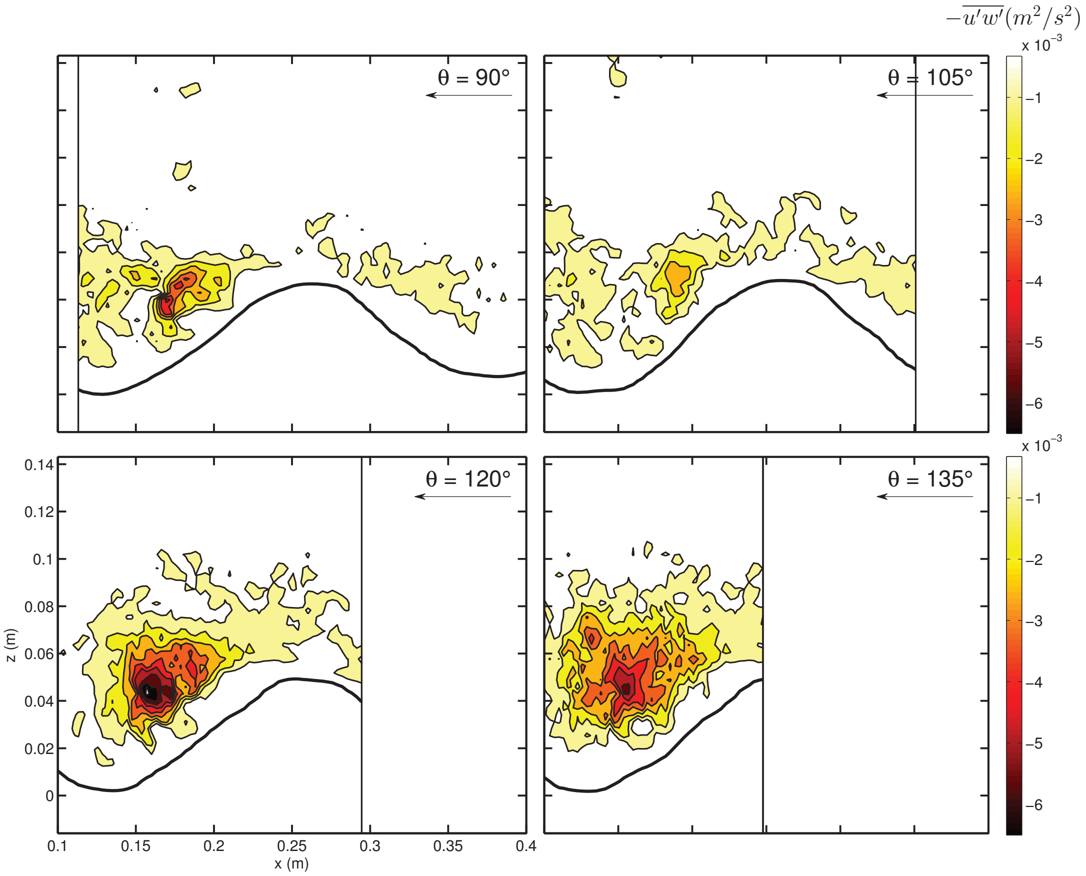

Figure 4.14: Phase-averaged Reynolds stress at four phases of the forcing cycle. The sediment-water interface is indicated in black and the direction of the free-stream velocity is indicated by an arrow.

presence of the lee vortex are found downstream from the ripple crest. Higher stress is located at the centre of the vortex and decays outwards. The peak Reynolds stress occurs after the time of maximum forcing as the lee vortex starts to detach from the ripple face.

4.5 Turbulence production

The evolution of turbulence production is presented in Figure 4.15. Turbulence production is given by the product of Reynolds stress and vertical shear (equation 2.67). Patches of positive turbulence production are confined close to the bed with a maximum located in the lee of the ripple crest. This distribution of turbulence production is expected since both Reynolds stress and vertical shear were shown to be large downstream from the ripple

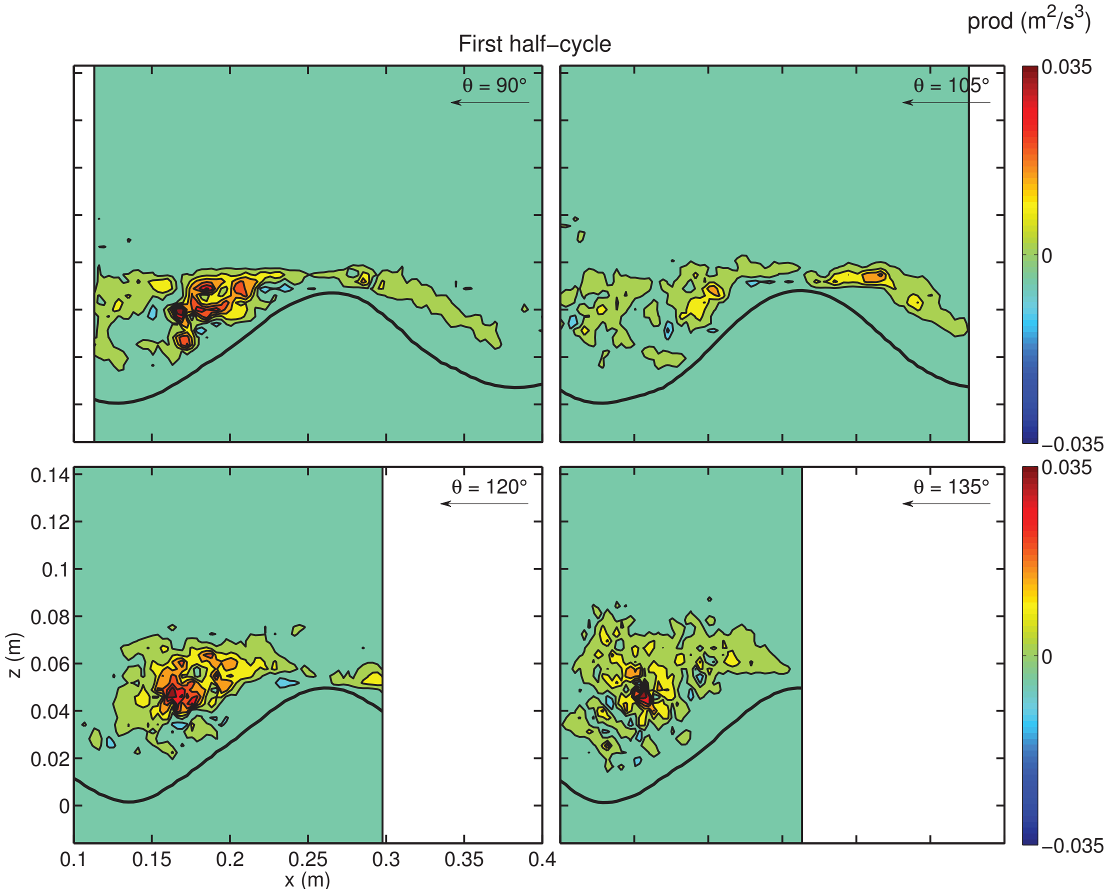

Figure 4.15: Distribution of the production of TKE at four different phases of the forcing cycle. The sediment-water interface is indicated in black.

crest. Furthermore, the amount of turbulence generated by the lee vortex evolves over time. Production of turbulence is highest at the time of maximum forcing. A secondary maximum of turbulence production is also present at 120° phase when the lee vortex starts to detach from the ripple face. Patches of negative turbulence could be artifacts due to noise.

4.6 Vertical profiles of stress and turbulence

Vertical profiles of Reynolds stress, turbulent kinetic energy and turbulence production through the TKE maximum in the lee vortex at phases of 90° and 120° are shown in Figure 4.16. At 90° phase, all three panels exhibit a clear extremum at the same height just below the ripple crest and at $\sim$4 cm above the ripple trough. At 120° phase, the Reynolds stress

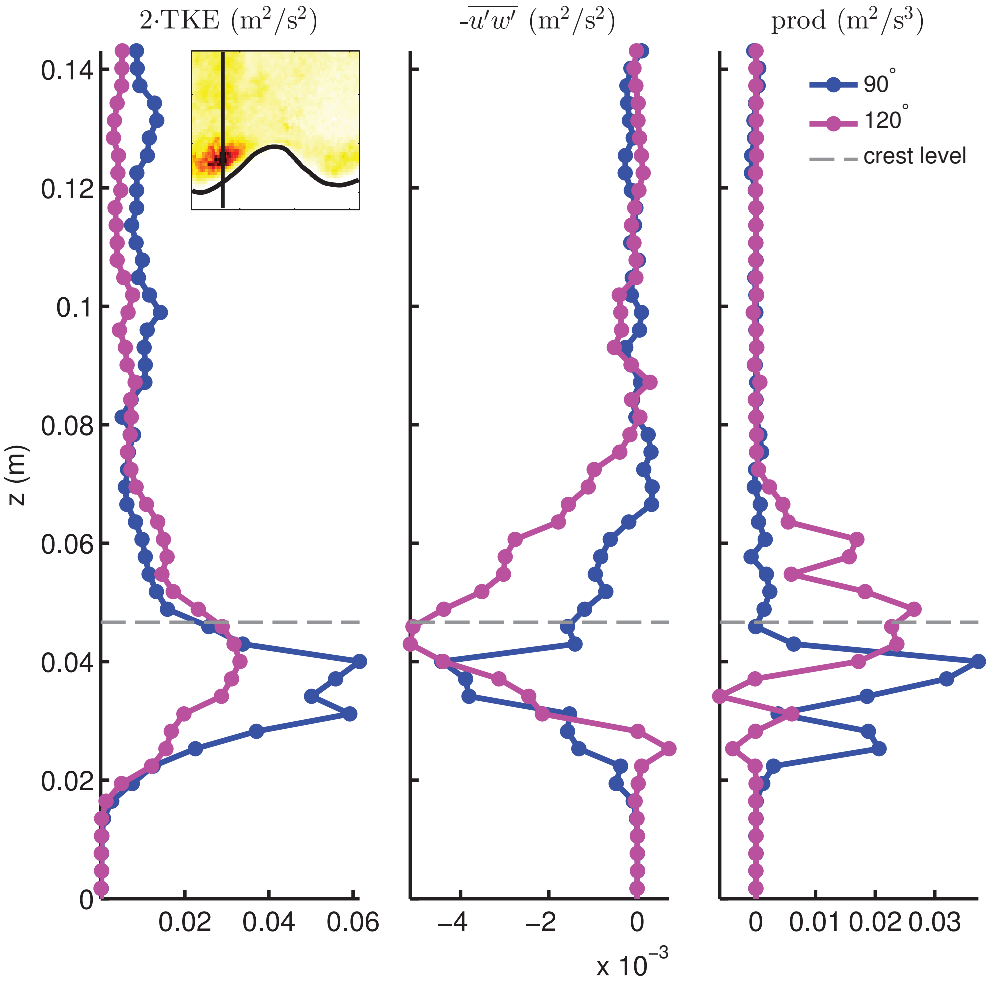

Figure 4.16: Vertical profiles of Reynolds stress, turbulent kinetic energy and turbulence production through the lee vortex at two phases. The location of these vertical profiles is shown by the vertical line in the inset of the TKE distribution.

and turbulence production extrema are higher above the bed, consistent with the lee vortex being advected away from the bed and into the interior. The maximum TKE decreases from 90° to 120°.

4.7 Law-of-the-wall

Best fits of $u(z)$ to the law-of-the-wall are plotted in Figure 4.17 for different positions along the ripple profile at 90° phase. The top panels are for the first half-cycle, the bottom panels for the second half-cycle. The crest position is not included since the log layer above the crest was not well resolved. For every profile, the crest level and local bed level are indicated. The fits were computed only on the part of the profile that exhibited the characteristic logarithmic behaviour. These points are indicated by open circles. Due to its variable thickness over ripples, the logarithmic layer was often difficult to define objectively. Hence, questions about the applicability of the law-of-the-wall can be raised since this method is sensitive to the selection of appropriate data points (discussed further in section 4.15).

The fits are better over the zero-crossings than over the troughs. A close-up of these fits over the zero-crossings is shown in a semi-logarithmic plot in Figure 4.18. In this way, the logarithmic behaviour of the vertical profiles is quite evident. The lee vortex is located over zero-crossing A during the first half-cycle and over zero-crossing B during the second half-cycle.

The parameter estimates obtained from the log-law fits are given in Figure 4.19. The friction velocity u_* exhibits a semi-sinusoidal pattern for each half-cycle with lower values in the troughs and higher values over the zero-crossings. Similar to the fixed roughness flat bed and small amplitude rippled bed results reported by *Hay et al.* (2012c), u_* is dominantly negative during the first half-cycle and positive during the second half-cycle. In addition, the friction velocity is higher over the zero-crossings and lower over the troughs. Similarly, the roughness height parameter z_0 is lower over the troughs and higher over the zero-crossings.

4.8 Bed shear stress from vorticity

The bed shear stress can be determined from the vertically-integrated vorticity equation using equation 2.62, repeated here

$$\frac{\tau^x}{\rho} \simeq \int\limits_z^\infty \left[\int\limits_z^\infty \frac{\partial \zeta}{\partial t} dz + w\zeta \right] dz \tag{4.1}$$

This equation assumes that the horizontal length scales are much greater than the vertical length scales. In order to obtain reliable results, this assumption was necessary since the $\partial(u\zeta)/\partial x$ term was very noisy due to the x derivative.

The time derivative of vorticity was estimated as $\omega\zeta$. The two terms that are used in determining the bed stress ($\int \partial\zeta/\partial t dz$ and $w\zeta$) and their sum ($\partial\tau/\partial z$) at maximum

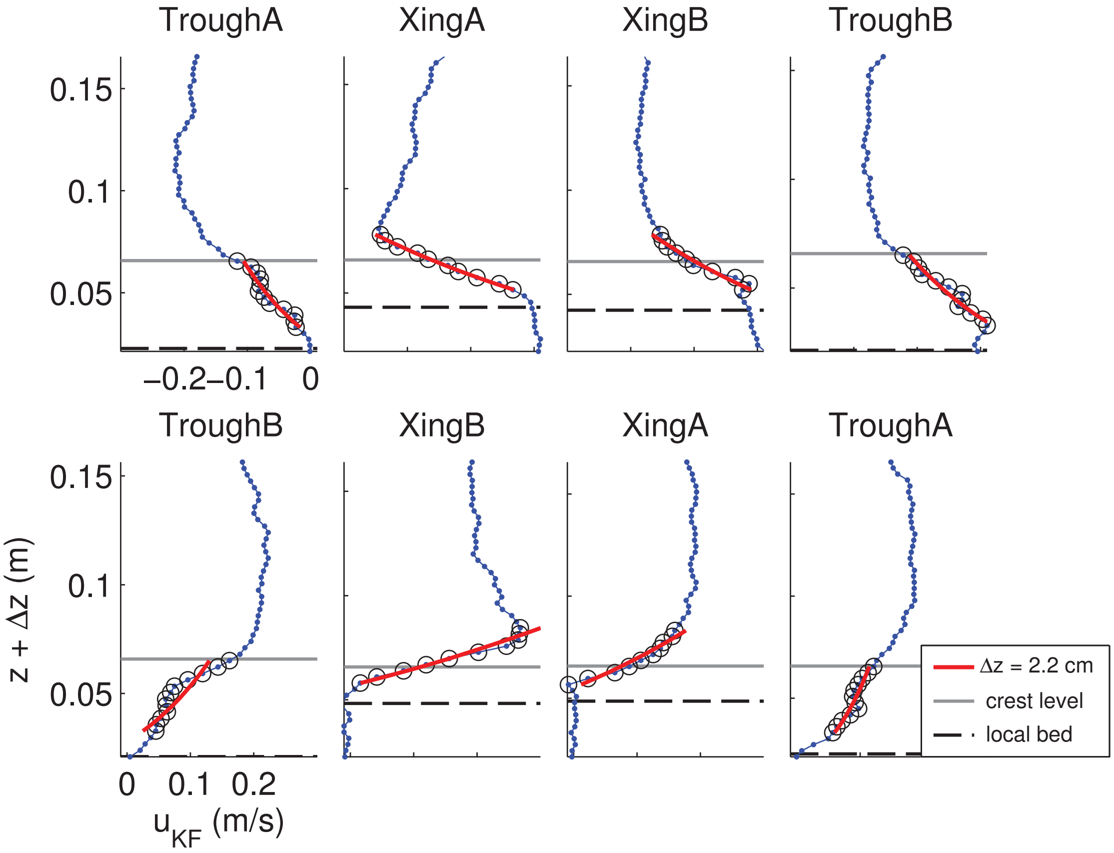

Figure 4.17: Vertical profiles of horizontal flow (blue) at certain positions (troughs and zero-crossings) along the ripple profile at maximum forcing (90°±12° phase or 270 °±12° phase) as a function of $z + \Delta z$. The logarithmic fits (red) were only executed on a restricted portion of the profile (black open circles). The crest level (solid grey line) and local bed level (dashed black line) are included. Data from the first half-cycle are shown in the top panels, whereas data from the second half-cycle are shown in the bottom panels.

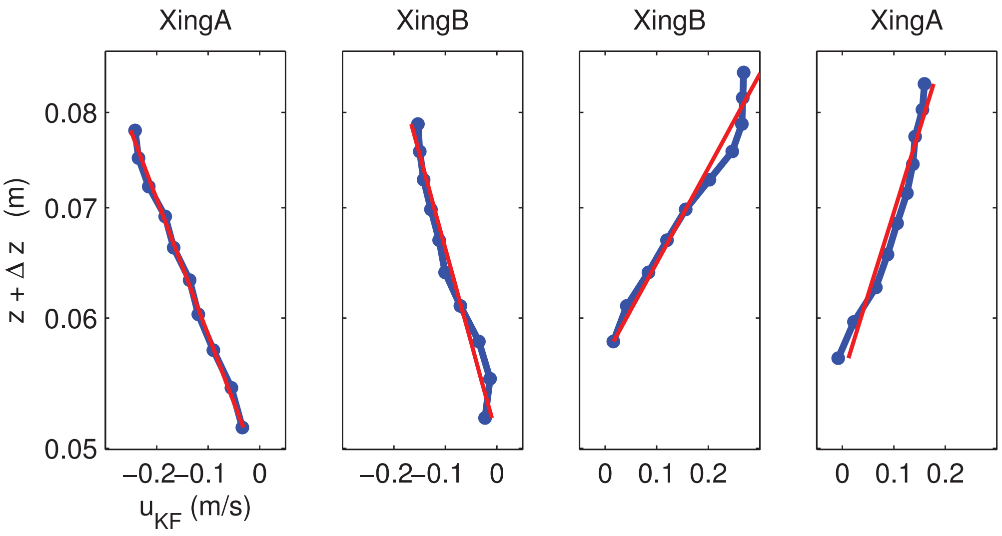

Figure 4.18: Semi-logarithmic plot of the vertical profiles of horizontal flow (blue) at the zero-crossings along the ripple profile at maximum forcing (90°±12° phase or 270 °±12° phase) as a function of $z + \Delta z$. The logarithmic fits are shown in red. Data from the first half-cycle are shown in the first two panels, whereas data from the second half-cycle are shown in the last two panels.

forcing are presented in Figure 4.20. The magnitude of the integral of the time-derivative of vorticity is much smaller than the $w\zeta$ term. As a result, the distribution of $\partial\tau/\partial z$ is similar to the distribution of $w\zeta$. The bed stress τ_0/ρ is presented in the last panel of Figure 4.20. The stress is negative downstream from the ripple crest and positive upstream of the ripple crest.

The net stress over a full ripple wavelength given by the horizontal integral of the bed shear stress,

$$\frac{\tau_{net}}{\rho} = \frac{1}{\lambda}\int_{0}^{\lambda} \frac{\tau_0(x)}{\rho} dx \tag{4.2}$$

is estimated to be -2.6×10^{-3} $\mathrm{m^2/s^2}$ for the first half-cycle and 2.0×10^{-3} $\mathrm{m^2/s^2}$ for the second half-cycle. The opposite signs indicate that the total bed shear stress reverses direction for each half-cycle.

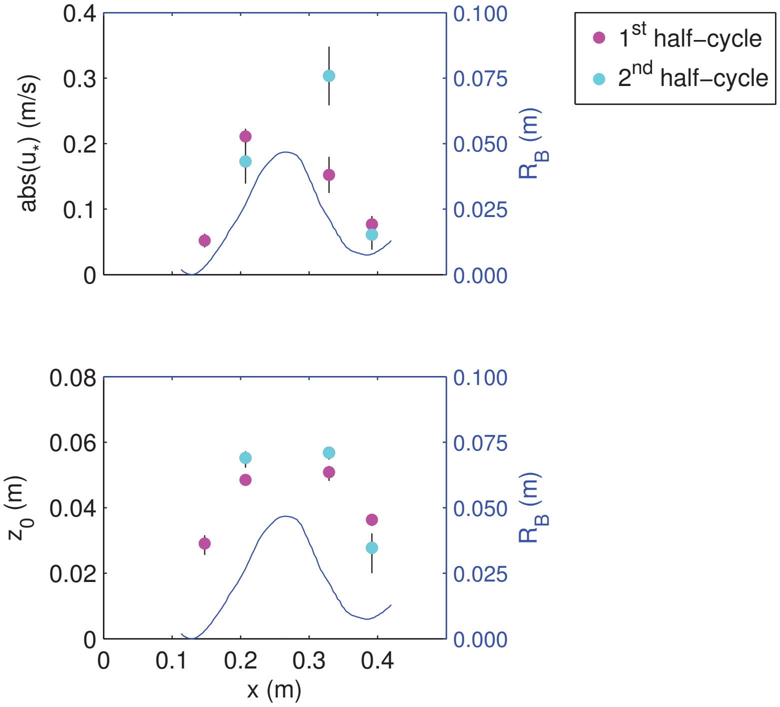

Figure 4.19: Law-of-the-wall parameters (friction velocity u_* and roughness height z_0) for both half-cycles at different positions along the ripple profile at maximum forcing (90° phase or 270° phase). The sediment-water interface R_B is indicated in blue.

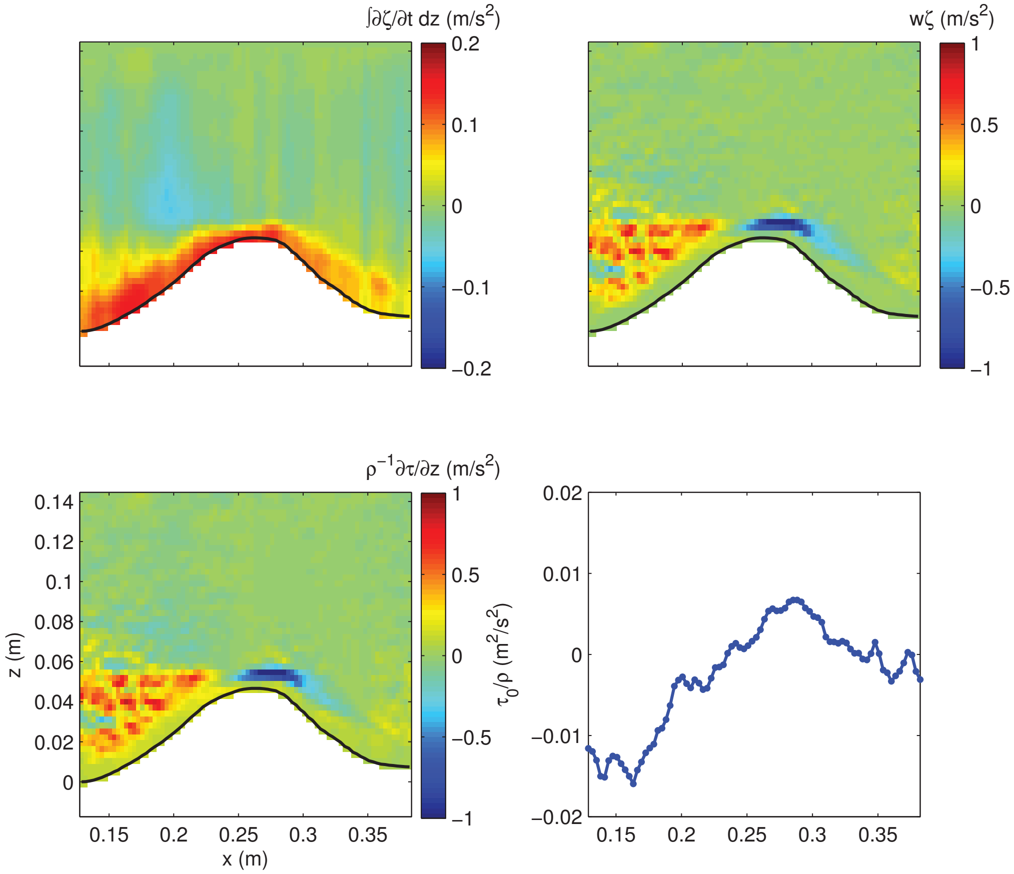

Figure 4.20: Vertical integral of the time-derivative of vorticity ($\int \partial\zeta/\partial t dz$), the product of vorticity and vertical flow ($w\zeta$), the vertical derivative of stress ($\partial\tau/\partial z$) and the bed shear stress (τ_0/ρ).

4.9 Bedform-induced shear stress

The bedform-induced shear stress discussed in section 2.4.5 is given by $\langle\tilde{u}\tilde{w}\rangle_s = \psi(z)\langle\tilde{u}\tilde{w}\rangle$ where the angle brackets represent the spatial average over a full ripple wavelength. The spatial fluctuations $\tilde{u}$ and $\tilde{w}$ of the phase-averaged flow, as well as their product are shown in Figure 4.21. The spatial fluctuation of the horizontal flow is confined to the near-bed region and is mainly negative downstream of the ripple crest and positive upstream of the ripple crest. The spatial fluctuation of the vertical flow exhibits very similar features to the phase-averaged flow shown in Figure 4.5. Similar to the phase-averaged results, the magnitude of $\tilde{u}$ is larger than the magnitude of $\tilde{w}$. The product $\tilde{u}\tilde{w}$ indicates two areas where the correlation between the spatial fluctuations is high: around the ripple crest and downstream of the ripple crest. From section 3.4.4, it was concluded that velocity measurements could not be resolved any closer to the bed than 4 mm ± 2 mm. A close-up of $\tilde{u}\tilde{w}$ near the crest region is shown in Figure 4.21d, where the edge of the bottom return contamination zone is indicated in grey. It is evident that the region of large $\tilde{u}\tilde{w}$ located near the ripple crest is partially contaminated by the bottom return, thereby reducing its value.

The double-averaged Reynolds stress $-\langle\overline{u'w'}\rangle_s$ and the double-averaged form-induced shear stress $-\langle\tilde{u}\tilde{w}\rangle_s$ are compared in Figure 4.22. Both stresses exhibit similar profiles: zero shear stress at the bed and away from the bed, as well as a peak just above the ripple crest. The magnitude of the form-induced stress is, for the most part, smaller than the magnitude of the Reynolds stress. The shear stress peak represents the amount of momentum being removed from the mean flow by the ripples. Except for a sign difference, both half-cycles exhibit similar behaviour of the double-averaged stresses.

4.10 Evolution of the double-averaged shear stress

The combined double-averaged shear stress is given by the sum of the double-averaged bedform-induced stress and Reynolds stress:

$$\frac{\tau}{\rho} = -\langle\tilde{u}\tilde{w}\rangle_s - \langle\overline{u'w'}\rangle_s \tag{4.3}$$

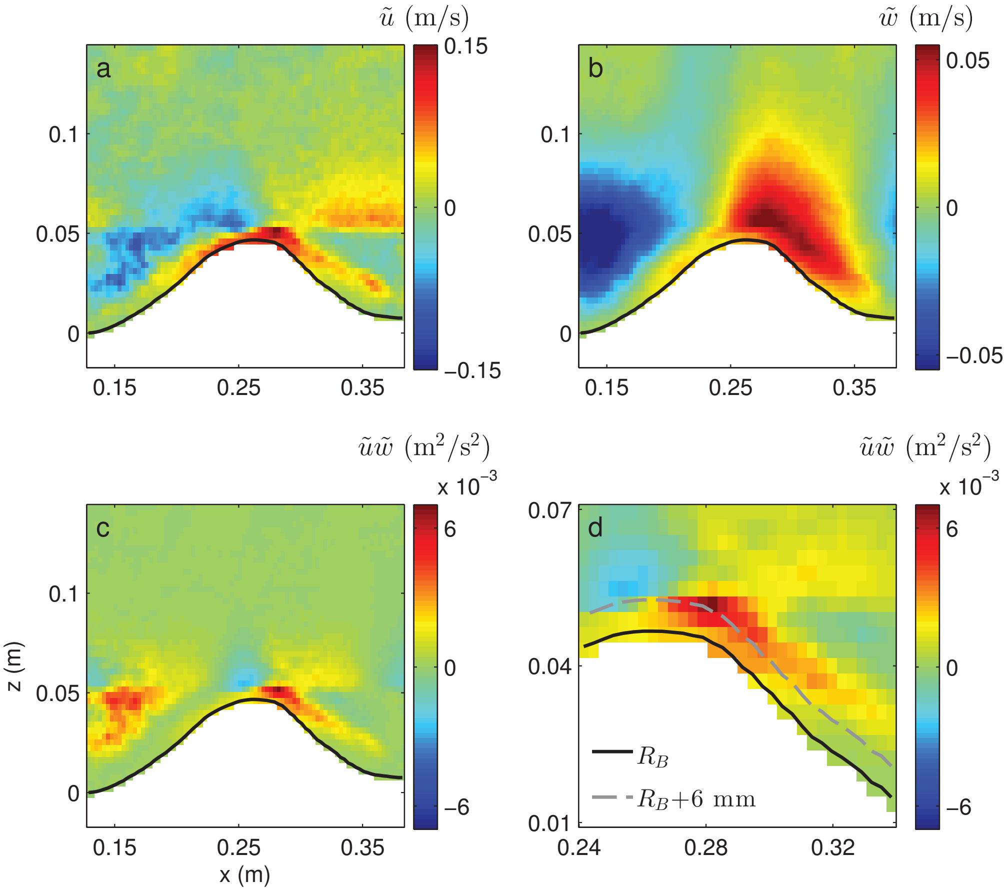

Figure 4.21: Spatial fluctuations $\tilde{u}$ and $\tilde{w}$ of the phase-averaged flow and their product over a full ripple wavelength at 90°. A close-up of $\tilde{u}\tilde{w}$ near the crest region is shown in panel d. The sediment-water interface R_B is indicated in black.

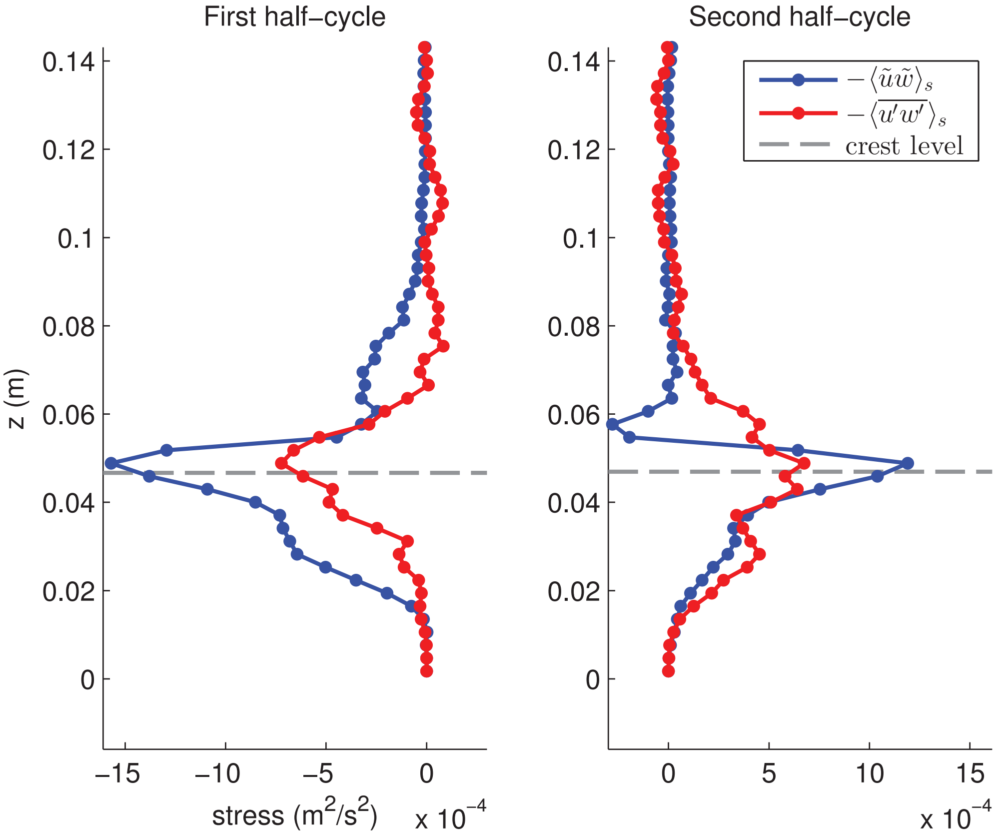

Figure 4.22: Double-averaged Reynolds stress $-\langle u'w' \rangle_s$ and double-averaged form-induced stress $-\langle \tilde{u}\tilde{w} \rangle_s$. The crest level is indicated by the grey dashed line.

Previously, the double-averaged stress at 90° phase was determined over a full ripple wavelength. At later times in the forcing cycle, the data spans different portions of the ripple profile. In order to determine the double-averaged stress at different phases, a slightly different method must be implemented, whereby the double-averaging procedure is applied over a half-wavelength (trough to crest) for each half-cycle. This method is valid as long as the ripple profile is symmetrical or, as in our case, nearly symmetrical. The downstream ripple flank is located to the left of the ripple crest during the first half-cycle. During the second half-cycle, the upstream ripple flank is also located to the left of the ripple crest. With this in mind, the profiles of shear stress double-averaged over half a wavelength for each half-cycle can thus be summed together, yielding the double-averaged stress over a full ripple wavelength.

The evolution of the vertical profiles of the total combined shear stress double-averaged over a half-wavelength is presented in blue in Figure 4.23 at the same four phases as in Figure 4.7. The magenta and green lines represent the combined stress averaged over a half-wavelength for each half-cycle. The stress is dominantly negative during the first half-cycle and positive during the second half-cycle. For all four phases, the peak shear stress for each half-cycle is located near crest level. The maximum stress in each vertical profile as a function of phase is shown in the polar plot in Figure 4.24. The maximum total shear stress is shown in blue and the maximum stress from each half-cycle is given by the magenta and green lines. Since the maximum stresses for each half-cycle are located at different heights above the bed, their sums do not necessarily equal the maximum total shear stress. Except at 105° phase, the maximum total shear stress increases as function of phase.

4.11 Different orbital excursions

The following section examines the near-bed flow and stress at a larger excursion with the intention of studying evolving ripples. A new bed of ripples was created at an excursion of 49.6 cm. MFDop measurements were then made at two RippleKart excursions: 49.6 cm and 60.5 cm. At the higher excursion, the ripples were slowly evolving to the longer wavelength expected for the larger excursion, and were thus out of equilibrium. The trough-to-trough ripple wavelength λ and ripple amplitude a for each 40-cycle run are listed in Table 4.1. The runs were consecutive: i.e. without stopping the Kart. Ripple

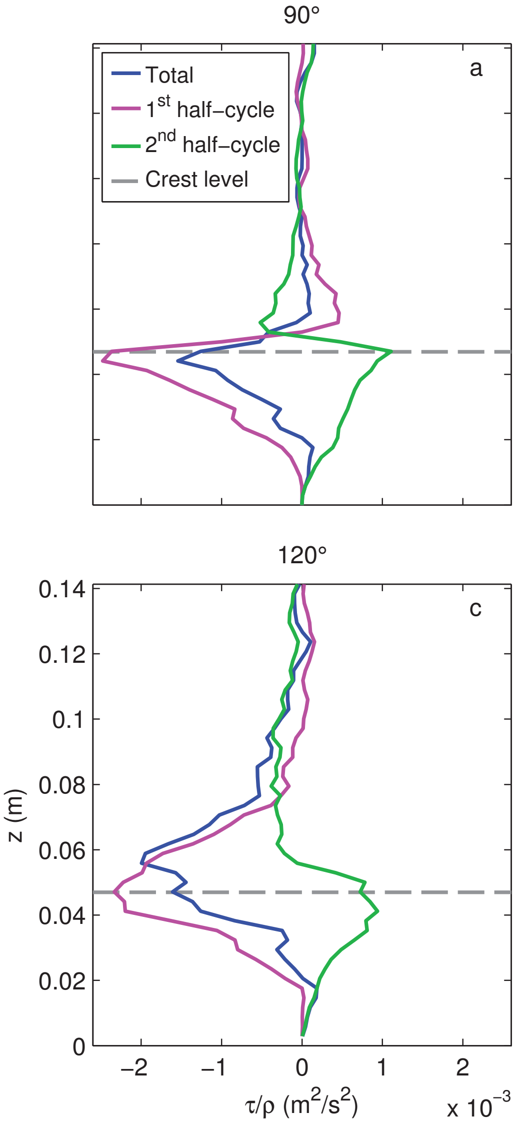

Figure 4.23: Double-averaged stress at four phases of the forcing cycle. The combined stress double-averaged over a half-wavelength for each half-cycle are indicated in magenta and green, as well as their sum in blue. The crest level is given by the dashed grey line.

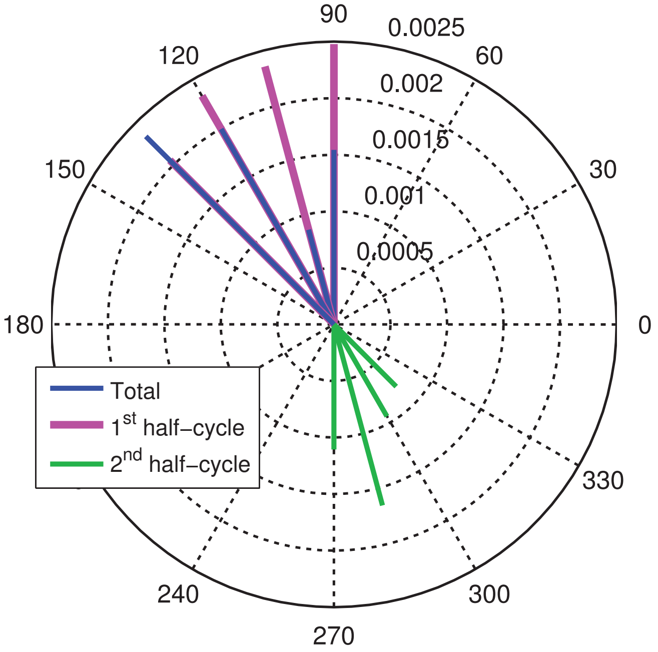

Figure 4.24: Maximum shear stress double-averaged over a half-wavelength (blue) and maximum shear stress from each half-cycle (magenta and green) as a function of phase.

wavelengths and amplitudes were determined from the sediment-water interface estimate R_B. For d_0 = 49.8 cm, the ripple parameters varied little between runs with an average wavelength of 24.6 cm ± 0.2 cm and an average amplitude of 2.22 cm ± 0.09 cm. For the other two excursions, there is a slightly greater difference between runs for these parameters, indicating that the rippled bed had not yet reached equilibrium. A smaller ripple crest was present in one of the troughs during these experiments, which could affect the estimates of the ripple parameters. However, for these experiments, the best fit sinusoid used in determining R_B was based on a portion of the rippled bed that excluded this small ripple. Ripple wavelength estimates differ from the expected wavelength of 31 cm at the lower excursion (equation 1.1), possibly due to the finite length of the RippleKart. The bed profiles from the last set of experiments at the higher excursion are presented in Figure 4.25.

4.11.1 Flow and vorticity

Figure 4.26 shows the vorticity and flow field at the two different RippleKart excursions: 49.8 cm (top panel) and 60.5 cm (bottom panel). The ripple shape and size are similar in

Table 4.1: Ripple parameters over a bed of ripples at an excursion of 49.8 cm and over a different bed of ripples at excursions of 49.6 cm and 60.5 cm

	d_0					
	49.8 cm		49.6 cm		60.5 cm	
	λ (cm)	a (cm)	λ (cm)	a (cm)	λ (cm)	a (cm)
run 1	24.4	2.2	24.0	2.1	23.6	2.1
run 2	24.7	2.1	24.0	2.1	25.1	2.3
run 3	24.7	2.3	23.4	2.0	23.6	2.0
run 4	24.7	2.3	23.4	2.0		
run 5			23.4	2.0		
run 6			24.6	2.0		

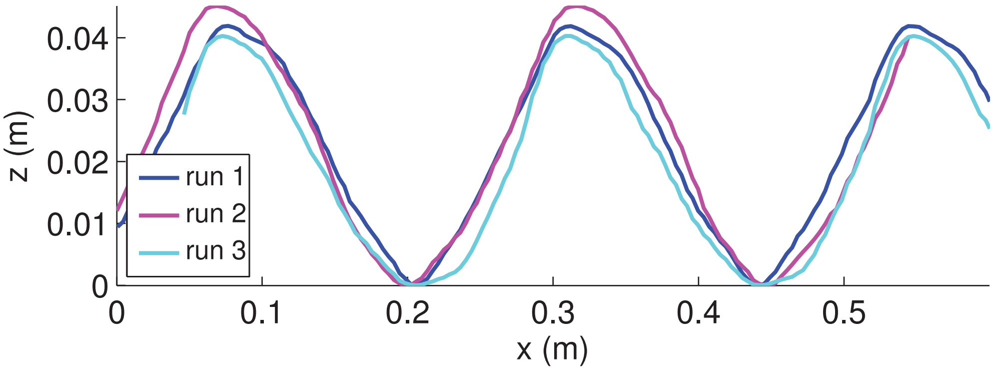

Figure 4.25: Phase-averaged bed profiles (R_B) at $d_0 = 60.5$ cm

both figures, indicating that the ripples had not yet adjusted to the higher excursion. Higher vorticity due to the intensification of the flow over the crest is evident at both excursions. The size of the separation bubble is larger at the larger excursion, indicating that given sufficient time the ripple wavelength would also increase.

4.11.2 Reynolds stress

The distribution of Reynolds stress at excursions of 49.8 cm and 60.5 cm, as well as at two phases of the forcing cycle, is shown in Figure 4.27. All panels exhibit a region of higher Reynolds stress downstream of the ripple crest. At the higher excursion, the high stress region increases in size from 90° to 105°, indicating that the maximum Reynolds stress occurs later than 90°. Furthermore, due to stronger flows at the higher excursion, the Reynolds stress associated with the lee vortex is much larger.

4.12 Maximum Reynolds stress and TKE

The error on the maximum Reynolds stress at 90° was estimated using the bootstrap method (*Efron and Gong*, 1983). This procedure consists of drawing a number of samples randomly and independently, with replacement, from the original distribution. In this case, each of the 40 cycles that was used in the phase-averaging procedure was assigned a unique integer, from 1 to 40, and 40 numbers were drawn at random, with replacement. A new phase-averaged Reynolds stress was computed from the 40 selected cycles, which obviously included some (random) repeats. The position and magnitude of the maximum Reynolds stress was then determined from the new distribution of phase-averaged Reynolds stress. This procedure was repeated a large number of times, B.

The position of the Reynolds stress maximum for two values of B is shown in the top panels of Figure 4.28. The variation of the magnitude of the Reynolds stress maximum is presented in the bottom panels. For both values of B, the largest number of occurrences of the maximum Reynolds stress occurred at the same location ($x =$17.2 cm and z = 4.0 cm). The magnitude of the Reynolds stress for both values of B is -0.0051 m^2/s^2, which is comparable to the magnitude of the maximum Reynolds stress of the pieced profile of -0.0044 m^2/s^2 found at $x =$17.0 cm and z = 4.0 cm. For both values of B, the distribution of the magnitude of the maximum Reynolds stress follow a quasi-normal distribution with a standard deviation relative to the peak value of 0.0016 m^2/s^2.

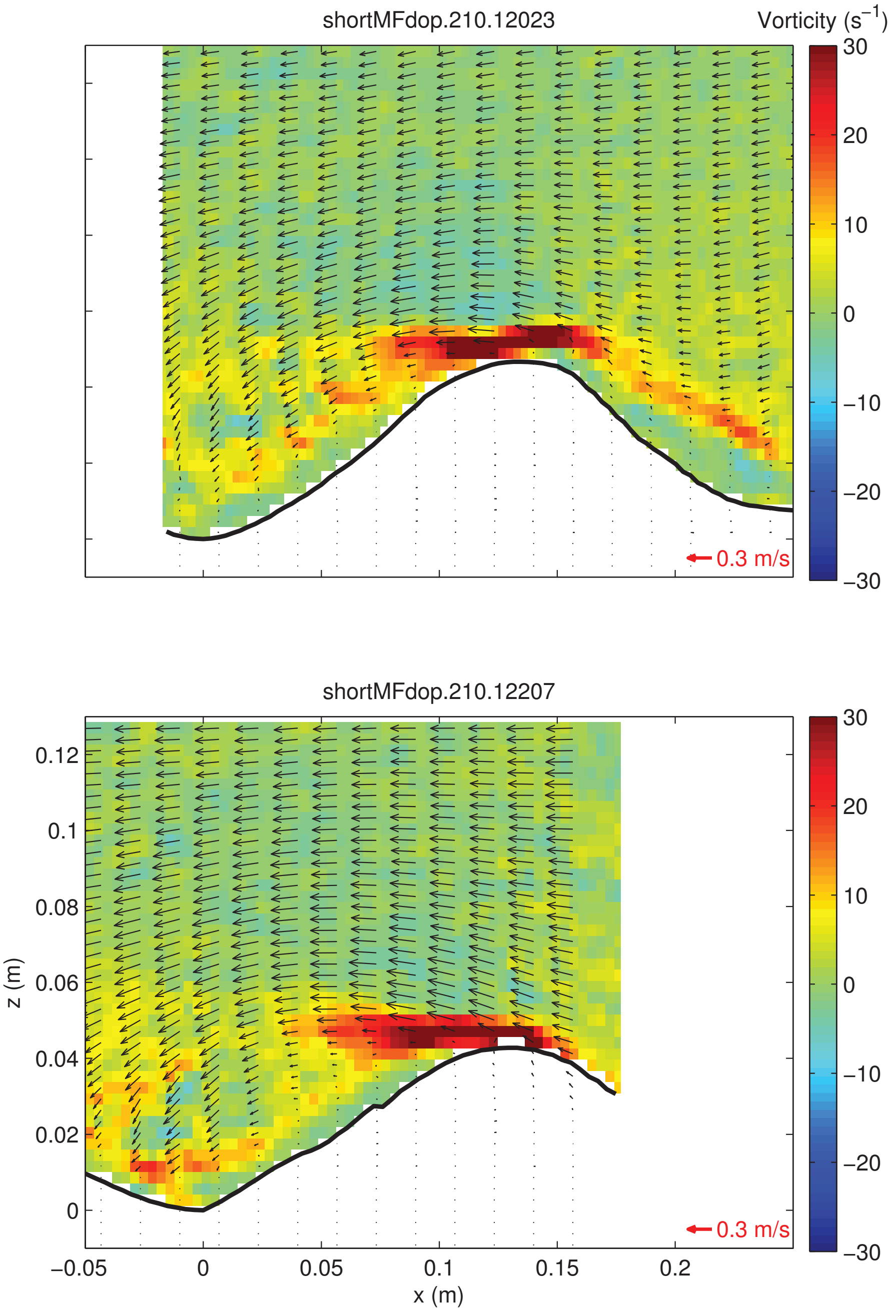

Figure 4.26: Vorticity and flow field at maximum forcing at two excursions: $d_0 = 49.8$ cm (top) and $d_0 = 60.5$ cm (bottom).

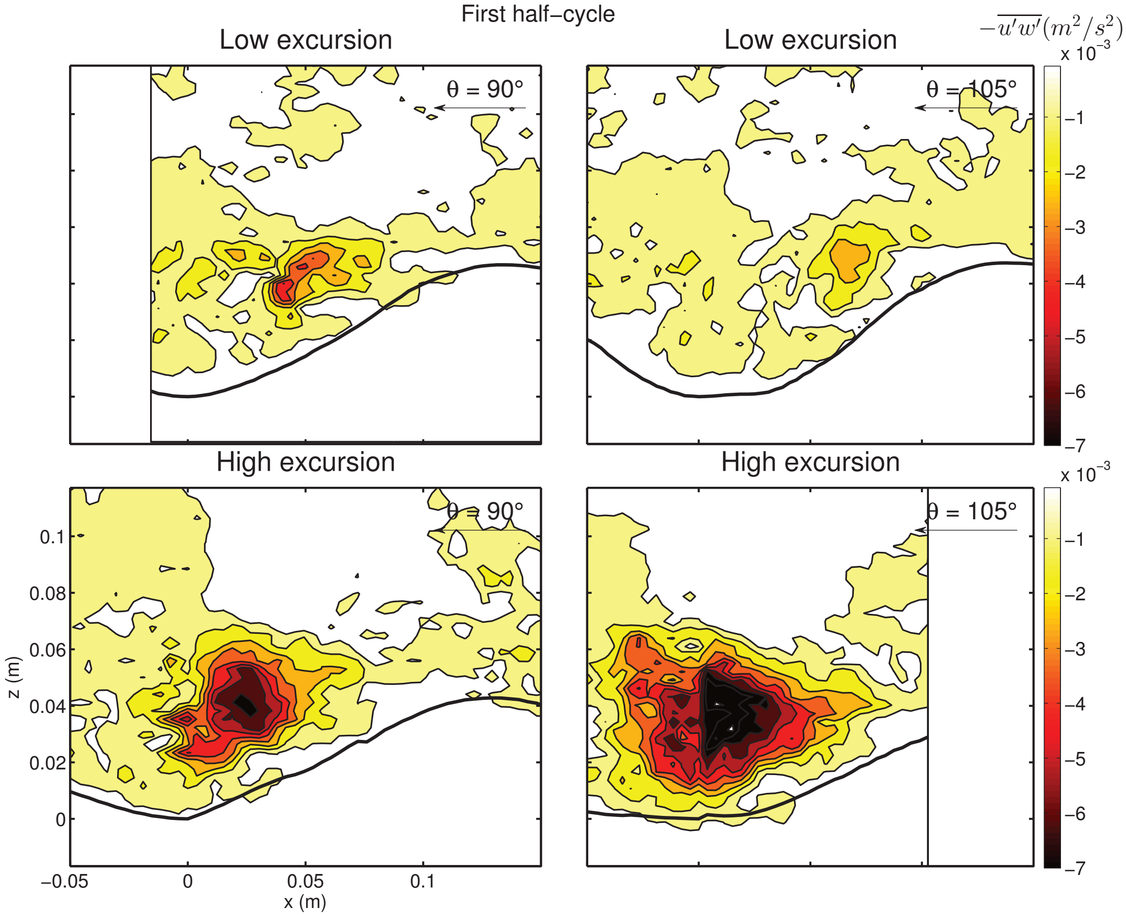

Figure 4.27: Reynolds stress distribution at 2 different excursions (49.8 cm and 60.5 cm) and at different phases (90° and 105°) during the first half-cycle. The sediment-water interface is indicated in black.

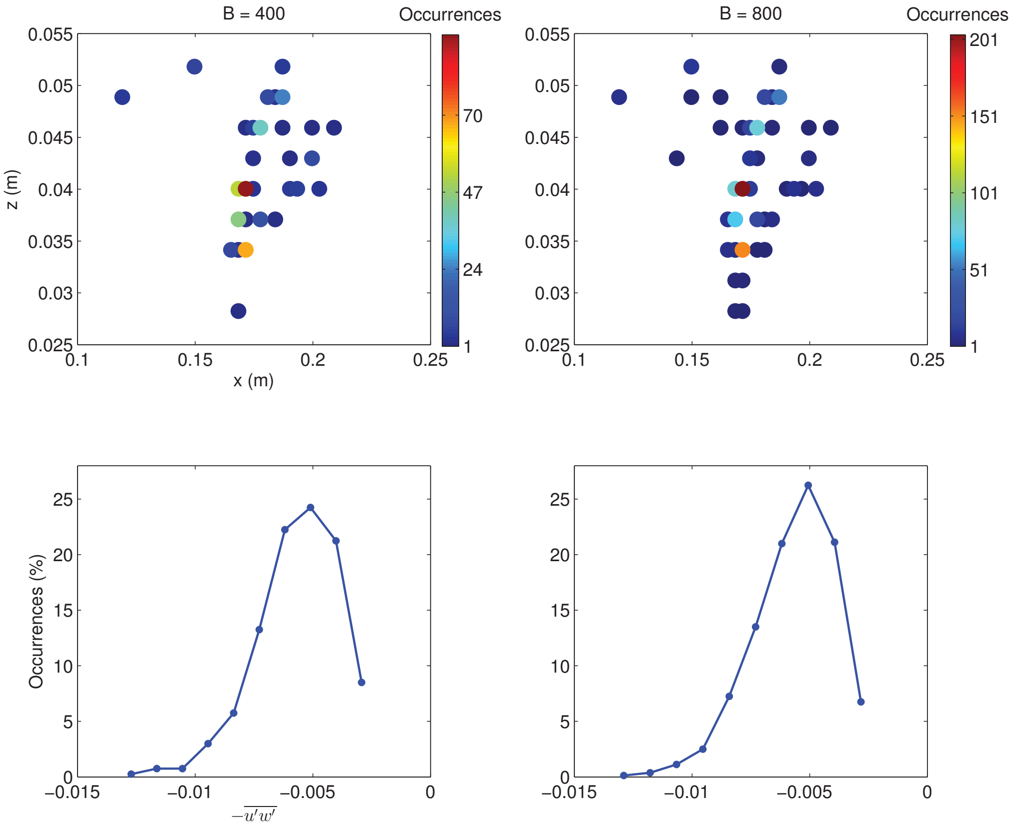

Figure 4.28: The position (top panels) and magnitude (bottom panels) of the maximum Reynolds stress at two values of B using the bootstrap method.

Table 4.2: Magnitude and location of the maximum Reynolds stress and TKE components using the Bootstrap method with B = 800

	magnitude (cm^2/s^2)	x (cm)	z (cm)
$-\overline{u'w'}$	-51 ± 16	17.2 ± 0.9	4.0 ± 0.5
$\overline{u'^2}$	490 ± 160	17.2 ± 0.7	4.0 ± 0.5
$\overline{v'^2}$	310 ± 120	16.8 ± 1.5	3.1 ± 1.6
$\overline{w'^2}$	50 ± 10	16.5 ± 0.6	3.7 ± 0.2

The bootstrap method can also be applied to the different TKE components. For $B =$ 800, the largest number of occurrences for the three TKE components are indicated in Table 4.2 and compared to the Reynolds stress results. The location of the maximum TKE components are comparable to each other and to the maximum TKE of the original pieced profile located at x =16.95 cm and z = 4.0 cm. The magnitude of the maximum TKE components differ, which indicates the degree of anisotropy of the high TKE core associated with the presence of the lee vortex. As discussed earlier (see section 4.3 and Figure 4.13), the largest contribution to the maximum TKE comes from $\overline{u'^2}$.

4.13 Friction factors

The maximum friction velocity during a half-cycle was determined from the maximum shear stress estimate τ_m using

$$u_{*m} = \sqrt{\tau_m/\rho} \tag{4.4}$$

Similar to equation 2.10, friction factors are given by

$$f_w = 2\frac{{u_{*m}}^2}{{U_{R0}}^2} \tag{4.5}$$

where U_{R0} is the amplitude of the relative velocity.

4.13.1 Single profiles of shear stress

Friction factors determined using the different methods (law-of-the-wall, vorticity method and Reynolds stress) at maximum forcing are listed in Table 4.3. The u_{*m} estimates determined via the log-law are based on the maximum values of friction velocities from the velocity profiles at the zero-crossings and troughs. In this case, the u_{*m} estimate is a local maximum. On the other hand, the maximum friction velocities determined from the vorticity method correspond to the maximum bed shear stress over a full ripple wavelength. The friction velocities determined from the Reynolds stress correspond to the maximum stress typically located above the bed.

For the vorticity method, friction factors could not be obtained at the largest excursion since the data at maximum forcing do not span a full ripple wavelength. Both the law-of-the-wall and the Reynolds stress methods yield larger friction velocities at the highest excursion. Friction factors obtained using the vorticity method are smaller than the law-of-the-wall results, but larger than the Reynolds stress estimates. For the most part, the f_w estimates are comparable for both half-cycles. However, there is as much as a factor 2 difference between half-cycles at a given excursion for the Reynolds stress and log-law estimates. The vorticity estimates are more consistent.

4.13.2 Spatially-averaged shear stress

Friction factors obtained from the spatially-averaged stress using the vorticity method (equation 4.2) and the combined double-averaged shear stress (equation 4.3) are presented in Table 4.4. Again, the f_w estimates could not be determined at the highest excursion of 60.5 cm, since the data at maximum forcing do not span a full ripple wavelength. The two methods yield similar results for both half-cycles. Due to averaging, friction factors obtained using these spatially-integrated methods are, for the most part, smaller than the friction factors from the single profiles presented in Table 4.3.

4.13.3 Spatially-averaged shear stress versus phases

Friction factors can also be obtained from the total combined shear stress profiles double-averaged over a half-wavelength. In this case, the friction velocity estimates correspond to the maximum total shear stress (blue lines in Figure 4.23). These friction velocities and their corresponding friction factors are presented in Table 4.5 as a function of phase. In addition, the friction factor estimate at 90° is very similar to (only 33% smaller than) the f_w estimate at 90° obtained from the stress double-averaged over a full wavelength (Table 4.4). Except for the results at 105°, friction factors increase with phase. The lower stress estimate at 105° phase could be influenced by a larger stress estimate during the second half-cycle (Figure 4.24) and by the decrease in Reynolds stress at this phase (Figure 4.14).

Table 4.3: Single-profile values of friction factors obtained using the law-of-the-wall, the vorticity method and Reynolds stress at 90°

	Log-law		Vorticity		Reynolds	
d_0 (cm)	${u_{*m}}^{\dagger}$ (cm/s)	f_w	${u_{*m}}^{\ddagger}$ (cm/s)	f_w	${u_{*m}}^{\dagger\dagger}$ (cm/s)	f_w
First half-cycle						
49.8	21.1	2.5	12.6	0.88	6.7	0.25
49.6	22.6	2.8	14.9	1.25	4.6	0.12
60.5	26.2	2.5	-	-	8.3	0.24
Second half-cycle						
49.8	30.3	5.3	13.8	1.16	6.3	0.24
49.6	16.0	1.4	15.0	1.43	6.5	0.27
60.5	27.8	2.7	-	-	7.5	0.26

† maximum value from the profiles at the zero-crossings and troughs (see Figure 4.19)

‡ corresponding to the maximum stress at the bed (see equation 4.1)

†† corresponding to the maximum stress, typically located above the bed (see Figure 4.14)

Table 4.4: Friction factors obtained from spatially-averaged values of stress using the vorticity method and the double-averaging method

	Vorticity		Double-average	
d_0 (cm)	${u_{*m}}^{\dagger}$ (cm/s)	f_w	${u_{*m}}^{\ddagger}$ (cm/s)	f_w
First half-cycle				
49.8	5.1	0.14	4.8	0.13
49.6	4.4	0.11	4.4	0.11
Second half-cycle				
49.8	4.5	0.12	4.3	0.11
49.6	6.0	0.23	4.9	0.15

† corresponding to the average bed stress over a wavelength

‡ corresponding to the maximum combined stress double-averaged over a full wavelength (see equation 4.3)

Table 4.5: Friction factors obtained from the combined stress double-averaged over a half-wavelength at $d_0 = 49.8$ cm

Phase (°)	${u_{*m}}^{\dagger}$ (cm/s)	f_w
90	3.9	0.09
105	2.9	0.05
120	4.5	0.12
135	4.8	0.14

† corresponding to the maximum combined stress double-averaged over a half-wavelength

4.14 Hydraulic roughness

In section 2.5, a hydraulic roughness equation which included a contribution from moving sand grains over ripples was presented. Using $s = 2.6$ (sediment specific gravity for sand, *Sleath* (1984)) and $D_{50} = 153\mu$m, the hydraulic roughness r_h can be calculated from the friction factor and ripple geometry estimates. It was found that the contribution of the second term in equation 2.68 was 3% to 7%. Since the contribution from the moving sand grains is negligible, the hydraulic roughness of these ripples can be estimated from the roughness of the ripple profile $8\eta_0^2/\lambda$. This method yields roughness estimates of 5 to 7 cm.

For turbulent flow over rough beds, *Nielsen* (1992) suggests using a modified version of the semi-empirical formula given by *Swart* (1974) for f_w:

$$f_w = \exp[5.5(r_h/A)^{0.2} - 6.3] \tag{4.6}$$

Given f_w, equation 4.6 can be used to estimate r_h.

Using equation 4.6, the r_h estimates determined from the friction factors obtained from the single profiles of stress (Table 4.3) are listed in Table 4.6. Due to the variation in the f_w estimates using the different methods, the values of hydraulic roughness vary greatly between the law-of-the-wall, the vorticity method and the Reynolds stress. Furthermore, most of these r_h estimates are much larger than the hydraulic roughness values of 5 to 7 cm obtained from the ripple geometry. These results lead to questions about the reliability of the different methods, which will be addressed in section 4.15.

In Table 4.7, values of hydraulic roughness at maximum forcing determined from the spatially-averaged shear stress estimates (vorticity and double-averaging methods) are presented. For the most part, the values of r_h are comparable in magnitude to each other and to the hydraulic roughness estimate of 5 to 7 cm obtained from the ripple geometry.

Hydraulic roughness estimates determined from the combined shear stress from the half-wavelength method are listed in Table 4.8 as a function of phase of the forcing cycle. These hydraulic roughness estimates are comparable in magnitude to each other and to the estimates based on the combined shear stress from the full-wavelength method (Table 4.7). These r_h estimates are also comparable to the hydraulic roughness estimate of 5 to 7 cm obtained from the ripple geometry. Similar to the f_w estimates, hydraulic roughness increases as a function of phase, except at 105°.

4.15 Discussion

4.15.1 Law-of-the-wall

The law-of-the-wall was used to determine friction velocities and consequently, friction factors. Better fits to the log-law were obtained over the zero-crossings than over the troughs. However, difficulties arose in choosing the appropriate number of points to which the fits were applied. In fact, some of the velocity profiles exhibit the logarithmic behaviour very poorly. Thus, caution must be used when interpreting the law-of-the-wall results.

For fully rough turbulent flow for which $r_h u_*/\nu > 70$ (*Nielsen*, 1992), the hydraulic roughness over rough beds is given by (*Monin and Yaglom*, 1971)

$$r_h = 30 z_0 \tag{4.7}$$

Since $r_h u_*/\nu > 600$ in these experiments, the flow can be assumed to be fully rough turbulent for the present experiments. Using equation 4.7 and the law-of-the-wall results yields r_h estimates between 60 cm to 160 cm, which are physically unrealistic.

Jensen (1988) (see also *Jensen et al.* (1989)) implemented the law-of-the-wall to estimate friction velocity and hydraulic roughness for fixed roughness beds in oscillatory flow. In one of his experiments, *Jensen* (1988) obtained $u_{*m} = 6$ cm/s for 8-s period waves at a

Table 4.6: Hydraulic roughness r_h obtained using the law-of-the-wall, the vorticity method and Reynolds stress

	Log-law	Vorticity	Reynolds
d_0 (cm)	r_h (cm)	r_h (cm)	r_h (cm)
		First half-cycle	
49.8	97	44	14
49.6	105	58	6
60.5	116	-	17
		Second half-cycle	
49.8	158	55	14
49.6	62	64	15
60.5	124	-	18

Table 4.7: Hydraulic roughness r_h from the spatially-averaged stress using the vorticity method and the double-averaged method

	Vorticity	Double-Average
d_0 (cm)	r_h (cm)	r_h (cm)
	First half-cycle	
49.8	7.8	6.7
49.6	5.5	5.7
	Second half-cycle	
49.8	6.5	5.9
49.6	12.8	8.2

Table 4.8: Hydraulic roughness from the total combined shear stress double-averaged over a half-wavelength as a function of phase at $d_0 = 49.8$ cm

Phase (°)	r_h (cm)
90	4.6
105	2.1
120	6.4
135	7.7

semi-excursion of 1.13 m. The height of the roughness elements (grain size) was 1.5 mm for this experiment. The friction velocity was determined using the law-of-the-wall and assumed a constant roughness height z_0. From equation 4.7, the hydraulic roughness (r_h) was estimated to be 2.6 mm, yielding a r_h to grain size ratio of 1.7. In other experiments using different grain sizes and near-bed orbital excursions, *Jensen* (1988) found ratios of 2.5, which is in agreement with values reported by *Kamphuis* (1974). However, the median grain size D_{50} is used for the height of the roughness elements in *Jensen* (1988), whereas as D_{90} (90$\%$ of the particles are smaller than the total grain size distribution) is used in *Kamphuis* (1974).

In reference to the experiments executed by *Jensen* (1988) (see also *Jensen et al.* (1989)), it is important to realize that the log-law was implemented over a fixed roughness bed, with roughness element size much smaller than the excursion. As a result, the number of roughness elements that a fluid element encountered during one wave period was $A/D_{50} \sim$ O(1000), whereas in the rippled bed case $A/\eta_0 \sim 5$, where a full ripple wavelength is considered to be a roughness element. In addition, the logarithmic layer was defined above the roughness elements in the results presented by *Jensen* (1988). In contrast, the log layer here is confined for the most part to heights below crest level (see Figure 4.17) and thus between the roughness elements, i.e. the ripple crests. For this reason, the assumption of a constant roughness height z_0 (and displacement height) is not necessarily valid over a rippled bed, since the log-law needs to be implemented at different positions along the ripple profile.

In addition, the law-of-the-wall could have been implemented at several more locations along the ripple profile in order to obtain spatially-averaged stress estimates between the roughness elements. However, this avenue was not pursued since the results from the best fits (over the zero-crossings) yielded physically unrealistic r_h estimates and due to the above-mentioned difficulties in implementing the law-of-the-wall.

In the present work, the law-of-the-wall was also implemented to verify the existence of the logarithmic layer above crest level. It was found that the logarithmic nature of the time-averaged horizontal flow over the crest was confined to several millimetres above crest level. The existence of this logarithmic layer can also be investigated using the double-averaging method. Over developing dunes, *Coleman et al.* (2006) found that the double-averaged horizontal flow below the roughness heights is linear and obtained a logarithmic profile immediately above crest level. This behaviour was verified using the MFDop data (not shown). Furthermore, it was found that the logarithmic nature of the double-averaged horizontal flow as measured by the MFDop was confined to a very thin ($\sim$9 mm) layer above crest level. The logarithmic fit to this thin layer above crest level yielded high friction factors of 3 to 8, values which are for the most part larger than the f_w estimates from the law-of-the-wall applied to the time-averaged flow (Table 4.3).

4.15.2 Spatially-averaged stress and connection to evolving ripples

The hydraulic roughness estimates obtained from spatially-averaged results (double-averaging and vorticity methods) were comparable in magnitude to each other and to the r_h estimate obtained from the ripple geometry. Furthermore, the double-averaging technique was also implemented over a half-wavelength as a function of phase, yielding similar hydraulic roughness estimates. For these methods, the hydraulic roughness to roughness height (ripple height) lies between 1 and 3. Over evolving sand ripples, *Hay et al.* (2012c) also obtain a hydraulic roughness to ripple height ratio between 1 and 3. In these experiments, the ripple steepness increased from 0.03 cm to 0.10 cm at an excursion of 0.9 m. It is very encouraging to see that *Hay et al.* (2012c) obtained similar ratios even though their experiments involved smaller amplitude ripples evolving at a larger excursion. Stress estimates obtained using spatially-averaged approaches have yielded sensible hydraulic roughness to ripple height ratios, which are much more realistic than the values of 14 to 40 obtained via the law-of-the-wall. These results have thus shown that a spatially-averaged approach is a more appropriate method to implement in the case of a rippled bed.

CHAPTER 5

SUMMARY AND CONCLUSION

5.1 Summary

Results have been presented from a laboratory investigation of the spatial and temporal structure of flow, vorticity and stress over orbital-scale sand ripples. Equilibrium two-dimensional ripples having a wavelength of nearly 25 cm and an amplitude of 2 cm were created using an oscillating tray apparatus. Near-bed flow measurements were obtained using a wide-band coherent Doppler profiler (MFDop). Through runs at different MFDop locations relative to a particular ripple crest, phase-averaged results were pieced together in order to obtain an instantaneous picture of the flow field over a ripple wavelength.

5.1.1 Flow and vorticity field at maximum forcing

The main features of the flow that were observed were the acceleration of the flow up the stoss side of the ripple and its deceleration down the lee side, as well as the intensification of the flow over the crest. These flow features were also observed to varying degrees in the potential flow models. At the same non-dimensional height (z/λ), the intensification of the flow was 1.3 times larger than the free-stream velocity, compared to 1.2 and to 1.4 for the models given by *Davies* (1983) and *Longuet-Higgins* (1981), respectively (Figure 4.2). Differences between the model predictions and the observations in the near-bed flow field are due to bottom friction (which is not included in the models), verified by estimating the rotational part of the flow, and to the ripples being slightly three-dimensional. Areas of significant rotational flow confined close to the bed represent regions in the flow field that are affected by bed shear stress. Vertical profiles of horizontal flow, as well as the vorticity distribution over a ripple, indicate the presence of a layer of high vertical shear confined close to the bed due to bottom friction.

Based on both the MFDop data and the potential flow solutions, it was found that the local acceleration $\partial u/\partial t$ and the non-linear terms ($u\partial u/\partial x$ and $w\partial u/\partial z$) are not only comparable in magnitude within the boundary layer, but are also dependent on height above the bed. Thus, the boundary layer approximation does not hold over orbital-scale ripples, and shear stress cannot be accurately resolved using the vertically-integrated acceleration defect. To illustrate this in a different way, the vertical integral of the acceleration defect is clearly non-zero over the crest in potential flow, which is frictionless (see Figure 2.6). As a result, the shear stress is not directly related to the vertically integrated acceleration defect over orbital-scale ripples.

5.1.2 Lee vortex evolution and associated turbulence

The distribution of the flow at different phases of the forcing cycle revealed the evolution of the lee vortex. At maximum forcing, a small separation bubble was present downstream from the ripple crest which increased in size as the free-stream velocity slowed.

The method used to calculate the second moments of the turbulent velocity fluctuations has yielded promising results. From the velocity fluctuation estimates, the distribution of Reynolds stress, turbulent kinetic energy and turbulence production have been obtained over a ripple wavelength. A region of high stress and turbulent kinetic energy associated with the lee vortex has been observed. Furthermore, the evolution of turbulence production over a ripple wavelength showed that the bottom as well as the lee vortex were sources of turbulence. At the higher orbital excursion, a stronger flow field was measured and, as a result, a larger separation bubble was present. The Reynolds stress associated with the lee vortex was also found to be larger at the increased orbital excursion.

Reynolds stress, turbulent kinetic energy and turbulence production are all associated with the presence of the lee vortex in different ways. Reynolds stress is a measure of the stress applied on the mean flow by the turbulent fluctuations (*Kundu*, 1990), whereas turbulent kinetic energy is a measure of the energy embedded in the lee vortex. In contrast, turbulence production represents a rate rather than a state. Specifically, it is a measure of the rate of energy production given by the interaction of the Reynolds stress with the mean vertical shear (*Kundu*, 1990). To summarize, Reynolds stress and turbulent kinetic energy are embedded in the lee vortex, which is a source of turbulence.

5.1.3 Friction factors and hydraulic roughness

Shear stress estimates over equilibrium orbital-scale ripples were determined using different methods. It should be noted that form drag is not included in any of the stress estimates. Friction factors obtained from single profiles of stress via the law-of-the-wall are at least a factor 10 greater than the estimates obtained from the Reynolds stress calculations. The error bounds on the maximum Reynolds stress estimate were found to be reasonably tight using the bootstrap technique. In contrast, the shear stress estimates and derived quantities such as hydraulic roughness obtained using the log-law are physically unrealistic.

The vorticity method assumes that the horizontal length scales are greater than the vertical length scales, but provides bed shear stress estimates at all points along the ripple profile. The double-averaging approach produces vertical profiles of the spatially-averaged Reynolds stress and bedform-induced stress, thereby yielding the net shear stress over a full ripple wavelength. Even though several major assumptions were made, the vorticity method produced similar results to the double-averaging technique, indicating that this approach has potential for obtaining accurate stress results.

Friction factor estimates from the spatially-averaged methods were a factor 2 smaller than the friction factors obtained using the Reynolds stress measurements. In addition, friction factors as a function of phase were determined by double-averaging over a half-wavelength. These results were consistent with the friction factors obtained via the full-wavelength double-averaging approach. Furthermore, the double-averaging and the vorticity methods were found to yield very similar hydraulic roughness estimates to each other and to the r_h estimate obtained from the ripple geometry. For both methods, the hydraulic roughness to ripple height ratio lies between 1 and 3, values which are much more sensible than the values of 14 to 40 obtained via the law-of-the-wall. Overall, spatially-averaged approaches have proven to produce reliable shear stress estimates over rippled beds.

5.2 Conclusion

Very promising near-bed flow measurements have been obtained using the MFDop in an oscillating tray set-up. However, constraints of this kind of experimental set-up need to be considered. In order to get an instantaneous picture of the flow, multiple runs where the MFDop is located at different positions along the ripple profile must be executed. In order to improve tracking of the lee vortex, it would be desirable to make more MFDop measurements with less physical space between them. However, executing more RippleKart runs while increasing the excursion could be problematic since the ripples might evolve between runs to adjust to the new forcing conditions.

One of the goals of the present research was to explore the limits of MFDop performance in a laboratory setting as a precursor to making similar measurements in the field. This state-of-the-art instrument has been shown to provide high resolution flow measurements at turbulence-resolving scales over orbital-scale ripples. In addition, the near-bed distributions of Reynolds stress and turbulent kinetic energy that have been obtained are clearly associated with the presence of the lee vortex, which is very encouraging. It would be of great interest to compare these laboratory results with similar field measurements.

The present results are encouraging for related future work that could include investigating the effects of ripple shape and ripple steepness on the flow field. Similar to *Jonsson and Carlson* (1976), measurements could be made over different beds of artificial ripples. In addition, the effect of varying the grain size distribution on ripple morphology and suspended sediment concentrations could be studied. In fact, creating ripples using a wider grain size distribution would simulate certain natural conditions more closely. Furthermore, it would be of interest to explore in detail the result of increasing the orbital excursion, which would lead to making measurements over evolving ripples. These results would be of use to improve our understanding of the adjustment of rippled beds to varying hydrodynamic conditions.

APPENDIX A

EQUATIONS IN THE MOVING FRAME OF REFERENCE

We are interested in the equations governing the flow above an oscillating plate with no imposed flow in the moving frame of reference. Let ˆ denote variables in the frame of reference moving with the boundary. The horizontal spatial coordinate in the moving frame of reference $\hat{x}$ as a function of the horizontal spatial coordinate in the lab frame x is given by

$$\hat{x} = x - \int_0^t U(\xi) d\xi \tag{A.1}$$

where U is the flow in the interior. Let us assume that there is oscillatory flow in the interior, i.e. $U = U_0 \cos \omega t$. Integrating equation A.1,

$$x = \hat{x} + \frac{U_0}{\omega} \sin \omega t \tag{A.2}$$

Differentiating with respect to time,

$$\begin{aligned} u &= \hat{u} + U_0 \cos \omega t && \text{(A.3)} \\ \frac{\partial u}{\partial t} &= \frac{\partial \hat{u}}{\partial t} - U_0 \omega \sin \omega t && \text{(A.4)} \end{aligned}$$

In the lab frame of reference, the Navier-Stokes equations for uniform oscillatory flow within the bottom boundary layer are

$$\frac{\partial u}{\partial t} = \frac{1}{\rho}\left(-\frac{\partial p}{\partial x} + \frac{\partial \tau^x}{\partial z}\right) \tag{A.5}$$

$$\frac{\partial p}{\partial z} = 0 \tag{A.6}$$

where ρ is the fluid density, p is the pressure and τ^x is the shear stress in the x-direction. Using equation A.4 and A.5, the horizontal momentum equation in the moving frame of reference can be determined. Within the bottom boundary layer,

$$\frac{\partial \hat{u}}{\partial t} - U_0\omega \sin \omega t = \frac{1}{\rho}\left(-\frac{\partial p}{\partial x} + \frac{\partial \tau^x}{\partial z}\right) \tag{A.7}$$

and in the interior,

$$\frac{\partial \hat{u}_\infty}{\partial t} - U_0\omega \sin \omega t = -\frac{1}{\rho}\frac{\partial p}{\partial x} \tag{A.8}$$

where $\hat{u}_\infty$ is the velocity in the interior in the moving frame of reference. Using equations A.7 and A.8,

$$\frac{\partial}{\partial t}(\hat{u} - \hat{u}_\infty) = \frac{1}{\rho}\frac{\partial \tau^x}{\partial z} \tag{A.9}$$

where $\hat{u} - \hat{u}_\infty$ is the defect velocity. The standard boundary layer approximation, which assumes that the magnitude of the variations of the flow in the stream-wise direction is much smaller than the magnitude of the variations across the boundary, has been used to eliminate the pressure gradient term. The momentum equation for the velocity defect in the moving frame of reference (equation A.9) is equivalent to the momentum equation in the inertial frame of reference (equation 2.6).

APPENDIX B

MFDOP BEAM BISECTOR SEPARATION

As discussed in section 3.2, the separation between the MFDop beam bisectors increases with distance from the point where the beam axes intersect. A sketch of the MFDop beam bisectors is shown in Figure B.1. The distances d_{13} and d_{23} between the bisectors and the centre beam at a distance R from the centre transducer are given by:

$$d_{13} = (r_0 - R)\tan\theta_{13} \tag{B.1}$$

$$d_{23} = (r_0 - R)\tan\theta_{23} \tag{B.2}$$

where $r_0 = 40$ cm is the beam intersection. The bisector angles between transducers 1 and 3 and between transducers 2 and 3 are given by θ_{13} and θ_{23} respectively. From *Hay et al.* (2012a), these bisector angles are θ_{13} =7.25° and θ_{23} =7.10°. The beam bisector separation is thus given by the sum of d_{13} and d_{23}. A plot of the beam bisector separation as a function of the range used for the RippleKart experiments is given in Figure B.2. The beam bisector separation is zero at 40 cm from the centre transducer and increases as measurements are made further away from this point. This separation is of the order of a few centimetres.

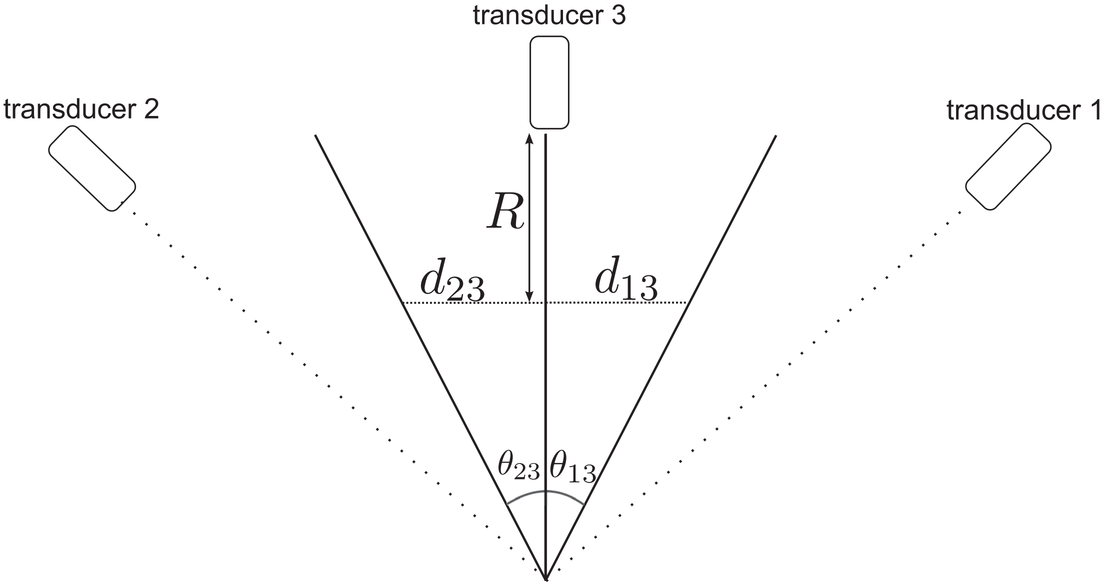

Figure B.1: Sketch of the MFDop beam bisectors between transducers 1 and 3 and transducers 2 and 3. The bisector angle θ between transducers at the beam axis intersection point is indicated. The distances d between the bisectors and the centre beam at a distance R from the centre transducer is also indicated.

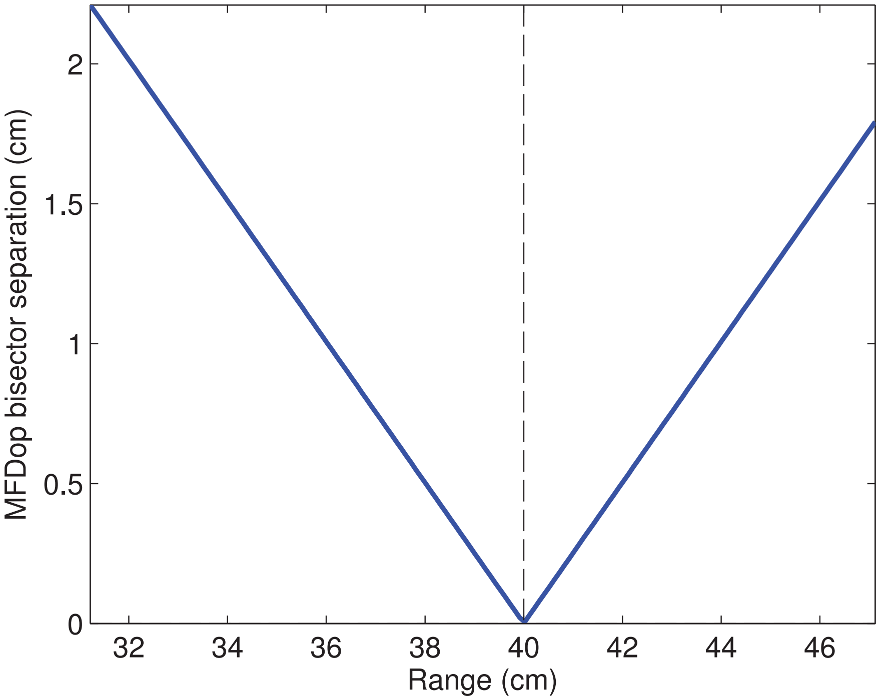

Figure B.2: MFDop beam bisector separation as a function of range from the centre transducer.

APPENDIX C

RANGE CORRECTION

Due to the MFDop's geometry, the vertical range from an outboard transducer to a target is shorter than the vertical range from the centre transducer to the same target. Therefore, the measurements registered by each transducer must be interpolated onto the centre transducer's vertical range.

A sketch of the relevant angles and distances between MFDop transducers 1 and 3 is given in Figure C.1. A pulse travelling from transducer 3 to 1 will travel a total distance of $2r$. Signals arriving at the centre transducer at the same time will also have travelled a distance $2r$. Thus, denoting the vertical distance corresponding to these simultaneous arrivals by D_{33} and D_{13} respectively, we have

$$D_{33} = r \tag{C.1}$$

$$D_{13} = r\cos\beta \tag{C.2}$$

where β is the angle between D_{13} and r. From Figure C.1,

$$\beta = \pi/2 - \gamma - \theta_0 \tag{C.3}$$

$$\gamma = \pi/2 - \theta \tag{C.4}$$

where θ_0 is the bisector angle between transducer 1 and 3 at the beam axis intersection point and θ is the bisector angle for a scatterer located along the bisector. As a result,

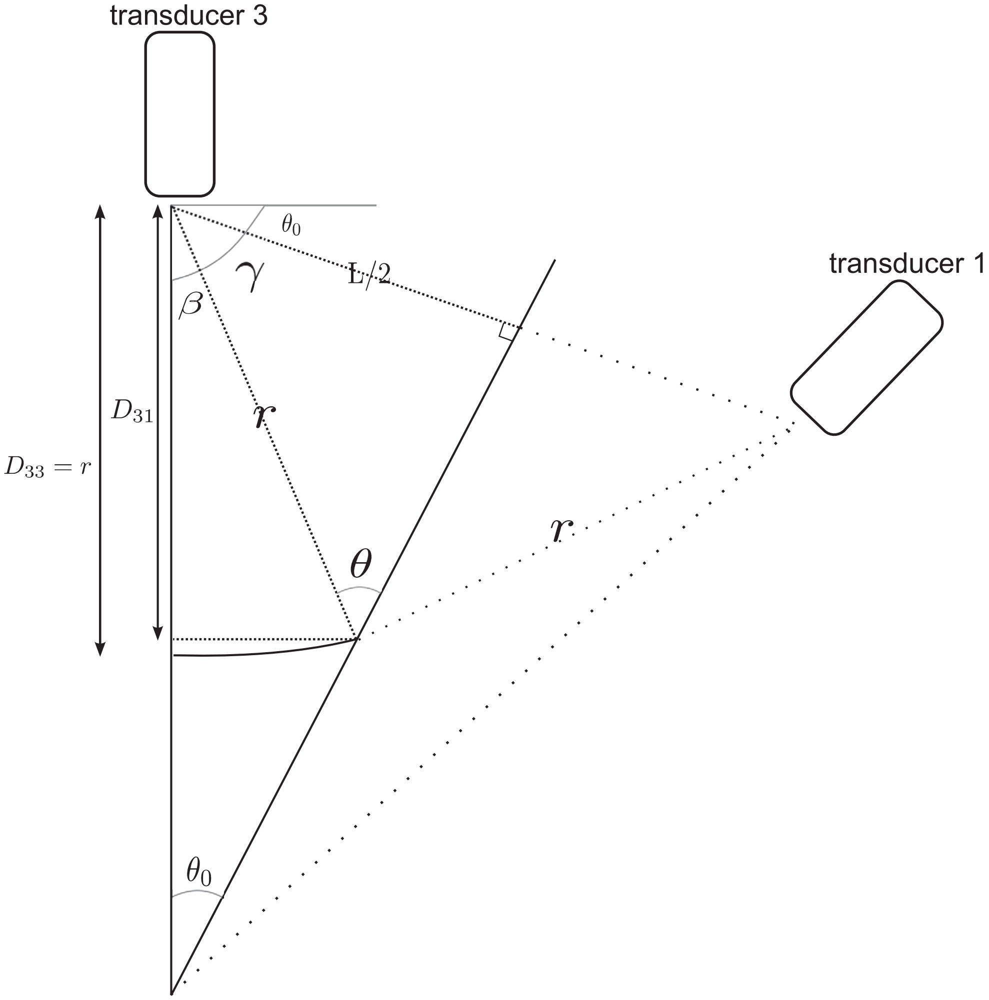

Figure C.1: MFDop sketch of angles and distances travelled by a pulse between transducers 1 and 3 showing θ_0, the bisector angle between transducer 1 and 3 at the beam axis intersection point, and θ, the bisector angle for a scatterer located along the same axis.

$\beta = \theta - \theta_0$ and using equation C.2,

$$D_{13} = r\cos(\theta - \theta_0) \tag{C.5}$$

Similarly, the distances between the other outboard transducers and centre transducer can also be calculated.

APPENDIX D

BOTTOM CONTAMINATION

We are interested in determining the minimum distance away from the bed that measurements can accurately be obtained without any contamination from the bed. A sketch of a pulse travelling between the centre transducer and an outboard transducer is presented in Figure D.1. The distance $R = R_1 + R_2$ that a pulse travels from transducer 1 to an outboard transducer is given by

$$R_1 = \sqrt{h_1^2 + x^2} \tag{D.1}$$

$$R_2 = \sqrt{h_2^2 + (d - x)^2} \tag{D.2}$$

where $d = L \cos \theta_0$ and $h_2 = h_1 - L \sin \theta_0$. The path of least time is also the minimum distance path R_{min}. The latter can be determined when the first derivative is equal to zero: $dR(x)/dx = 0$. Thus, we obtain

$$\frac{x}{\sqrt{h_1^2 + x^2}} - \frac{d - x}{\sqrt{h_2^2 + (d - x)^2}} = 0 \tag{D.3}$$

Using θ_0 =7°, $L =$ 9.6 cm and $h_1 =$ 40 cm, we can determine x. Both terms of equation D.3 are plotted as a function of x in Figure D.2. The intersection point is located at $x =$ 4.84 cm and, as a consequence, $R_{min} = R(x) =$ 79.4 cm. The distance that a pulse travels from the centre transducer and back is $2h_1 =$ 80 cm. As a result, the bottom return from an outboard transducer arrives earlier by 6 mm.

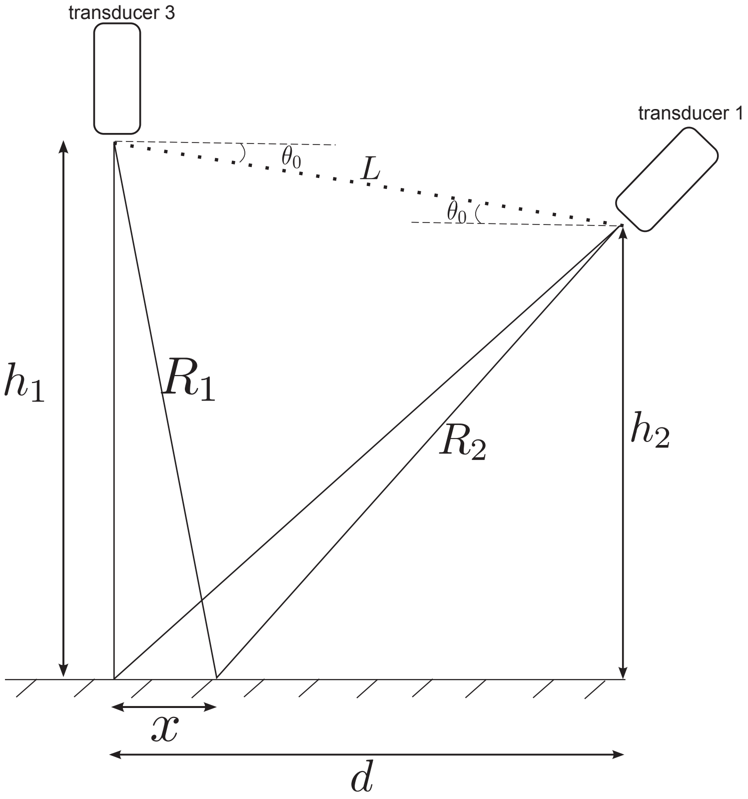

Figure D.1: MFDop sketch of a pulse travelling between the centre transducer and an outboard transducer over a flat bottom.

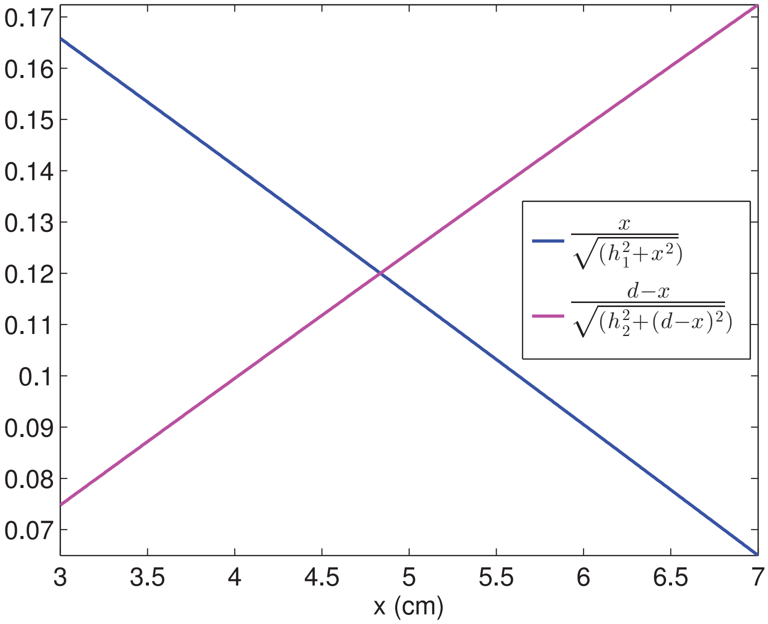

Figure D.2: MFDop bottom contamination: solving equation D.3

APPENDIX E

ACCELERATION FORCE

Nielsen (1992) and *Tunstall and Inman* (1975) have both mentioned a caveat concerning the oscillating tray set-up. The acceleration force acting upon a sand particle being accelerated in a stationary fluid is different from the force exerted on a stationary particle in an accelerating flow. From *Nielsen* (1992) and based upon Newton's second law of motion, the force exerted on a resting particle on a fixed bed in an accelerating fluid is given by

$$\rho(1 + C_M)V_p\frac{\partial u}{\partial t} \tag{E.1}$$

where V_p is the particle volume and C_M is the added mass coefficient. In contrast, the force exerted on a sand grain on a moving bed and, thus being accelerated in a stationary flow, is

$$\rho(s + C_M)V_p\frac{\partial u}{\partial t} \tag{E.2}$$

where s is the specific sediment density or the ratio between the sediment density and the fluid's density. For both cases, the $\rho C_M V_p$ term is the added hydrodynamic mass and corresponds to the volume of surrounding fluid that is being displaced by the particle (*Nielsen*, 1992). However, in the second case, the added hydrodynamic mass is added to the mass of the particle and thus the force has to also depend on the particle density, $\rho_s = s\rho$.

Similar to *Hay et al.* (2012c), the ratio between the force associated with shear stress

($\rho {u_*}_m^2 A_p$) and the acceleration force (equation E.2) is given by

$$\frac{{u_*}_m^2}{(s + C_M)\omega U_0} \frac{A_p}{V_p} \sim \frac{{u_*}_m^2}{(s + C_M)\omega U_0 D_{50}} \tag{E.3}$$

where A_p is the projected area of the particle. Using $s =$ 2.6 (sand), $C_M =$ 0.5 (value for a sphere (*Nielsen*, 1992)) and $U_0 =$ 0.2 m/s, the denominator of the right-hand-side of equation E.3 is 6×10^{-5} m^2/s^2, which is much smaller than the squared values of the observed maximum friction velocities (see Tables 4.3 and 4.4). As a result, the fluid pressure force acting on a particle resting on an accelerating bed used in these experiments is much smaller than the shear stress force. Nevertheless, the ripples created in the RippleKart could have been influenced by the forces due to the increased fluid pressure gradients present in an oscillating tray set-up. However, other factors could have had a more important influence such as end-effects due to the finite-length of the oscillating tray (*Hay et al.*, 2012c).

BIBLIOGRAPHY

Allen, J. R. L., A model for the interpretation of wave ripple-marks using their wavelength, textural composition, and shape, *J. Geol. Soc.*, *136*, 673–682, 1979.

Ardhuin, F., W. O'Reilly, T. Herbers, and P. F. Jessen, Swell transformation across the continental shelf. Part I: Attenuation and directional broadening, *J. Phys. Oceanogr.*, *33*, 1921–1939, 2003.

Bagnold, R. A., Motion of waves in shallow water. Interaction between waves and sand bottoms, *Proc. Roy. Soc.*, *Ser. A 187*, 1–15, 1946.

Barr, B. C., D. N. Slinn, T. Pierro, and K. B. Winters, Numerical simulation of turbulent, oscillatory flow over sand ripples, *J. Geophys. Res.*, *109*, doi:10.1029/2002JC001709, 2004.

Batchelor, G. K., *An Introduction to Fluid Dynamics*, Cambridge University Press, New York, 1967.

Blondeaux, P., and G. Vittori, Vorticity dynamics in an oscillatory flow over a rippled bed, *Journal of Fluid Mechanics*, *226*, 257–289, 1991.

Chou, Y.-J., and O. B. Fringer, A model for the simulation of coupled flow-bed form evolution in turbulent flows, *J. Geophys. Res.*, *115*, doi:10.1029/2010JC006103, 2010.

Christoffersen, J. B., and I. G. Jonsson, Bed friction and dissipation in a combined current and wave motion, *Ocean Engng*, *12*, 387–423, 1985.

Clifton, H. E., and J. R. Dingler, Wave–formed structures and paleoenvironmental reconstruction, *Mar. Geol.*, *60*, 165–198, 1984.

Coleman, S. E., V. I. Nikora, S. R. McLean, T. M. Clunie, T. Schlicke, and B. W. Melville, Equilibrium hydrodynamics concept for developing dunes, *Phys. Fluids*, *18*, 105104, 2006.

Davies, A. G., Wave intetactions with rippled sand beds, in *Physical Oceanography of Coastal and Shelf Seas*, edited by B. Johns, pp. 1–65, Elsevier, New York, 1983.

Du Toit, C. G., and J. F. A. Sleath, Velocity measurements close to rippled beds in oscillatory flow, *Journal of Fluid Mechanics*, *112*, 71–96, 1981.

Efron, B., and G. Gong, A leisurely look at the bootstrap, the jackknife, and cross-validation, *The American Statistician*, *37*, 36–48, 1983.

Fredsoe, J., and R. Deigaard, *Mechanics of Coastal Sediment Transport*, World Scientific, 1992, 369 pp.

Grant, W., and O. Madsen, The continental-shelf bottom boundary layer, *Ann. Rev. Fluid Mech.*, *18*, 265–305, 1986.

Hay, A. E., Sound scattering from a particle-laden turbulent jet, *J. Acoust. Soc. Am.*, *90*, 2055–2074, 1991.

Hay, A. E., L. Zedel, R. Craig, and W. Paul, Multi-frequency pulse-to-pulse coherent Doppler sonar profiler, in *Ninth Working Conference on Current Measurement Technology*, pp. 25–29, IEEE/OES/CMTC, 2008.

Hay, A. E., L. Zedel, R. Cheel, and J. Dillon, Observations of the vertical structure of turbulent oscillatory boundary layers above fixed roughness beds using a prototype wide-band coherent Doppler profiler: 1. The oscillatory component of the flow, *J. Geophys. Res.*, *117*, 2012a.

Hay, A. E., L. Zedel, R. Cheel, and J. Dillon, Observations of the vertical structure of turbulent oscillatory boundary layers above fixed roughness beds using a prototype wide-band coherent Doppler profiler: 2. Turbulence and stress, *J. Geophys. Res.*, *117*, 2012b.

Hay, A. E., L. Zedel, R. Cheel, and J. Dillon, On the vertical and temporal structure of flow and stress in the turbulent oscillatory boundary layer above evolving sand ripples: Observations using a prototype wide-band coherent Doppler profiler, *Cont. Shelf Res.*, *46*, 31–49, 2012c.

Hurther, D., and P. D. Thorne, Suspension and nearbed load sediment transport processes above a migrating sand rippled bed under shoaling waves, *J. Geophys. Res.*, *116*, doi:10.1029/2010JC006774, 2011.

Hurther, D., P. D. Thorne, M. B. U. Lemmin, and J.-M. Barnoud, A multi-frequency acoustic concentration and velocity profiler (ACVP) for boundary layer measurements of fine-scale flow and sediment transport processes, *Coast. Eng.*, *58*, 594–605, 2011.

Jensen, B., *Experimental Investigation of Turbulent Oscillatory Boundary Layers*, Institute of Hydrodynamics and Hydraulic Engineering, Technical University of Denmark, Lyngby, 1988.

Jensen, B., B. Sumer, and J. Fredsoe, Turbulent oscillatory boundary layers at high Reynolds numbers, *J. Fluid Mech.*, *206*, 265–297, 1989.

Jonsson, I., and N. Carlson, Experimental and theoretical investigations in an oscillatory turbulent boundary layer, *J. Hydraulic Res.*, *14*, 45–60, 1976.

Kamphuis, J. W., Determination of sand roughness for fixed beds, *J. Hydr. Res.*, *12*, 193–203, 1974.

Kundu, P. K., *Fluid Mechanics*, Academic Press, San Diego, 1990, 638 pp.

Lhermitte, R., and R. Serafin, Pulse-to-pulse coherent Doppler sonar processing techniques, *J. Atmos. Oceanic Tech.*, *1*, 293–308, 1984.

Longuet-Higgins, M. S., Oscillating flow over steep sand ripples, *Journal of Fluid Mechanics*, *107*, 1–35, 1981.

Marieu, V., P. Bonneton, D. L. Foster, and F. Ardhuin, Modeling of vortex ripple morphodynamics, *J. Geophys. Res.*, *113*, doi:10.1029/2007JC004659, 2008.

Mignot, E., E. Barthelemy, and D. Hurther, Double-averaging analysis and local flow characterization of near-bed turbulence in gravel-bed channel flows, *J. Fluid Mech.*, *618*, 279–303, 2009.

Monin, A. S., and A. M. Yaglom, *Statistical Fluid Mechanics: Mechanics of Turbulence*, vol. 1, MIT Press, Cambridge, MA, 1971, 769 pp.

Newgard, J. P., and A. E. Hay, Turbulence intensity in the wave boundary layer and bottom friction under (mainly) flat bed conditions, *J. Geophys. Res.*, *112*, 2007, C09024.

Nichols, C. S., and D. L. Foster, Full-scale observations of wave-induced vortex generation over a rippled bed, *J. Geophys. Res.*, *112*, 2007.

Nielsen, P., *Coastal Bottom Boundary Layers and Sediment Transport*, World Scientific, River Edge, New Jersey, 1992, 324 pp.

Nikora, V. I., I. McEwan, S. McLean, S. Coleman, D. Pokrajac, and R. Walters, Double-averaging concept for rough-bed open-channel and overland flows: Theoretical background, *J. Hydraul. Eng.*, *133*, 873–883, 2007a.

Nikora, V. I., S. McLean, S. Coleman, D. Pokrajac, I. McEwan, L. Campbell, J. Aberle, D. Clunie, and K. Koll, Double-averaging concept for rough-bed open-channel and overland flows: Applications, *J. Hydraul. Eng.*, *133*, 884–895, 2007b.

Raupach, M. R., Drag partition on rough surfaces, *Bndry-Layer Met.*, *60*, 375–395, 1992.

Riedel, H. P., J. W. Kamphuis, and A. Brebner, Measurement of bed shear stress under waves, in *Proc. of 13th Coastal Engineering Conference*, pp. 587–603, Vancouver, 1972.

Sleath, J., Turbulent oscillatory flow over rough beds, *J. Fluid Mech.*, *182*, 369–409, 1987.

Sleath, J. F. A., *Sea Bed Mechanics*, John Wiley, New York, 1984, 335 pp.

Smyth, C., and A. E. Hay, Wave friction factors in nearshore sands, *J. Phys. Oceanogr.*, *32*, 3490–3498, 2002.

Swart, D., Offshore sediment transport and equilibrium beach profiles, *Tech. Rep. 131*, Delft Hydraulics Lab., 1974.

Tunstall, E. B., and D. L. Inman, Vortex generation by oscillatory flow over rippled surfaces, *J. Geophys. Res.*, *80*, 3475–3484, 1975.

van der Werf, J. J., J. S. Doucette, T. O'Donoghue, and J. S. Ribberink, Detailed measurements of velocities and suspended sand concentrations over full-scale ripples in regular oscillatory flow, *J. Geophys. Res.*, *112*, 2007, doi:10.1029/2006JF000614.

Wiberg, P. L., and C. K. Harris, Ripple geometry in wave-dominated environments, *J. Geophys. Res.*, *99*, 775–789, 1994.

Zedel, L., and A. Hay, A coherent Doppler profiler for high resolution particle velocimetry in the ocean: laboratory measurements of turbulence and particle flux, *J. Atmos. and Ocean. Tech.*, *16(8)*, 1102–1117, 1999.

Zedel, L., and A. Hay, Resolving velocity ambiguity in multi-frequency, pulse-to-pulse coherent Doppler sonar, *IEEE J. Oceanic Eng.*, *35(4)*, 847–850, 2010.